International Journal of Heat and Mass Transfer 213 (2023) 124296

Contents lists available at ScienceDirect

International Journal of Heat and Mass Transfer

journal homepage: www.elsevier.com/locate/hmt

Parametric experimental trends, interfacial behavior, correlation assessment, and interfacial lift-off model predictions of critical heat flux for microgravity flow boiling with subcooled inlet conditions – Experiments onboard the International Space Station

Issam Mudawar[#,*], Steven J. Darges, V.S. Devahdhanush

Purdue University Boiling and Two-Phase Flow Laboratory (PU-BTPFL), School of Mechanical Engineering, Purdue University, 585 Purdue Mall, West Lafayette, IN 47907, United States

ARTICLE INFO

Article history:
Received 11 January 2023
Revised 7 April 2023
Accepted 9 May 2023
Available online 31 May 2023

Keywords:
Flow boiling
Microgravity
Critical heat flux
Subcooled inlet
Flow visualization
Interfacial lift-off model

ABSTRACT

This study examines the critical heat flux data obtained during the "Flow Boiling and Condensation Experiment (FBCE)" which was launched to the International Space Station (ISS) in August 2021. The overarching goals of FBCE are to obtain flow boiling and flow condensation data in high quality, long-duration microgravity, and investigate gravitational effects on two-phase flow physics. The first stage of FBCE completed features the Flow Boiling Module (FBM), which collected flow boiling heat transfer data and flow visualization images in a highly accurate and steady microgravity environment from February 2022 until July 2022. Flow boiling experiments were performed with subcooled inlet of n-Perfluorohexane in a rectangular channel of dimensions 114.6-mm heated length, 2.5-mm heated width, and 5.0-mm height with either one or two, opposite, heated walls. The long-duration microgravity database encompasses a broad range of operating conditions: mass velocity of 199 – 3200 kg/m^{2}s, inlet subcooling of 2.6 – 45.6°C, and inlet pressure of 124.8 – 176.7 kPa. Image sequences leading up to and at CHF are presented to both illustrate the physical mechanism triggering CHF and explain the experimental trends observed in microgravity. Experimental results show CHF is strongly dependent on mass velocity and higher degrees of inlet subcooling, but less dependent on inlet pressure in the tested ranges. Examination of the relationships and parametric trends between dimensionless groups governing CHF reinforces conventional trends and reveals, for subcooled CHF, a dependence of Boiling number at CHF on outlet thermodynamic equilibrium quality. Comparison of the new microgravity CHF data with Earth-gravity CHF data reveals, for single-sided heating, CHF in microgravity is degraded up to ~38% at low mass velocity, with diminishing differences as mass velocity is increased, and for double-sided heating, less significant differences in CHF between the two gravitational environments. Experimental data are compared to predictions of various flow boiling CHF correlations which previously demonstrated their merit, and the most suitable one for the entire database is recommended. Flow visualization reveals a wavy vapor layer with wetting fronts described in the *Interfacial Lift-off Model*, which is used to predict CHF values with good accuracy.

1. Introduction

1.1. Two-phase systems in future space missions

Thermal management is a crucial component in the design of any heat dissipating system. In certain high heat flux applications prevalent in the computing, medical, transportation, energy, aerospace, and defense industries, two-phase thermal management systems offer sufficient cooling where conventional single-phase systems are inadequate. This is owed to two-phase systems taking advantage of the fluids' latent heat, while single-phase systems solely rely on sensible heat. Two-phase systems are configured into numerous schemes, including capillary flows, evaporating falling films, pool boiling, channel flow boiling, jet impingement boiling, and spray cooling. Flexibility in design coupled with larger heat dissipation rates allows engineers to minimize the size and weight of thermal management systems, which is a premium in many applications. Specifically, two-phase thermal management systems have been tapped to play a crucial role in future space missions. A recent NASA technical report [1] cites boiling systems

* Corresponding author.
E-mail address: mudawar@ecn.purdue.edu (I. Mudawar).
website: https://engineering.purdue.edu/BTPFL

https://doi.org/10.1016/j.ijheatmasstransfer.2023.124296
0017-9310/

Nomenclature

A_c	channel cross-sectional area, [m^2]
b	ratio of wetting front length to wavelength
Bd_θ	orientation-specific Bond number, $g\cos\theta(\rho_f-\rho_g)D^2/\sigma$
Bo	Boiling number at CHF, $q''_{CHF}/(Gh_{fg})$
C	constant
c	wave speed, [m/s]
D	diameter, [m]
D_e	equivalent heated diameter, $4A_c/P_h$ [m]
D_h	hydraulic diameter, [m]
f	friction factor
Fr_θ	orientation-specific Froude number, $G^2/(\rho_f^2 g\sin\theta D)$
G	mass velocity, [kg/m^{2}s]
g	gravitational acceleration, [m/s^2]
g_e	gravitational acceleration on Earth, [m/s^2]
μg_e	microgravity, [m/s^2]
H	height of channel, [m]
h	enthalpy, [J/kg]
h_{fg}	latent heat of vaporization, [J/kg]
Δh_{sub}	h_f - h_b, [J/kg]
k	wave number, [1/m]; thermal conductivity, [W/m-K]
L	length, [m]
$\dot{m}$	mass flow rate [kg/s]
N	number of data points
P	perimeter, [m]
p	pressure, [Pa]
p_r	reduced pressure
q''	heat flux, [W/cm^2]
q''_{CHF}	critical heat flux, [W/cm^2]
Re_{fo}	Reynolds number, GD/μ_f
Re_k	Phase Reynolds number
T	temperature, [°C]
ΔT_{sub}	fluid subcooling, T_{sat} – T_f, [°C]
t	time, [s]
u	mean phase velocity, [m/s]; velocity, [m/s]
W	width of channel, [m]
We_D	Weber number based on channel diameter, $G^2D/(\rho_f\sigma)$
We_L	Weber number based on channel heated length, $G^2L_h/(\rho_f\sigma)$
x	flow quality
x_e	thermodynamic equilibrium quality
y	coordinate normal to interface, [m]
z	streamwise coordinate, [m]
z_o	streamwise location where vapor velocity just exceeds liquid velocity, [m]
z^*	streamwise location for determining vapor layer thickness and critical wavelength, [m]

Greek symbols

α	void fraction
δ	mean vapor layer thickness, [m]
ε	heat utility ratio
η	interfacial perturbation
θ	orientation angle of channel [°]
λ	wavelength, [m]
μ	dynamic viscosity, [kg/m-s]
ξ_{30}	percentage of datapoints predicted within ±30%
ξ_{50}	percentage of datapoints predicted within ±50%
ρ	density, [kg/m^3]
ρ''	modified density, [kg/m^3]
σ	surface tension, [N/m]
τ	shear stress, [Pa]

Subscripts

a	corresponding to heated wall 1 or 2 (= 1 or 2)
b	local bulk liquid
c	critical
d	development
D_e	calculated $D = D_e$
e	exit
exp	experimental
f	saturated liquid; bulk fluid
g	saturated vapor
h	heated
i	interfacial
in	inlet
k	either liquid (f) or vapor (g)
out	outlet
$pred$	predicted
s	solid
sat	saturation
sub	subcooling
tc	substrate thermocouple
w	wall
wa	heated wall (= $w1$ or $w2$)
z	local

Acronyms

BHM	Bulk Heater Module
CHF	Critical Heat Flux
CHF–	Prior to CHF
CHF+	After CHF
FBCE	Flow Boiling and Condensation Experiment
DC	Direct Current
FBM	Flow Boiling Module
FIR	Fluid Integrated Rack
FSML	Fluids System Module – Lower
FSMU	Fluids System Module – Upper
ISS	International Space Station
ITCS	ISS Thermal Control System
MAE	Mean Absolute Error (%)
MST	Mission Sequence Testing
nPFH	n-Perfluorohexane
ONB	Onset of Nucleate Boiling
RDAQM1	Remote Data Acquisition Module 1
RDAQM2	Remote Data Acquisition Module 2
RMSE	Root Mean Square Error (%)
RTD	Resistance Temperature Detector
TMA	Test Module Assembly
VES	Vacuum Exhaust System

to be vital in the safe operation of onboard life support systems, avionics, Rankine power systems, and high-power-density energy conversion equipment. Eventually, these augmentations will aid in the commercialization of the Earth and Moon space domain, transportation of humans to Mars, and development of human habitats on the Moon and Mars. Complementary to boiling, condensation is equally poised to support future space missions, with any closed loop thermal management, vapor compression, or Rankine power cycle requiring condensation to return the working fluid back to single-phase liquid.

A daunting task in implementing two-phase systems for space missions is confidently predicting their performance to ensure safe and successful operation. As shown in Fig. 1, a wide range of g is experienced in aerospace applications, where deviations from Earth gravity ($1g_e$) render two-phase-system design tools based

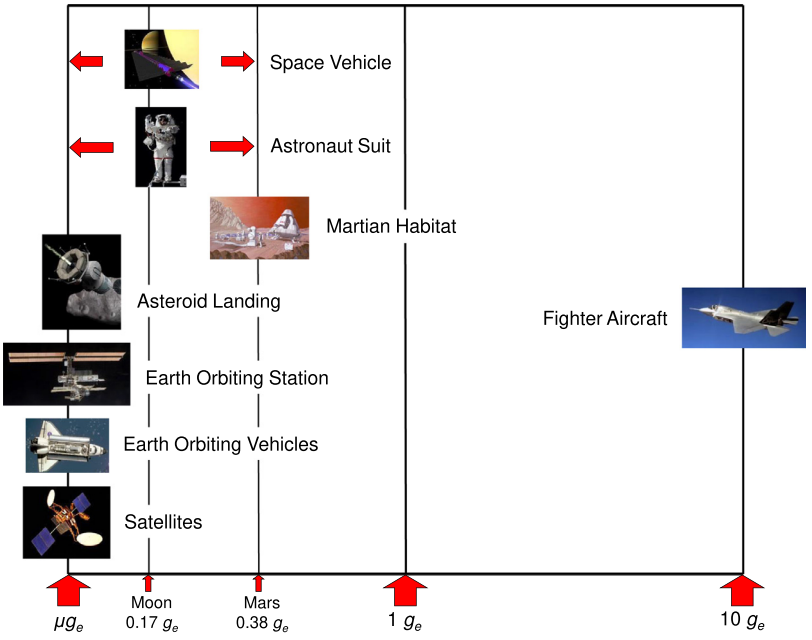

Fig. 1. Range of gravities important to study of two-phase flow and heat transfer in space and aircraft applications.

on terrestrial experiments and databases unreliable. The magnitude of body force has a strong influence on flow regime, pressure drop, and heat transfer performance. Hence, it is imperative for researchers to develop databases, correlations, theoretical models, and computational tools based on reliable reduced gravity experiments [2]. Alternatively, operation in a gravity independent regime can be achieved for both flow boiling and flow condensation (for example, criteria for gravity-independent operation of flow boiling is proposed in [3] and flow condensation in [4]), in which conventional methods would be sufficient in predicting system performance, but may not be achievable for every application.

1.2. Review of boiling experiments in microgravity

1.2.1. Boiling experiments in short durations of microgravity – prior to year 2000

Investigating the heat transfer performance and interfacial behavior of boiling in microgravity (μg_e) has become a top priority for many researchers. In most studies, short duration μg_e data for either pool or flow boiling is obtained via drop towers, sounding rockets, or parabolic flights.

Oka *et al.* [5] investigated pool boiling of n-pentane onboard a parabolic flight. They observed four separate regimes in μg_e, compared to only three in terrestrial gravity. The first regime in both environments was a single-phase regime with no bubbles followed by an isolated bubble regime. In μg_e, bubbles remained attached to the heated surface as opposed to rapid bubble departure observed in $1g_e$. The next regime featured prominent bubble coalescence and growth. This occurred at the heated wall in μg_e, causing bubbles to expand into the subcooled liquid where interfacial condensation occurred. In $1g_e$, rapid departure of bubbles from neighboring nucleation sites led to coalescence away from the heated wall. A fourth regime was observed unique to μg_e, featuring vapor slugs covering the heated surface. At high heat fluxes, inertia-induced bubble departure occurred as bubbles rapidly coalesced. Overall, the differences in bubble behavior led to moderate heat transfer coefficients in μg_e compared to terrestrial experiments.

Onboard a parabolic flight, Saito et al. [6] examined flow boiling of water over a horizontal heated rod in a square channel. Compared to ground data, bubble detachment was significantly less in μg_e, which resulted in vapor surrounding the rod downstream. Differences were more pronounced at low flow rates and high heat fluxes. However, they found significant differences in flow regimes between μg_e and $1g_e$ produced only minor differences in heat transfer coefficient.

Ohta [7] considered both flow boiling of R-113 through a glass tube coated with a thin gold film, and pool boiling of water and ethanol over a transparent sapphire glass plate during parabolic flights. During their flow boiling experiment, heat transfer of nucleate boiling in low-quality bubbly flow is consistent between $1g_e$ and μg_e at all mass velocities. Larger bubble diameters in μg_e led to a lower-quality transition to annular flow. For moderate-quality annular flows, nucleate boiling is suppressed, and heat transfer is deteriorated in μg_e. However, at sufficiently high heat fluxes, nucleate boiling was observed in the liquid film, eliminating discrepancies due to gravity. High quality annular flows, even at low heat fluxes, were less influenced by gravity as shear forces became dominant. Critical heat flux (CHF) experienced as dryout at high qualities was found to be similar in μg_e and $1g_e$. In pool boiling, a large, coalesced bubble was observed above the heated wall with a liquid layer buffer between it and the heated surface. They noted the dominant mechanism of heat transfer to be evaporation of a liquid layer that remained below bubbles within the buffer layer. Local heat transfer coefficients could be greater or lesser than those in $1g_e$ depending on whether dryout patches form in the liquid layer or not, but averaged heat transfer coefficients were found to be insensitive to gravity. The observed detachment of bubbles from the heated wall was attributed to a relatively weak level of μg_e on the order of $g_e \times 10^{-2}$. Similarly, in their μg_e pool boiling experiments of ethanol over a transparent sapphire glass plate onboard a sounding rocket, Ohta *et al.* [8] observed conflicting trends of heat transfer coefficient, depending on vapor accumulation at the heated surface. Steady-state nucleate boiling was established only for low heat flux and high subcooling, while other conditions produced large amounts of vapor and resulted in CHF.

1.2.2. Boiling experiments in short durations of microgravity – between years 2000 and 2018

Ma and Chung [9] achieved μg_e via drop tower and studied flow boiling of FC-72 over a platinum wire. CHF was reported to be sig-

nificantly lower in μg_e than $1g_e$ at low flow rates. However, with sufficiently high flow rates, forced convection mitigated the influence of gravity. Similar trends were visually observed, and bubble behavior drastically differed between μg_e than $1g_e$ at low flow rates. As surface temperatures increased, bubbles coalesced along the wire in μg_e, while rapidly detaching in $1g_e$.

Zhang *et al.* [10] performed flow boiling experiments in a rectangular channel with FC-72 during parabolic flights. They investigated the formation and behavior of vapor in the channel leading up to CHF. Near CHF, a wavy vapor layer developed and slid along the wall, with little to no bubble detachment occurring. The authors noted that increasing either subcooling or flow rate decreased the thickness of the vapor layer. At low flow rates, q''_{CHF} in μg_e was significantly lower than horizontal flow in $1g_e$, where bubble detachment is abundant. At high flow rates, flow patterns in μg_e aligned with those in ground experiments, resulting in similar q''_{CHF}. This was elaborated in a two-part study by Konishi *et al.* [11,12], who used a rectangular channel with two opposite heated walls to perform flow boiling experiments with FC-72 during a parabolic flight. They also observed the formation of a wavy vapor layer along their heated walls, except at the combination of the lowest heat flux and flow rate, which produced bubbly flow. Upon entering the μg_e period of the parabola, heat transfer performance was degraded. The mean thickness of the vapor layer increased with increasing heat flux but decreased with increasing flow rate. Approaching CHF, the vapor layers from opposite walls grew large enough to merge in the downstream part of the channel, but independent wavy vapor layers remained on each wall upstream.

Xue et al. [13] studied pool boiling of FC-72 on a 1-cm^2 silicon chip during a drop tower experiment. Experiments were initialized by achieving steady-state boiling in $1g_e$ where rapid bubble departure was observed. Upon entering μg_e, departure frequency decreased, and bubbles grew larger before detaching. At low heat fluxes, the surface temperatures remained nearly constant and heat transfer performance was not impacted by transitioning to low gravity. They hypothesized that the temperature gradient along the bubble interface invokes a thermocapillary flow that promotes liquid replenishment at the heated wall and allows for steady-state nucleate boiling. Increasing the heat flux resulted in the formation of a larger bubble whose boundary layer promoted the growth and coalescence of smaller bubbles. As bubbles slid along the wall and coalesced, the generated momentum caused the large bubbles to detach from the heated surface. Bubble coalescence resulted in a large bubble covering most of the surface, resulting in degraded heat transfer performance and CHF in μg_e. Wang *et al.* [14] later performed similar experiments utilizing a 2-cm^2 silicon chip to investigate the impact of heater size. They observed similarity in trends between the two heaters in different gravities and heat transfer performance in the nucleate boiling regime to deteriorate with increasing heater size in both $1g_e$ and μg_e. However, at high heat fluxes, different bubble behavior and heat transfer mechanisms were observed for the two chips after entering μg_e. A hemispherical bubble was present over the 1-cm^2 chip, while an oblate vapor blanket formed on the 2-cm^2 chip. This behavior validated their speculation that boiling was dominated by surface tension and buoyancy. Surface-tension-dominated boiling can also be considered heater-size dependent and is typically present for small heaters or low gravity conditions, whereas buoyancy-dominated boiling is independent of heater size and is exhibited by large heaters or high gravity conditions [15]. This resulted in q''_{CHF} being ~20% higher for the larger heater.

Brutin et al. [16] focused on gravity's effects on void fraction, frictional pressure drop, and heat transfer during their parabolic flight experiments of flow boiling of HFE-7100 in a vertical Inconel mini-channel. Bubbles were found to grow quicker and larger in μg_e than hypergravity. They inferred bubble growth rate to be inversely related to bubble rise velocity in the channel. During vertical upflow, hypergravity resulted in faster-rising slower-growing bubbles compared to in μg_e. Larger bubbles in μg_e resulted in thinner liquid films near the wall and smaller effective liquid cross sections, which respectively yielded more efficient heat transfer and lower frictional pressure drops.

Onboard a suborbital rocket, Souza et al. [17] examined pool boiling of n-pentane on a downward-facing copper disk. They performed $1g_e$ and μg_e experiments with and without heater confinement. The effects of confinement were tested by creating a 0.3-mm narrow gap between the downward-facing heated surface and the opposite adiabatic wall. For the unconfined case, heat transfer coefficient was higher in μg_e than $1g_e$. Due to their heater orientation, the buoyancy forces present in $1g_e$ prevented bubble detachment resulting in relatively low heat transfer coefficients compared to μg_e. To the contrary, heat transfer was degraded in μg_e for the confined case, where cooling was inhibited by the confinement of the relatively large bubble size forming dry patches on the heated surface.

Narcy *et al.* [18] performed flow boiling experiments of HFE-7000 in a sapphire tube during parabolic flights. In subcooled flow boiling, bubbles grew larger and detached less frequently in μg_e, resulting in lower heat transfer coefficient. However, at higher flow rates, differences between $1g_e$ and μg_e lessened. As quality increased, flow transitioned to slug and eventually annular, however the transitions occurred at lower qualities in μg_e than $1g_e$. During annular flow, thinner liquid films were observed in μg_e. Despite this, heat transfer coefficients were found to be similar in $1g_e$ and μg_e, owing to the dominance of shear forces.

1.2.3. Boiling experiments in short durations of microgravity – year 2018 and later

Zhang *et al.* [19] studied flow boiling of FC-72 with a constant inlet velocity of $u_{in} = 0.5$ m/s and heat fluxes of 7.2, 11.5, 13.3, 18.2, and 21.3 W/cm^2 during free fall in a drop tower. After entering μg_e, heat transfer was slightly enhanced for heat fluxes of 13.3 W/cm^2 and lower, with increased bubble growth and coalescence. At a higher heat flux of 18.2 W/cm^2, increased bubble production and coalescence in μg_e resulted in large patches of vapor downstream on the heated wall. However, wall temperatures only slightly increased as liquid inertia advected the vapor patches out of the channel. At the highest heat flux of 21.3 W/cm^2, steady-state boiling was established in $1g_e$, but wall temperatures quickly escalated, and a vapor layer covered the entire wall in μg_e, indicating CHF occurred.

Pool boiling of HFE-7500 and water was studied in μg_e via a drop tower by Yang et al. [20]. While both fluids experienced greater coalescence in μg_e, different mechanisms were observed. For HFE-7500, which has a smaller contact angle than water, bubbles were observed to migrate along the heater and absorb smaller bubbles. This resulted in relatively quick vapor growth. Water, on the other hand, produced large, stationary bubbles which remained at their nucleation sites. A single large bubble was observed at the center of the heater as bubbles merged.

Lebon *et al.* [21] studied flow boiling of HFE-7000 in both vertical upflow and downflow on a parabolic flight. Data was collected throughout the entire parabola and at different orientations to capture gravitational accelerations ranging from $-1.8g_e$ to $1.8g_e$, allowing the authors to analyze the effects of gravity on flow boiling. Noticeable features in μg_e included decreased slip velocity, less frequent bubble detachment, and less turbulent mixing. These coupled effects resulted in a reduction in bubbly-flow heat transfer compared to other gravities. One exception was when nucleate boiling occurred in μg_e and single-phase flow was present at other gravity levels. This was attributed to the rapid growth of the thermal boundary layer in μg_e and resulted in superior heat transfer.

Similarly, Iceri et al. [22] examined vertical upflow boiling of FC-72 during a parabolic flight and compared their results from different phases of the parabolas. In general, they found bubbles in μg_e to be fewer, larger, and more circular compared to vertical upflow in $1g_e$ and hypergravity. They attributed this to the dominance of surface tension particularly at low flow rates. In the annular flow regime, μg_e featured the thickest liquid film and lowest heat transfer coefficients. In $1g_e$ and hypergravity, convective effects were enhanced by buoyancy increasing the drift velocity.

Liu et al. [23] compared the CHF of FC-72 flow boiling in a rectangular channel during a drop tower experiment to ground data at different orientations. They found CHF in μg_e to be consistently between CHF with the channel oriented at 135° and 315° in $1g_e$ and proposed these values be used as bounds when predicting μg_e CHF.

1.2.4. Advantages and limitations of different microgravity experimental methods

The aforementioned experiments employed standard, cost-effective techniques to produce short duration periods of μg_e during which valuable data shedding light on the physics of μg_e boiling are obtained. However, each method is accompanied with unique issues. Drop tower experiments provide a high quality of μg_e but may struggle to reach steady state due to their relatively short duration of μg_e [24]. Sounding rockets and parabolic flight data are prone to small oscillations in the observed level of gravity known as g-jitter, degrading the quality of μg_e [25]. In some cases, g-jitter may artificially enhance heat transfer in μg_e by causing continuous deformation of bubble shape provoking flow around the bubble [26]. Ideally, long-duration μg_e experiments with stable values of low gravity performed in space will be used to verify data collected and corresponding predictive tools developed during short duration experiments. In the past, some researchers relied on either space shuttles or recoverable satellites to collect long-duration μg_e boiling data. Additionally, the International Space Station (ISS) has been identified as a prime venue to collect high quality μg_e data [27]. However, large financial costs, long-term time commitments, and limited resources, such as power and physical space, onboard spacecrafts act as barriers to performing such experiments, resulting in relatively few opportunities.

1.2.5. Boiling experiments in long durations of high-quality microgravity

Lee et al. [28] studied pool boiling of R-113 for different combinations of heat flux and subcooling on a NASA space shuttle. Steady nucleate boiling was achieved, and heat transfer enhanced by the following process: vapor bubbles attached to the heater grow via evaporation and coalescence provoking motion of other nearby bubbles; bubble motion causes a single, relatively large bubble to lift-off the wall and hover above the surface; this bubble acts a vapor reservoir and continues to absorb other ejected bubbles; after vapor is absorbed into the reservoir, surface rewetting occurs, and new bubbles are formed. However, CHF occurred at significantly lower heat fluxes than in $1g_e$.

Onboard a Chinese recoverable satellite, Zhao et al. [29] tested pool boiling of R-113 on a thin platinum wire. In their experiments, they found the superheat required for the onset of nucleate boiling (ONB) has a weak dependence on gravity. After ONB, a large amount of vapor was quickly generated. Eventually a large bubble formed and occupied a significant portion of the wire, deteriorating heat transfer in μg_e. Bubble coalescence induced oscillations of other nearby bubbles, which in turn provoked bubble detachment. In the discrete bubbly regime, behavior could be demarcated by 3 critical-bubble-diameter values: many small bubbles with diameters less than 0.3 mm would form and depart from the wire; bubbles that were able to exceed this diameter would grow to a size between 3.5 and 6.6 mm; these bubbles were observed to oscillate along the wire and eventually coalesce; once a bubble that exceeds 8.4 mm is formed, it also departs from the wire. In terrestrial experiments, only the tiny bubbles were observed as buoyancy causes them to depart before they can grow larger. On another satellite, Zhao et al. [30] observed pool boiling of FC-72 on a flat plate during quasi-steady heating in which the voltage of the heater increased exponentially with time. They developed boiling curves for different subcoolings and pressures in μg_e and found CHF to be inferior compared to that in $1g_e$. In general, both heat transfer coefficient and CHF increased with subcooling and pressure, agreeing with the trends seen in terrestrial experiments. At high subcooling, a relatively small bubble with a smooth interface occupies a large fraction of but not the entire heater. This results in a special region in which nucleate boiling and dryout coexist, subduing an abrupt transition to film boiling. The size of the coalesced bubble increased with decreasing subcooling due to diminished condensation effects. Heat transfer will continue to increase and surface temperatures slowly rise until CHF is reached and vapor occupies the entire heater.

Raj et al. [26] performed over 200 pool boiling experiments of n-Perfluorohexane (nPFH), onboard the ISS as part of the Microheater Array Boiling Experiment (MABE) and investigated the effects of gravity, heater size, superheat, subcooling, and pressure in μg_e. ONB occurred at lower superheats resulting in larger heat fluxes at these superheats compared to $1g_e$. Overall, increasing subcooling and pressure resulted in enhanced heat transfer, with greater sensitivity than in $1g_e$. This was the result of bubbles growing to sizes that cover the entire heater preventing further nucleation. They found trends with respect to heater size to match those in $1g_e$. Generally, surface-tension-dominated boiling exists in μg_e and is dependent on the heater size.

Pool boiling of nPFH onboard the ISS was performed during the Nucleate Pool Boiling eXperiment (NPBX) [31] and consisted of two types of tests. One, focusing on the dynamics of a single or few bubbles and the other, integral tests examining parametric trends of the boiling curve. They observed, unlike in terrestrial gravity, bubbles remained on the heated surface and moved laterally, merged, and formed a large bubble at the center of the heater. Other smaller bubbles moved radially inward towards the central bubble, generating motion of smaller bubbles and liquid. At high superheats, this large bubble existed on or just above the heated surface and acted as a vapor sink, absorbing smaller bubbles. However, the established steady nucleate boiling in μg_e, as well as CHF, was found to be significantly lower than in $1g_e$.

Researchers in conjunction with the Japanese Aerospace Exploration Agency (JAXA), have outlined flow boiling experiments with nPFH through copper and heated glass tubes onboard the ISS [32]. These test sections coupled with an adiabatic transparent section downstream allow for the acquisition of heat transfer and CHF data with simultaneous observation of interfacial behaviors. Later papers have detailed heat loss analysis being performed to accurately determined inlet conditions for both single-phase [33] and two-phase inlet [34].

1.3. Critical heat flux for flow boiling

CHF is the transition point from the nucleate boiling to film boiling regime. In the nucleate boiling regime, the primary mechanism of heat transfer is bubble nucleation at the heated wall, featuring relatively low and uniform wall temperatures while vast quantities of heat are removed from the surface. On the other hand, the film boiling regime consists of a vapor layer between the heated surface and bulk liquid, shifting the heat transfer mechanism from nucleate boiling at the wall to evaporation at the liquid-vapor interface. The presence of vapor, which possesses

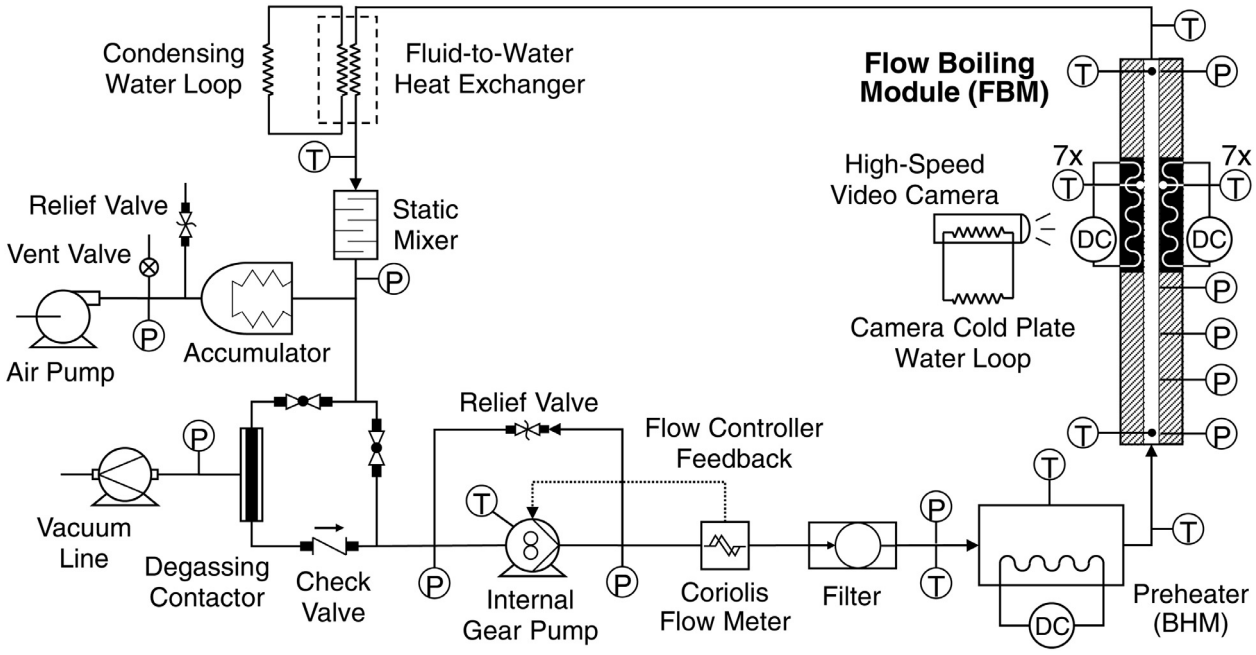

Fig. 2. Schematic diagram of two-phase flow loop used for flow boiling experiments.

significantly lower thermal conductivity than liquid, adjacent to the heated wall requires substantially higher wall temperatures to meet heat dissipation requirements than in the nucleate boiling regime. The abrupt shift from nucleate boiling to film boiling causes a simultaneous degradation in heat transfer coefficient and a sharp escalation in wall temperatures. This potentially becomes catastrophic if wall temperatures exceed safety limits resulting in overheating, burnout, or system failure. Hence, CHF is treated as arguably the most crucial parameter for any heat-flux-controlled thermal management system.

The prediction of CHF is handled through two primary avenues. First is the use of correlations consisting of empirical constants that aid in limiting the error with regards to the respective databases used for their development. Such correlations are typically simple and provide quick results but are designed for use with specific fluids, operating conditions, and flow geometries. Extrapolating correlations to unverified operating conditions could yield unreliable results. Some researchers have pursued the development of generalized or universal correlations [35,36] which are developed from sizeable consolidated databases and have shown the versatility to tackle a vast range of operating conditions. However robust these correlations may be, limitations in recommended operating conditions exist which render them unreliable or unusable in certain situations.

Alternatively, meticulous observations of CHF have led to the development of analytical models which are based on the physical mechanism occurring at CHF and require few empirical constants to obtain closure. One of the earliest-developed models is the *Boundary Layer Separation Model* by Kutateladze and Leont'ev [37]. They hypothesized production of vapor at the heated wall was similar to gas injection into a liquid boundary layer. As the velocity of gas increases to a critical value, the velocity gradient approaches zero, causing the boundary layer to separate from the wall. They also hypothesized vapor production can reach a rate that prevents liquid from contacting the heated wall, resulting in CHF. The *Bubble Crowding Model* was proposed by Weisman and Pei [38] for high-velocity flows in tubes. Their model assumes CHF occurs when a bubble layer adjacent to the heated wall reaches a critical volume fraction. At this point, a cluster of ellipsoidal bubbles limits turbulent fluctuations of liquid in the subcooled core from accessing the wall. Lee and Mudawar [39] developed the *Sublayer Dryout Model* for vertical subcooled flow boiling at high pressures and high mass velocities. Their model is based on observations of a vapor blanket that develops and traps a thin liquid layer against the heated wall as a result of Helmholtz instability at the interface. They define CHF as the heat flux that evaporates the liquid sublayer and prevents replenishment from the subcooled bulk liquid.

1.4. Objectives of present study

The Flow Boiling and Condensation Experiment (FBCE), a collaborative endeavor between the Purdue University Boiling and Two-Phase Flow Laboratory (PU-BTPFL) and the NASA Glenn Research Center, was initiated in 2011 with an ultimate goal of being installed onboard the ISS and collecting long-term microgravity data. This study features results from the first stage of FBCE utilizing the Flow Boiling Module (FBM), which was launched to the ISS in August 2021 and collected data from February 2022 to July 2022. A unique feature of FBM is its ability to simultaneously provide high-quality temperature measurements and invaluable flow visualization. The heat transfer results and interfacial flow physics for subcooled inlet to the FBM onboard the ISS have already been reported and discussed in detail in [40,41].

This study is focused on the CHF datapoints and the associated high-speed images obtained during long-duration microgravity experiments. Experimental trends of CHF in microgravity are analyzed in conjunction with flow visualization to explain the parametric trends with respect to mass velocity, inlet subcooling, inlet pressure, and heating configuration. Parametric trends of dimensionless groups related to the CHF mechanism are examined. The new ISS μg_e CHF data is compared to previously acquired CHF data for the vertical upflow orientation in $1g_e$. A brief correlation assessment is conducted with CHF correlations which have previously shown merit in predicting q''_{CHF} in μg_e for similar operating conditions. Finally, observations from flow visualization justify use of the *Interfacial Lift-off Model*, which has proven itself capable of predicting q''_{CHF} for a variety of operating conditions in different gravitational environments.

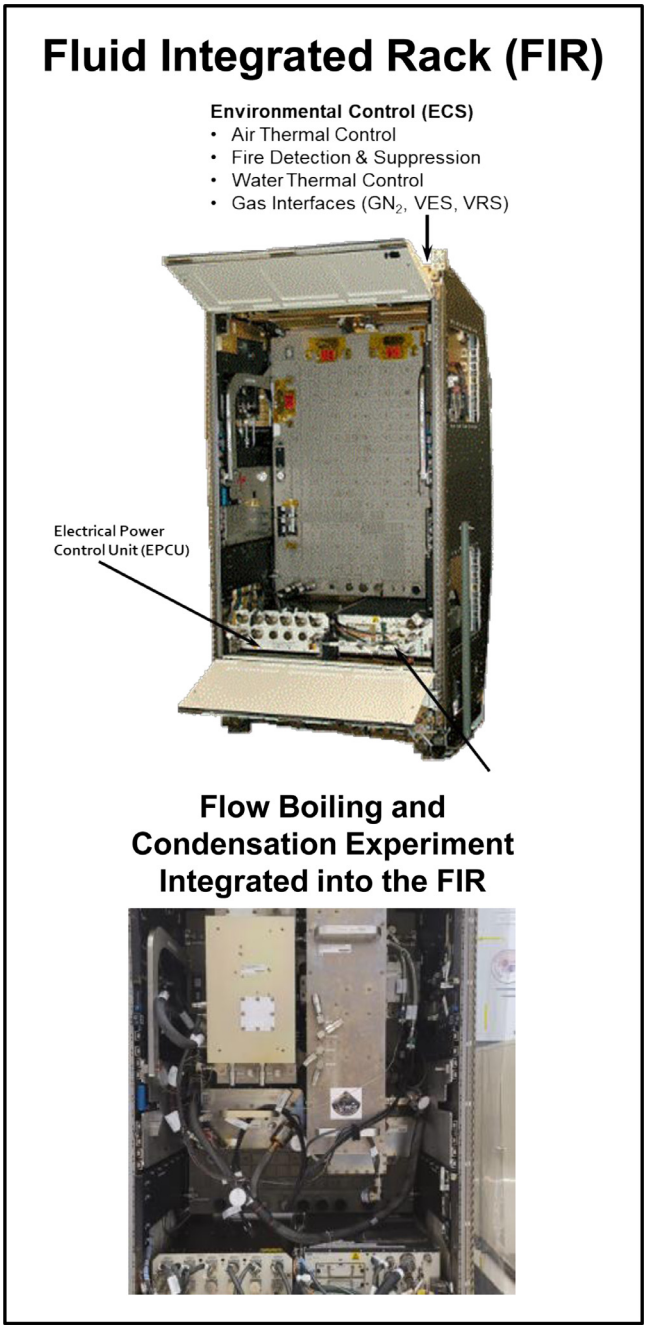

Fig. 3. Fluid Integrated Rack (FIR) and integration of FBCE into it.

2. Experimental methods

Key aspects of the experimental methods employed during data collection onboard the ISS are highlighted in this section. For comprehensive details regarding the flow loop, test module construction, instrumentation, measurement uncertainties, operating procedure, and data reduction, the reader is referred to [40].

2.1. Two-Phase flow loop and fbce rig

Fig. 2 contains a schematic of the closed two-phase flow loop that was installed on the ISS. The loop is filled with n-Perfluorohexane (nPFH), a specific isomer of Perfluorohexane. A more commonly known Perfluorohexane-based fluid is FC-72, a mixture of different Perfluorohexane isomers used in heat transfer applications such as electronics cooling [42]. Specifically, nPFH has been selected to handle electronics cooling and HVAC in aerospace applications, due to its preferable thermal, hydrodynamic, and chemical properties. Additional details concerning nPFH can be found in [43]. The fluid is positively displaced through the loop by a gear pump. Two bypass relief valves are connected in parallel across the pump and are set to crack open if the pressure differential between the pump inlet and outlet exceeds 199.5 kPa and 206.8 kPa. Directly downstream of the pump, a Coriolis flow meter measures the flow rate and provides feedback to the pump to maintain the desired flow rate. The fluid then passes through a filter, before entering the preheater, called the Bulk Heater Module (BHM). A predetermined amount of heat is provided by the BHM via a set of heaters, such that, the fluid enters the FBM with the desired inlet conditions. The BHM is instrumented with thermocouples and Resistance Temperature Detectors (RTDs), which provide feedback to shut the heaters down if the fluid or surface temperatures exceed 100°C or 130°C, respectively. The fluid enters the FBM as a subcooled liquid, absorbs a finite amount of heat, and exits as either a subcooled liquid of higher temperature or a two-phase mixture. Heat gained within the BHM and FBM is rejected to a fluid-to-water heat exchanger, condensing the nPFH back to a subcooled liquid state. Any thermodynamic non-uniformities are eliminated, and entrained vapor bubbles condensed as the nPFH passes through a static mixer, ensuring subcooled liquid entry into the pump.

A T-junction located downstream of the static mixer connects an accumulator to the flow loop. The accumulator is comprised of stainless-steel bellows which contains most of the fluid on one side. The other side is filled with air and its pressure and volume are regulated by an air pump and vent valve. Additionally, a pressure relief valve on the air side is set to crack if the pressure differential between the two sides exceeds 137.9 kPa. The accumulator acts as a reference point for system pressure and dampens flow loop instabilities [44]. Two parallel paths exist between the accumulator T-junction and the pump inlet. One provides a direct route to the pump, which is used during normal operation, while the other reroutes the flow through a degassing contactor, which is only used during degassing. The degassing contactor features a semi-permeable membrane with nPFH flow on one side and an applied vacuum, supplied by the ISS's Vacuum Exhaust System (VES), on the other. Degassing was regularly done prior to testing to eliminate non-condensable gasses from the nPFH and ensure reliable data was obtained.

FBCE is housed within the Fluid Integrated Rack (FIR) onboard the ISS, featured in Fig. 3. Additionally, the FIR contains Space Acceleration Measurement System (SAMS), Confocal Control Unit (CCU), Image Processing Storage Unit – Camera Link (IPSU-CL), and various auxiliary systems and components identified in Fig. 3, including the Environmental Control System (ECS) and Electrical Power Control Unit (EPCU). Prior to delivery to the ISS, components of the flow loop are compacted into six individual FBCE modules and are connected to the FIR, as shown at the bottom of Fig. 3. The individual modules, and their layout on the optics bench within the FIR are shown in Fig. 4. The BHM contains the preheater equipped with two sets (one for backup) of three 120 V heaters and 28 V booster heater. The Fluids System Module – Upper (FMSU) houses the degassing contactor in addition to the components upstream of BHM including gear pump, flow meter, mass flow controller, and filter. The Fluids System Module – Lower (FSML) contains the condenser, static mixer, and accumulator. Cooling water is supplied to the condenser via the ISS Thermal Control System (ITCS) through the FIR's Water Interface Panel (WIP). The components of FSML are located downstream of the Test Module Assembly (TMA), which denotes the FBM for the present study. nPFH exits the TMA and enters the FSML, the FSMU,

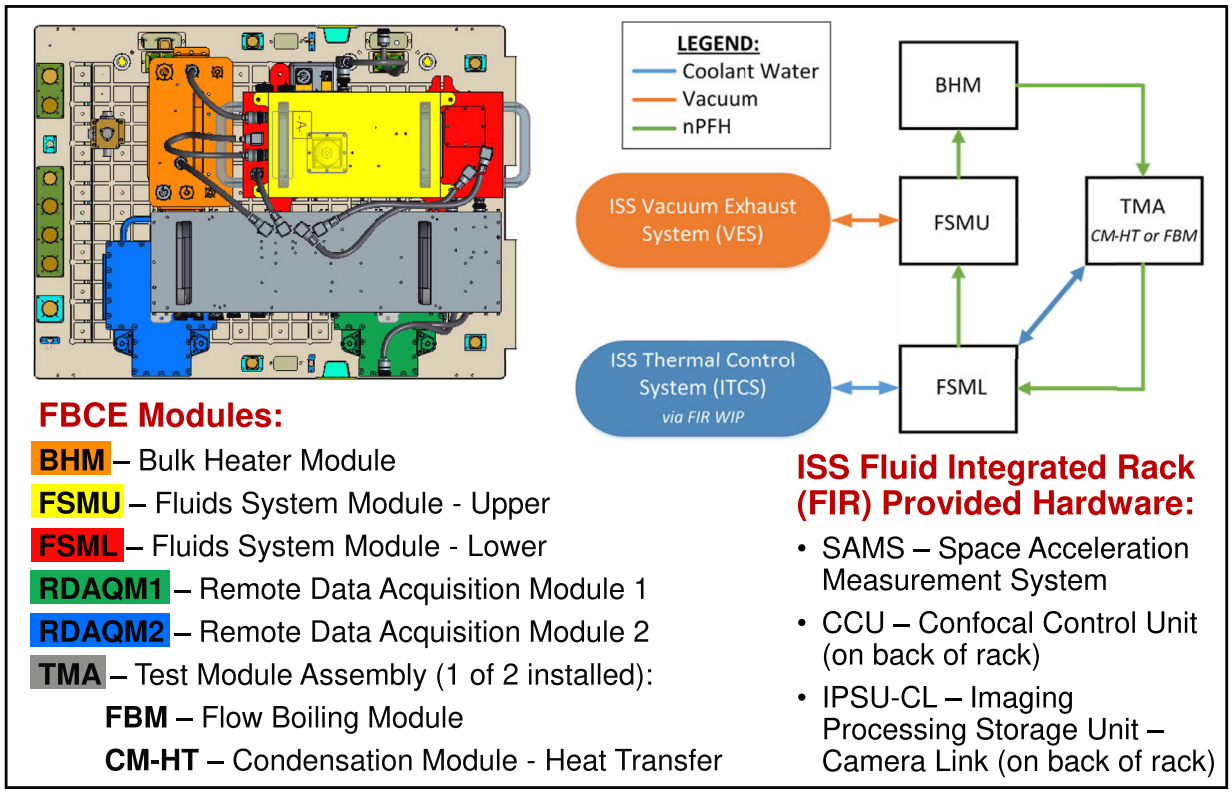

Fig. 4. Layout of main modules of the Flow Boiling and Condensation Experiment (FBCE) on the Optics Bench of the Fluid Integrated Rack (FIR), and ISS provided hardware. The Optics Bench is rotated to vertical upward orientation inside the FIR during the tests.

and the BHM in series, reconditioning the fluid, before entering the TMA again. The final two modules are Remote Data Acquisition Module 1 (RDAQM1) and Remote Data Acquisition Module (RDAQM2). RDAQM1 and RDAQM2 respectively house the UEI data cubes utilized for thermocouple signal conditioning, and the UEI data cube and custom-sensor-supply printed circuit board for signal conditioning of other sensor signals and power distribution.

2.2. Flow boiling module

The FBM is constructed by clamping three transparent polycarbonate plates between two aluminum support plates, which aids against leaks and buckling by dispersing the bolting stress uniformly over the module. A 5.0-mm high and 2.5-mm wide flow channel is milled into the middle piece of polycarbonate. As shown in Fig. 5(a), the entire channel is comprised of a 327.7-mm developing length, containing a honeycomb flow straightener to break up large eddies and align streamlines, a heated length formed by two 114.6-mm long, 15.5-mm wide, and 1.04-thick oxygen-free copper strips which serves as the heated walls, and a 60.7-mm exit length. The construction of the heated walls is depicted in Fig. 5(b). Soldered to the copper strips opposite the flow channel is a set of six 16.4-mm long, 4.5-mm wide, 0.56-mm thick, thick-film resistive heaters in series. Each resistor has a resistance of 188-Ω, and they are electrically connected in parallel to yield uniform heat flux across the copper strip. All other solid-solid contacts, including the copper strips, are made leak-proof with O-rings.

As shown in Fig. 5(c), thermocouples are inserted directly into the heated strip within the 0.9-mm gaps between consecutive heaters; numerical computations have shown the separation between heaters does not impact the heat flux distribution owed to the high thermal conductivity of copper [45]. This heated wall design has been shown to provide fast temperature response and accurate CHF measurement [10,11].

Fig. 6 shows a CAD rendering of the FBM and all components within the FBM box (including the camera system) at the top and a photograph of the final assembled FBM at the bottom.

2.3. Instrumentation and measurement uncertainty

Within the FBM, pressure is measured at five locations by absolute pressure transducers, located at the inlet and out of the module and three locations with the development length (see Fig. 2). The inlet pressure, p_{in}, referenced in this study corresponds to the pressure measurement just upstream of the heated length, and the outlet pressure, p_{out}, to the pressure measurement downstream of the heated length. Inlet temperature, T_{in}, and outlet temperature, T_{out}, of the fluid are measured by type-E thermocouples inserted directly into the fluid near the FBM inlet and outlet, respectively. Type-E thermocouples measure the temperature of the copper strip at seven equidistant locations, as shown in Fig. 5(c). Pressure and temperature are measured by pressure transducers and thermocouples and RTDs, respectively, at various locations along the loop. Additionally, a Coriolis flow meter of range 0 – 60 g/s is used to measure the flow rate.

DC Power is supplied to either one or both heating strips and the bulk heater. Both voltage and current are directly measured by RDAQM2 and are used to calculate the power. As already mentioned, RDAQM2 additionally collects output sensors from various components around the loop, while RDAQM1 exclusively collects thermocouple data. An in-house FBCE flight software monitors and controls both the DAQs and all other instruments, including solenoid valve actuation.

The maximum uncertainty for each measurement of absolute pressure, temperature (using thermocouples), temperature (using

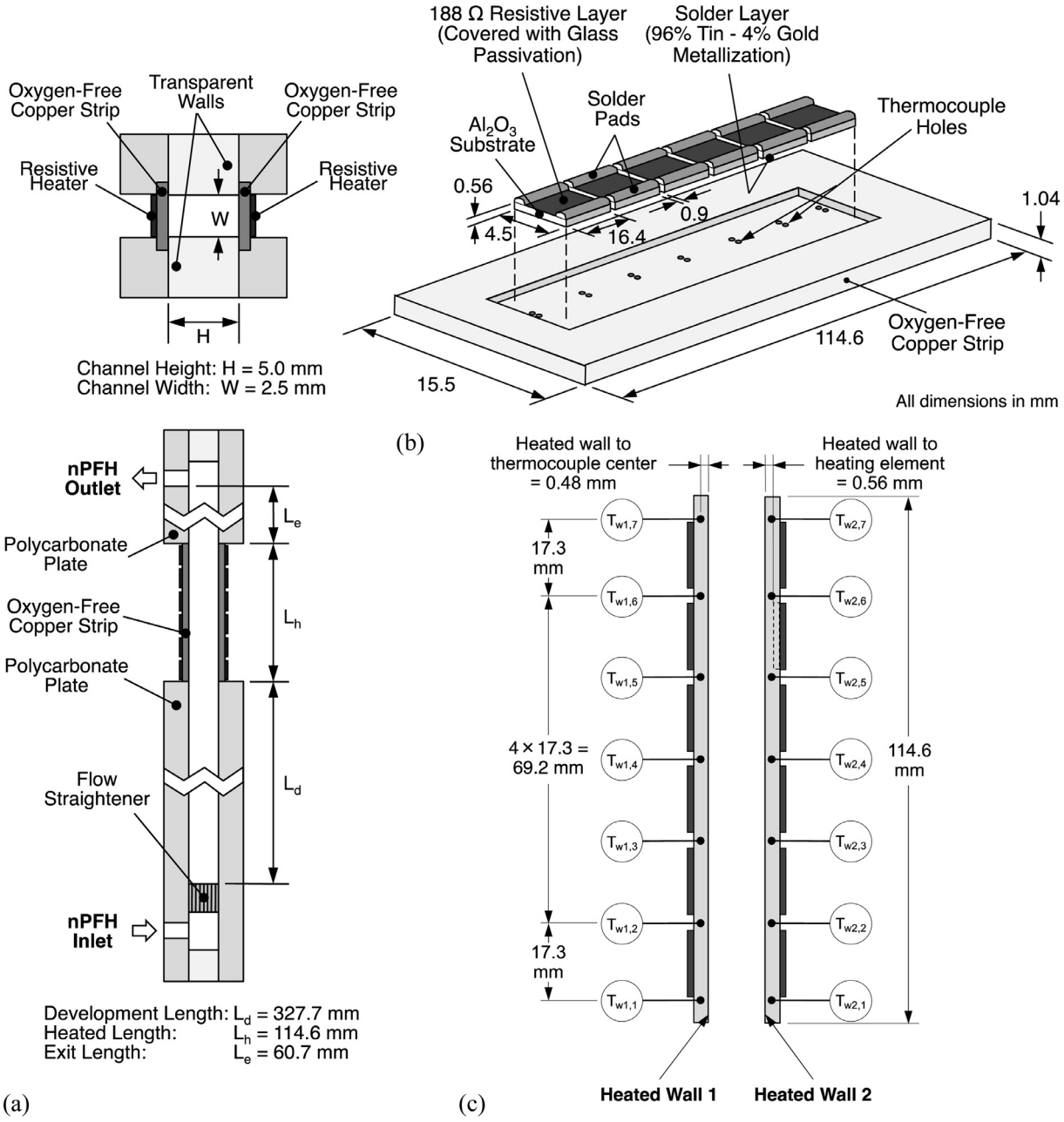

Fig. 5. Schematic representations of (a) overall construction of Flow Boiling Module (FBM), (b) construction of heating strips, and (c) designation of heated walls and local wall temperatures.

RTDs), FBM heater power, BHM heater power, and flow rate is ±0.7 kPa, ±0.5°C, ±0.5°C, ±0.3%, ±0.6%, and ±0.6%, respectively. Approaching CHF, finer increments in heater power are employed compared to early in the boiling curve. The average increase in heat flux which triggered CHF is 1.1 W/cm^2. q''_{CHF} is determined by averaging the heater power of the increment resulting in CHF and the previous steady increment. This results in a CHF isolation error, which is the difference between the true q''_{CHF} and the q''_w provoking CHF, of 0.6 W/cm^2. In some cases, CHF was triggered by an unusually large increase in heat flux. Considering both the uncertainty in measurement of FBM heater power and the isolation error of CHF, the maximum uncertainty in q''_{CHF} is 8.8%, and this corresponds to 4.6 W/cm^2 for an observed q''_{CHF} of 52.1 W/cm^2. However, the average uncertainty in reported q''_{CHF} is 2.2%.

2.4. Operating procedure and data processing

Aside from astronauts installing the FBCE system in the FIR, no in-person operation is needed, and experiments are executed remotely. During off hours, the flow loop is left at a sub-atmospheric pressure, which could allow air to leak into the system and dissolve in the nPFH. Hence, to ensure purity of the fluid, degassing was performed for a few hours prior to performing experiments each testing day, and for longer dedicated periods when deemed necessary.

To initialize each test run, operating conditions are uploaded, and the desired flow rate and pressure is set. Power is supplied to the BHM to achieve the desired inlet temperature or quality. Once steady state is detected, FBM heating is initiated by supplying DC

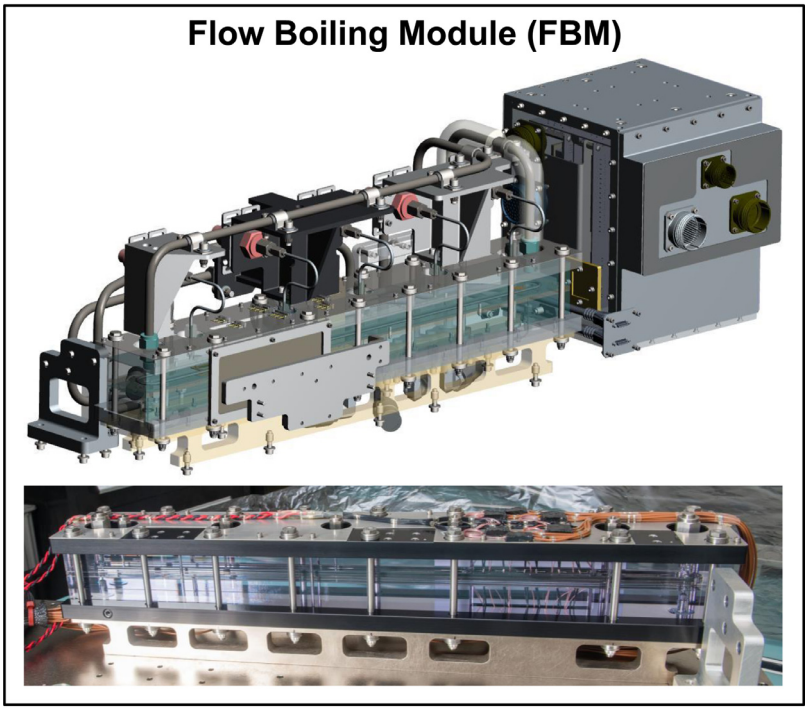

Fig. 6. Full CAD rendering and photograph of Flow Boiling Module.

power to either one or both of the heating strips for either single-sided or double-sided heating, respectively. A duration of 120 – 180 s is allowed for steady-state data collection prior to advancing to the next heating increment. The first 12 increments are predetermined based on an estimated q''_{CHF}, after which, heater power is finely increased by 1.25 W to accurately capture q''_{CHF}. Heater power continues to incrementally increase until CHF is detected by one of the FBM substrate temperatures reaching 122°C, after which FBM heaters are brought to a minimum. Fig. 7 shows an example of temporal records of wall temperatures and heater power recorded during a typical run, from the time the FBM heaters are turned on until CHF. Some notable features of the curves are ONB, the incremental increase in wall temperatures with heater power every 120 s, the attainment of steady state each heat increment after ONB, and heater shutdown once CHF is detected by an unsteady rise in wall temperature. CHF is classically defined as the heat flux which leads to an unsteady and uncontrollable rise in surface temperature at the transition to film boiling. However, for safety, CHF is defined as the heat flux which results in at least one local strip temperature reaching 122°C.

For each heat increment, the final 20 s of data are averaged to obtain steady values. The fluid enthalpy is determined by

$$h_{in} = h|_{T_{in}, p_{in}} \tag{1}$$

Thermophysical properties of nPFH are evaluated using NIST-REFPROP [46]. Energy balance over the FBM yields the following expression for outlet enthalpy,

$$h_{out} = h_{in} + \frac{q''_w P_h L_h}{\dot{m}}, \tag{2}$$

where q''_w is wall heat flux, $\dot{m}$ mass flow rate through FBM and L_h heated length. P_H corresponds to the heated perimeter of the channel and is defined as

$$P_h = \begin{cases} W, & \text{single-sided heating} \\ 2W, & \text{double-sided heating} \end{cases}, \tag{3}$$

where W is the channel width. As detailed in [47], the design of FBM mitigates heat loss from the module. The copper strips are surrounded by polycarbonate, except for a thin gap where thermocouples and heater leads are connected. Heat transfer to the insulating polycarbonate and the stagnant air directly above the heater would be negligibly small to that to the nPFH. This was demonstrated in a previous FBCE paper which extensively investigated heat loss [48], albeit with a slightly different module featuring a slightly shorter heated length and only one heated wall. It was found that the maximum heat loss from the module was 0.2% of the power supplied, which is within the measurement uncertainty of power, 0.3%. Hence, q''_w is simply determined as the FBM heater power divided by the heated area.

Thermodynamic equilibrium quality is determined by

$$x_e = \frac{h - h_f\big|_p}{h_{fg}\big|_p}, \tag{4}$$

where the inlet and outlet values are determined by setting $h = h_{in}$ and $h = h_{out}$, respectively.

The experimental q''_{CHF} is determined to be the average of the q''_w causing the substrate temperatures to exceed 122°C and the q''_w of the previous steady increment. The true q''_{CHF} will fall somewhere between the two, creating the q''_{CHF} isolation described in Section 2.4. Other operating conditions corresponding to CHF, such as pressure, temperature, and flow rate, are assumed to be the steady operating conditions of the previous step. This is done because flow parameters do not reach steady during the increment triggering CHF, and thus cannot be averaged. The range of CHF datapoints and corresponding operating conditions in this study are reported in Table 1. Cases considered in this study are restricted to $\Delta T_{sub,in} \geq 1$°C, in order to limit the influence of vapor produced by non-equilibrium within the bulk heater. Additionally, cases clearly observed to have two-phase inlet are omitted.

2.5. Flow visualization techniques

Optical access for high-speed video capture of the flow is permitted through the polycarbonate sides of the channel. The polycarbonate was vapor polished to suppress vignetting effects caused

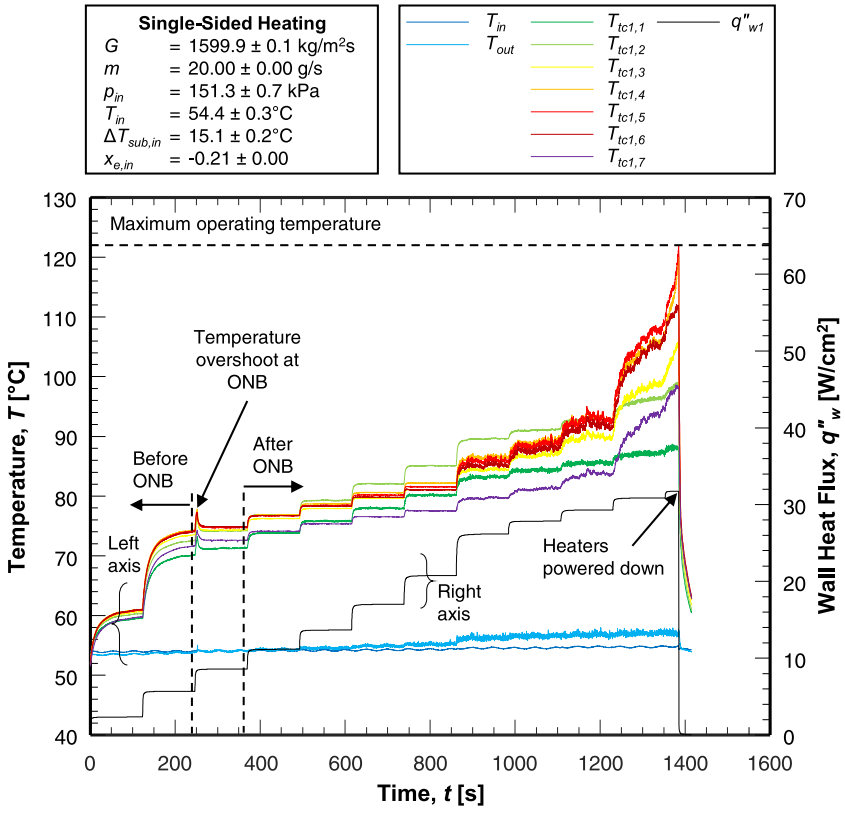

Fig. 7. Temporal variations of fluid inlet, fluid outlet, and heating-strip temperatures for heat flux increments from a minimum to CHF for a typical experimental case. Adapted from [40].

Table 1
Summary of CHF datapoints obtained with subcooled inlet conditions to the FBM's heated section.

	Single-Sided Heating	Double-Sided Heating
Mass velocity, G	200.0 – 3200.0 kg/m^{2}s	199.0 – 3200.0 kg/m^{2}s
Mass flow rate, $\dot{m}$	2.50 – 40.00 g/s	2.49 – 40.00 g/s
Inlet pressure, p_{in}	124.8 – 164.2 kPa	127.6 – 176.7 kPa
Inlet temperature, T_{in}	23.5 – 68.9°C	25.5 – 68.5°C
Inlet subcooling, $\Delta T_{sub,in}$	2.6 – 45.6°C	4.0 – 43.7°C
Inlet quality, $x_{e,in}$	-0.61 – -0.04	-0.58 – -0.06
Outlet pressure, p_{out}	119.0 – 156.2 kPa	117.5 – 165.8 kPa
Outlet temperature, T_{out}	34.8 – 69.7°C	43.1 – 71.8°C
Outlet subcooling, $\Delta T_{sub,out}$	0.00 –34.5°C	0.00 – 20.6°C
Outlet quality, $x_{e,out}$	-0.45 – 0.09	-0.26 – 0.41
Critical heat flux, $q"_{CHF}$	10.1 – 53.9 W/cm^2	17.3 – 48.9 W/cm^2
Number of data points, N	62	74

by the copper heaters and O-rings within the module. The high-speed camera continuously records throughout the entire experiment, in anticipation of CHF occurring. At the end of each heating increment, the latest 1.0-s of video captured prior to proceeding to the next heat increment is saved. Once CHF is detected, the latest 7.0-s of video is saved to better capture the flow transients leading to CHF. Images were recorded at a frame rate of 2000 frames/s and a shutter speed of 10 μs. A F#0.95–25 mm focal length lens was used and images were captured at a resolution of 2040 × 164 pixels. The other polycarbonate side wall is backlit with blue light emitting diodes (LEDs), with an intermediate Teflon sheet serving as a light shaping diffuser and is shown in the CAD rendering in Fig. 6. Each image was then externally processed to enhance the visibility of flow features.

3. Flow visualization results and discussion

This section presents flow visualization images of the FBM's heated length near CHF. Sequential images of flow patterns are shown approaching CHF with $q"_w > 90\%\ q"_{CHF}$ (labeled as "CHF–") and after CHF occurs (labeled as "CHF+"). A variety of operating conditions are selected to provide a thorough investigation of the parametric effects of mass velocity, inlet subcooling, and inlet pressure on flow patterns around CHF in microgravity. These observations elucidate both parametric trends and physical mechanisms of CHF. Time interval between consecutive images is 2 ms unless noted otherwise, and each set of images is accompanied by its corresponding operating conditions at CHF as described in Section 2.5.

Schematic representations of single- and double-sided heating configurations are shown in Fig. 8, and all flow visualization im-

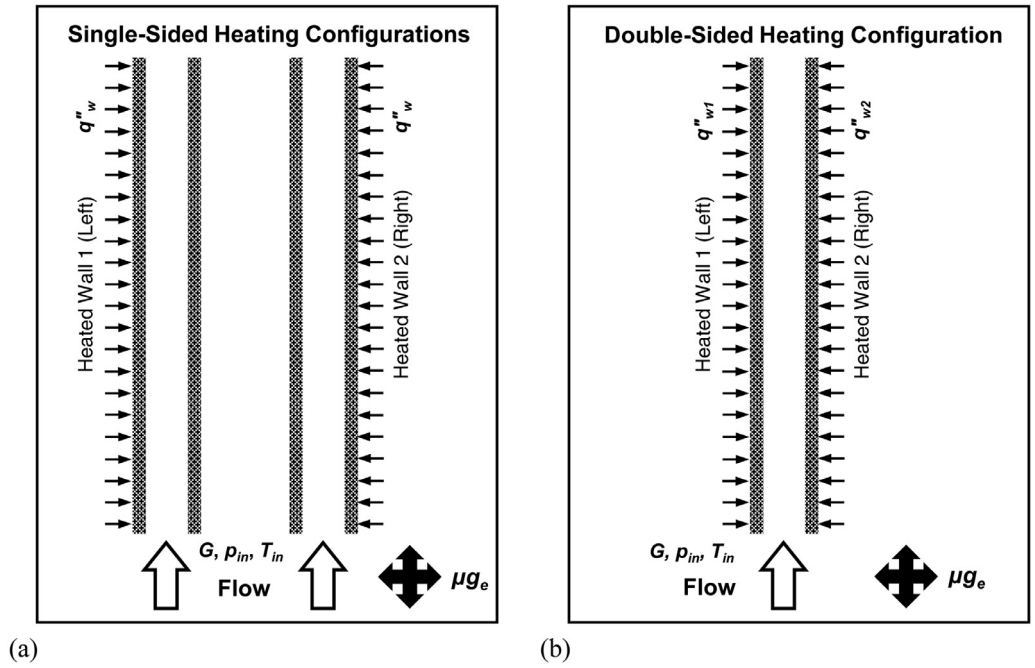

Fig. 8. Schematic representation of (a) single-sided and (b) double-sided heating configurations.

ages in this paper conform to this format. Flow enters from the bottom end of the channel at the specified inlet conditions. It is noted, for single-sided heating, the choice of wall influences neither the flow patterns nor the heat transfer performance [40]. A preliminary example of flow visualization and an outline of the liquid-vapor interface at CHF- and CHF+ for single-sided heating are presented in Fig. 9(a) and (b) respectively for relatively low and high subcooling. The liquid-vapor interface is wavy as vapor protruding from the heated, left wall forms the wave crests. The troughs of the wavy interface are comprised of gaps in the vapor layer, called *wetting fronts*, which allow liquid to contact the heated wall. In Fig. 9(a), a wetting front exists halfway through the channel, and the interface touches the heated wall. Boiling that occurs within wetting fronts is hypothesized to be the primary source of cooling for the heated wall. In the upstream region of the channel, a fairly continuous vapor layer forms, albeit with some breaks as individual vapor structures in close proximity to each other begin to coalesce. At CHF+, once the continuous vapor layer fully matures in the upstream portion of the channel, a continuous vapor layer shields the wall from the liquid and no wetting fronts exist downstream. A similar phenomenon is observed in Fig. 9(b) at a higher inlet subcooling, where wetting fronts are better preserved. At CHF-, wetting fronts are present throughout the channel, even in the downstream section. However, at CHF+, wetting fronts are sustained in the upstream region, but lose contact in the downstream portion of the channel. This phenomenon will be further investigated in the subsequent figures, featuring flow visualization sequences at CHF- and CHF+ for a variety of operating conditions.

3.1. Single-Sided heating

3.1.1. Effects of inlet subcooling for single-sided heating

Fig. 10 presents image sequences for single-sided heating at an intermediate mass velocity of G = 800.0 – 805.1 kg/m^{2}s, and a variety of inlet subcoolings. At the lowest subcooling of $\Delta T_{sub,in}$ = 6.0°C, shown in Fig. 10(a), liquid enters the channel and almost immediately boils at the heated section inlet. Vapor travels downstream along the heated wall, coalescing and growing until a mostly continuous vapor layer occupies the majority of the heated wall. At CHF-, a wetting front clearly exists in the upstream region of the channel and slides downstream along the heated wall. Wetting fronts accelerate as boiling ensues, and eventually lift off the heated wall downstream due to vapor production preventing liquid replenishment. As wetting fronts continue to lift off the wall downstream, the onus of heat dissipation shifts to wetting fronts further upstream. Occasionally wettings fronts reattach to the heated wall downstream to provide temporary cooling, however they are not sustained. At CHF+, heat flux is sufficiently high that wetting fronts are contained further upstream, preventing cooling of the heated wall downstream, resulting in copper-strip thermocouples escalating to the experimental upper limit of 122°C.

Subsequent subfigures show cases with monotonically increasing inlet subcooling. Figs. 10(b) and (c) show image sequences with inlet subcooling of $\Delta T_{sub,in}$ = 9.5°C and 14.9°C, respectively. In both subfigures, flow patterns around CHF closely resemble those in Fig. 10(a), regardless of the higher inlet subcooling. Expectedly, the near identical flow patterns correspond to similar q''_{CHF} for these cases. Elevating the inlet subcooling to $\Delta T_{sub,in}$ = 23.7°C, shown in Fig. 10(d), results in a thinner vapor layer in the channel downstream at CHF+. At this point, the effect of subcooling is strong enough to enhance q''_{CHF}.

Fig. 10(e) contains images with an even higher inlet subcooling of $\Delta T_{sub,in}$ = 28.9°C. Higher inlet subcooling increases the effect of condensation at the liquid-vapor interface away from the heated wall, and the amount of heat required to vaporize liquid. This yields a thinner vapor along the heated wall and a significant increase in q''_{CHF} compared to the preceding subfigures. At CHF-, numerous wetting fronts are present along the heated wall throughout the entire channel. At CHF+, the strong condensing potential of bulk fluid helps two wetting fronts traverse the entire channel to the exit, concentrating heat dissipation at the remaining wetting fronts. At the end of the sequence, the most downstream wetting front is extinguished, forming a continuous vapor layer along the wall. Fig. 10(f), features the highest subcooling of $\Delta T_{sub,in}$ = 38.3°C. At a high degree of subcooling, wetting fronts

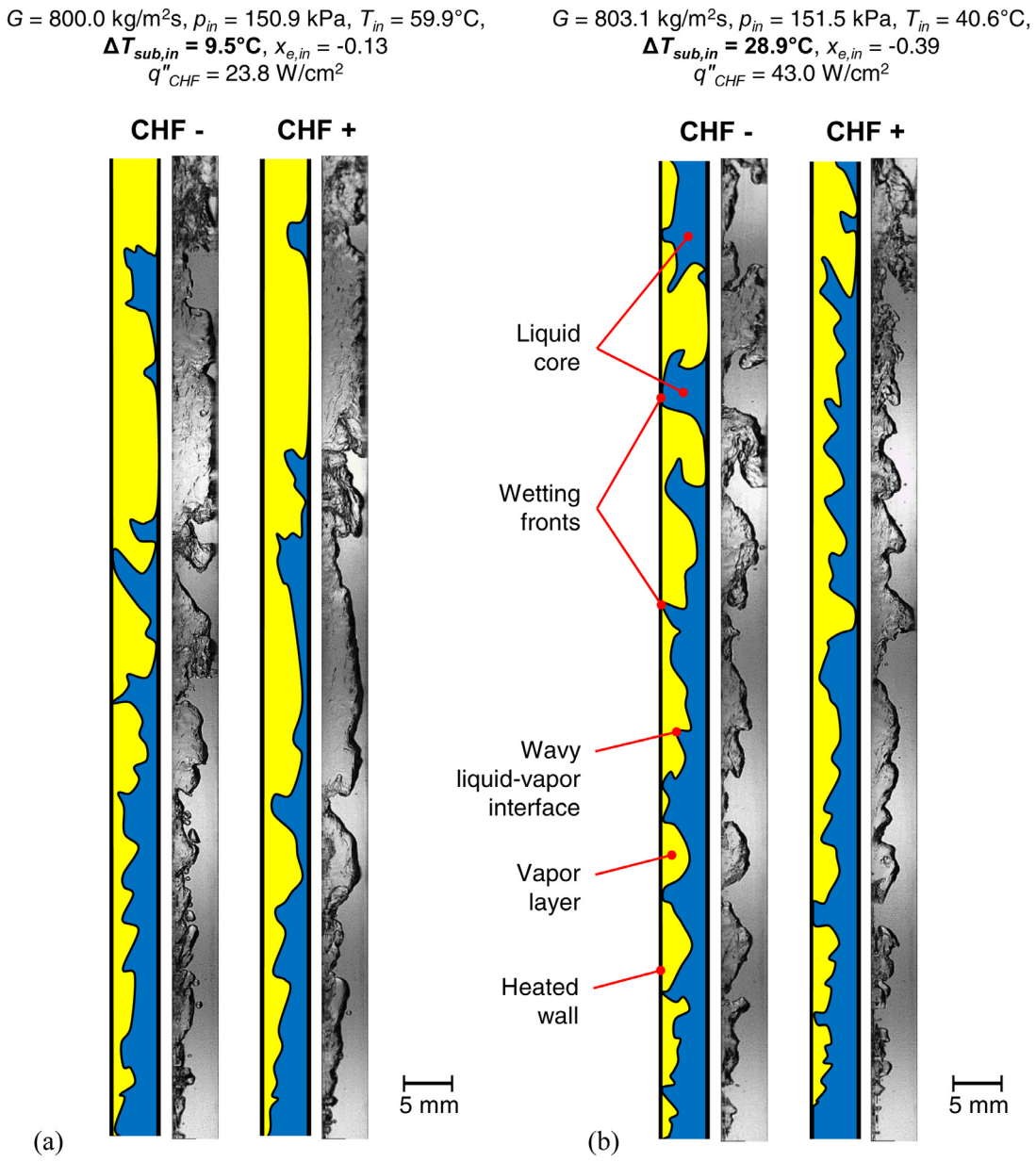

Fig. 9. Flow visualization and outline of liquid-vapor interface at CHF- and CHF+ during single-sided heating with an intermediate mass velocity of $G \approx 801.6$ kg/m^{2}s and an inlet subcooling of $\Delta T_{sub,in}$ = (a) 9.5°C and (b) 28.9°C. Channel width is 5 mm.

persist through the channel. At CHF+, the distance between successive wetting fronts downstream (or the wavelength of the interface) is longer than at CHF-. At this point, large vapor patches preclude sufficient liquid contact to prevent local copper-strip thermocouples from reaching 122°C.

3.1.2. Effects of mass velocity for single-sided heating

Fig. 11 presents similar image sequences for single-sided heating as Fig. 10, but focusing on the near-saturated cases, $\Delta T_{sub,in}$ = 3.3 – 4.7°C, at a variety of mass velocities. At the lowest mass velocity of G = 200.0 kg/m^{2}s, shown in Fig. 11(a), a smooth continuous vapor structure occupies the channel, with a thin liquid layer on the adiabatic wall. The predominantly vapor downstream produced at the combination of low inlet subcooling and low mass velocity results in an extremely low $q"_{CHF}$ of 10.1 W/cm^2. Increasing the mass velocity to G = 399.9 kg/m^{2}s, shown in Fig. 11(b), increases $q"_{CHF}$ to 17.5 W/cm^2. This is owed to increased flow inertia, moving wetting fronts further into the channel and at a faster rate, decreasing the wavelength of the interface, compared to Fig. 11(a). This trend monotonically continues as mass velocity is further increased, Fig. 11(c) and (d), with respective mass velocities of G = 799.9 and 1599.9 kg/m^{2}s. In Fig. 11(d), the vapor structures downstream appear darker and more chaotic than in cases with lower mass velocity, due to the turbulence produced at higher mass velocities. Similar to the effects of inlet subcooling, higher mass velocity increases interfacial shear stress and thins the vapor layer, specifically in the upstream region. However, condensation at the liquid-vapor interface is insignificant at low subcooling and the vapor layer grows large enough to reach the opposite adiabatic wall in the downstream section.

The highest mass velocity of G = 2400.0 kg/m^{2}s is depicted in Fig. 11(e). At CHF-, wetting fronts in the upstream region of the channel slide along the heated wall and lift off by the end of the channel. At CHF+, in the first image, one wetting front exists

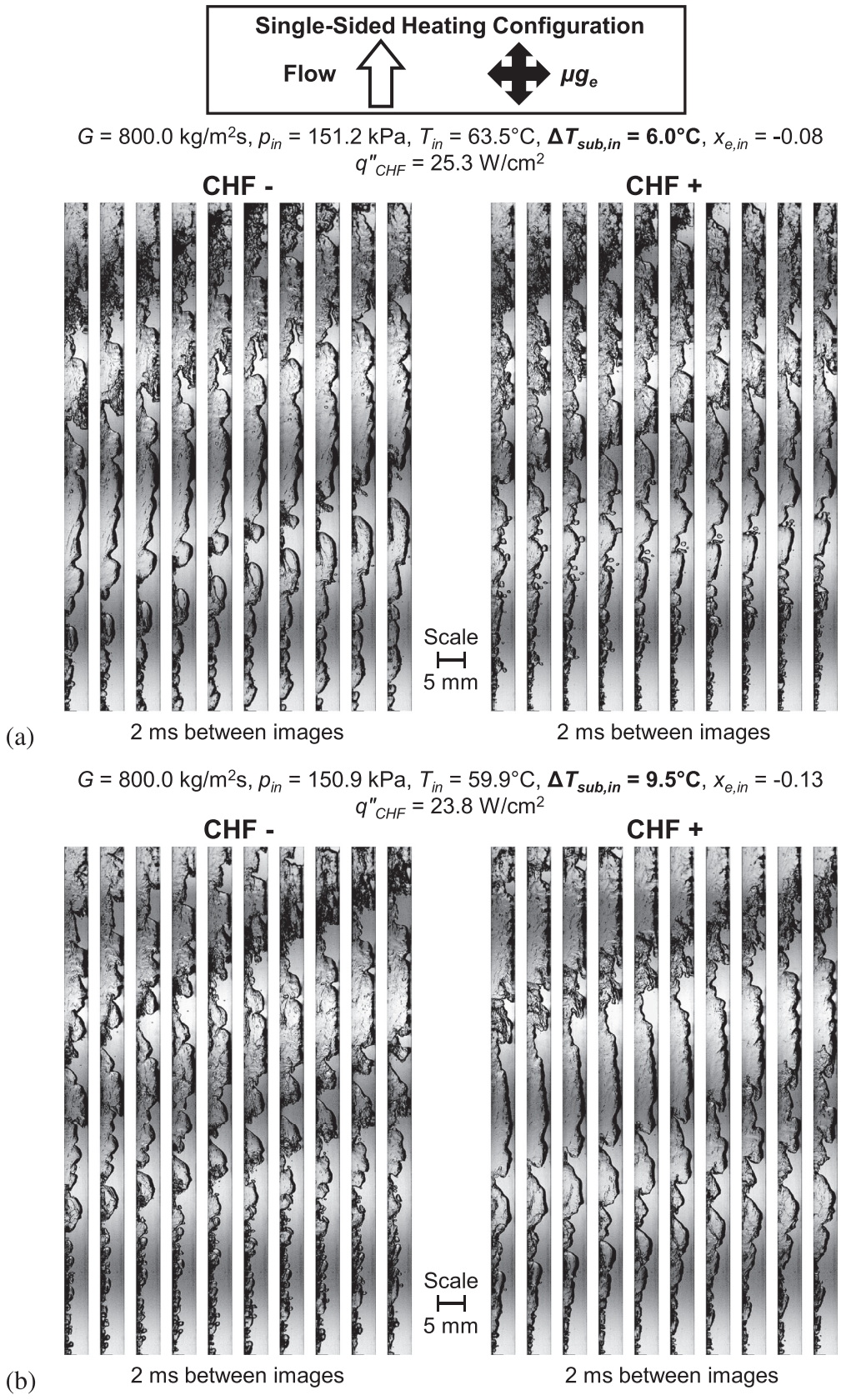

Fig. 10. Flow visualization image sequences around CHF for inlet subcoolings of $\Delta T_{sub,in}$ = (a) 6.0°C, (b) 9.5°C, (c) 14.9°C, (d) 23.7°C, (e) 28.9°C, and (f) 38.3°C at fixed intermediate mass velocity and high inlet pressure with single-sided heating. Time interval between successive images is mentioned below each sequence. Channel width is 5 mm.

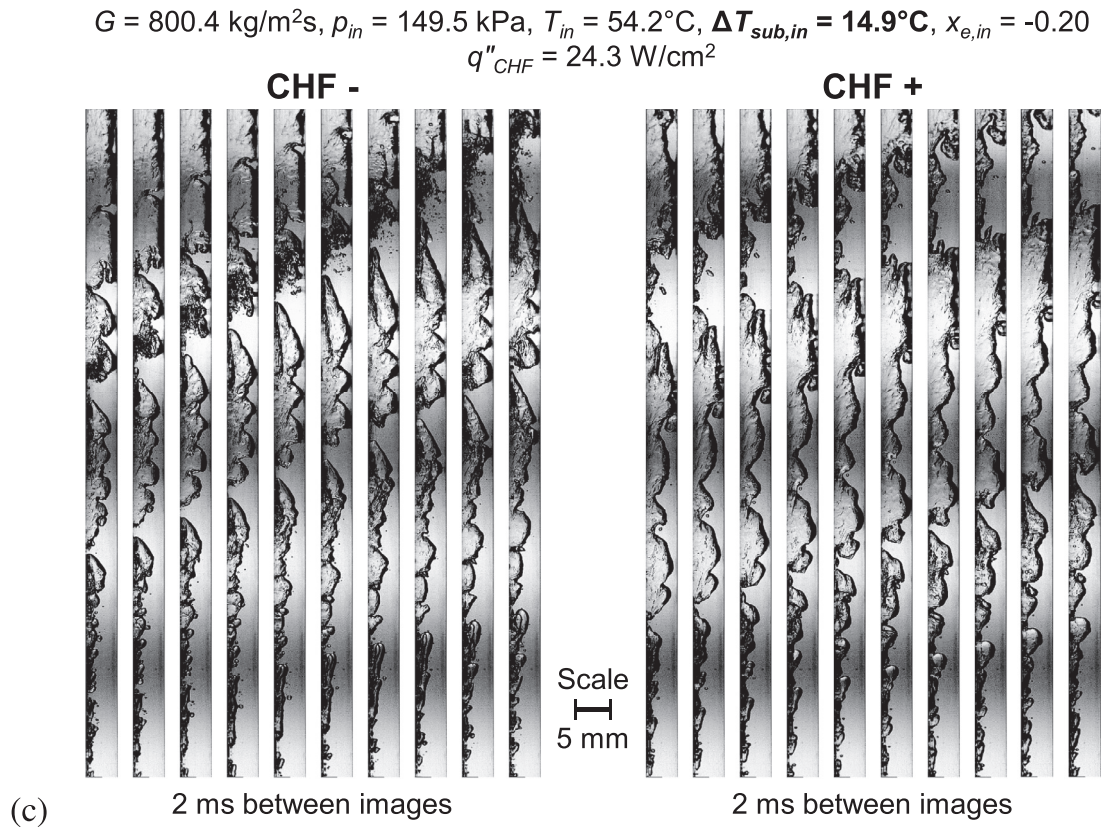

Fig. 10. Continued

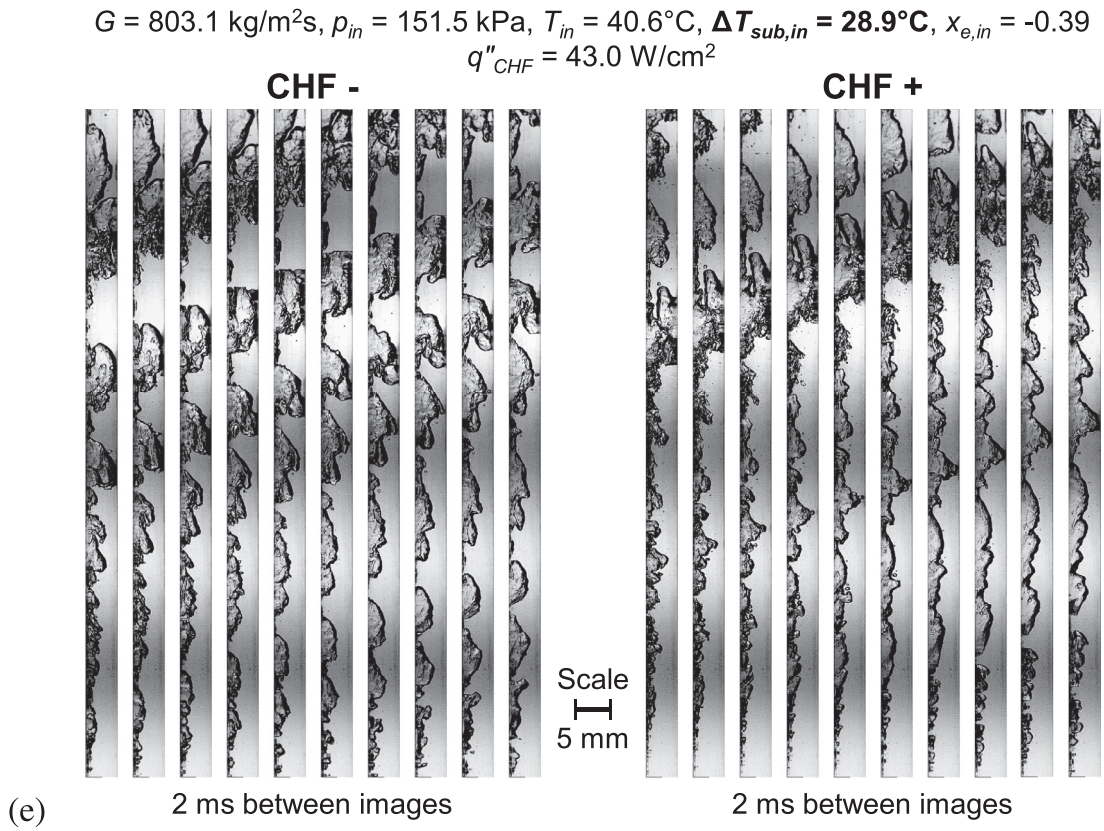

Fig. 10. Continued

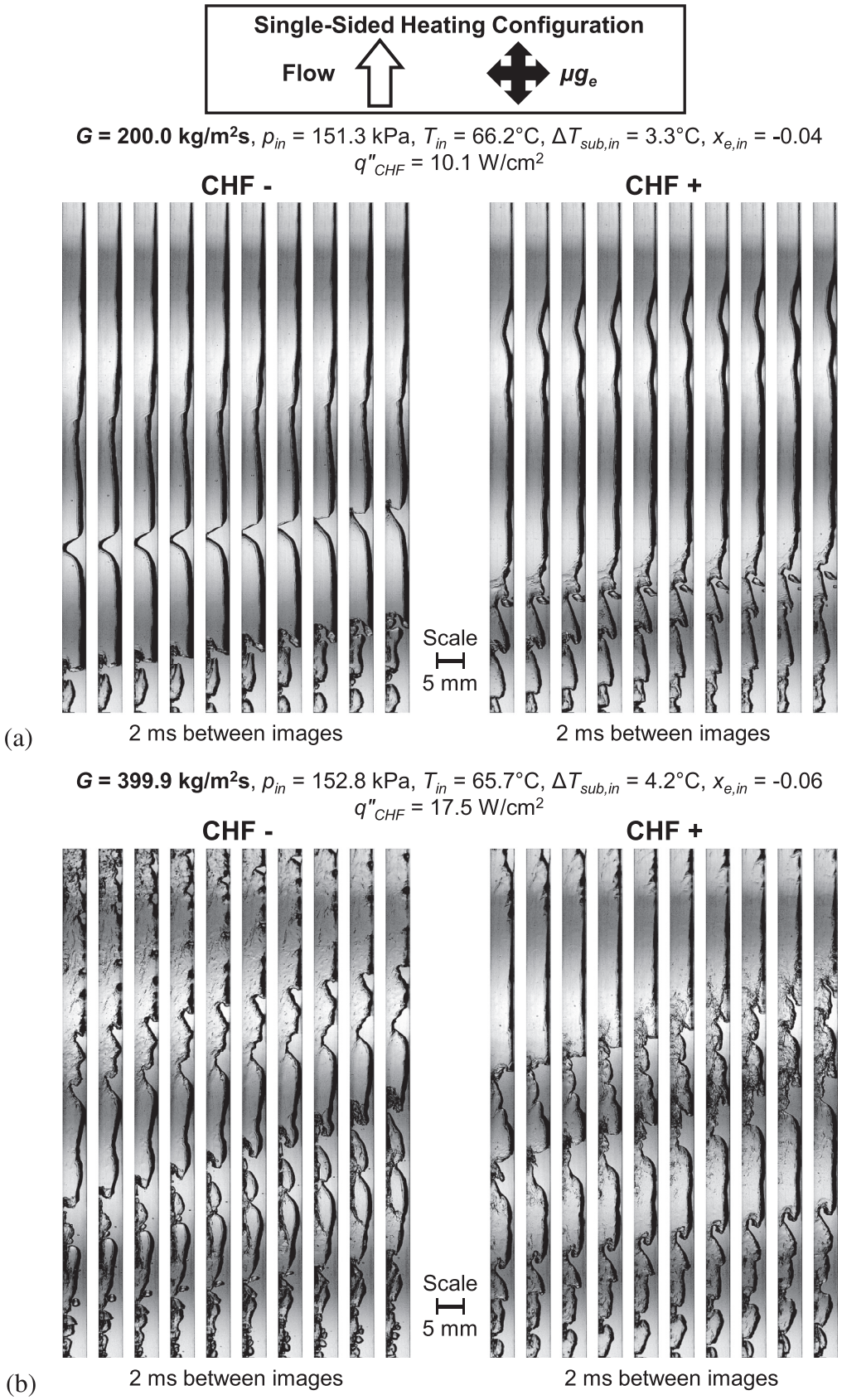

Fig. 11. Flow visualization image sequences around CHF for mass velocities G = (a) 200.0, (b) 399.9, (c) 799.9, (d) 1599.9, and (e) 2400.0 kg/m²s at fixed low inlet subcooling and high inlet pressure with single-sided heating. Time interval between successive images is mentioned below each sequence. Channel width is 5 mm.

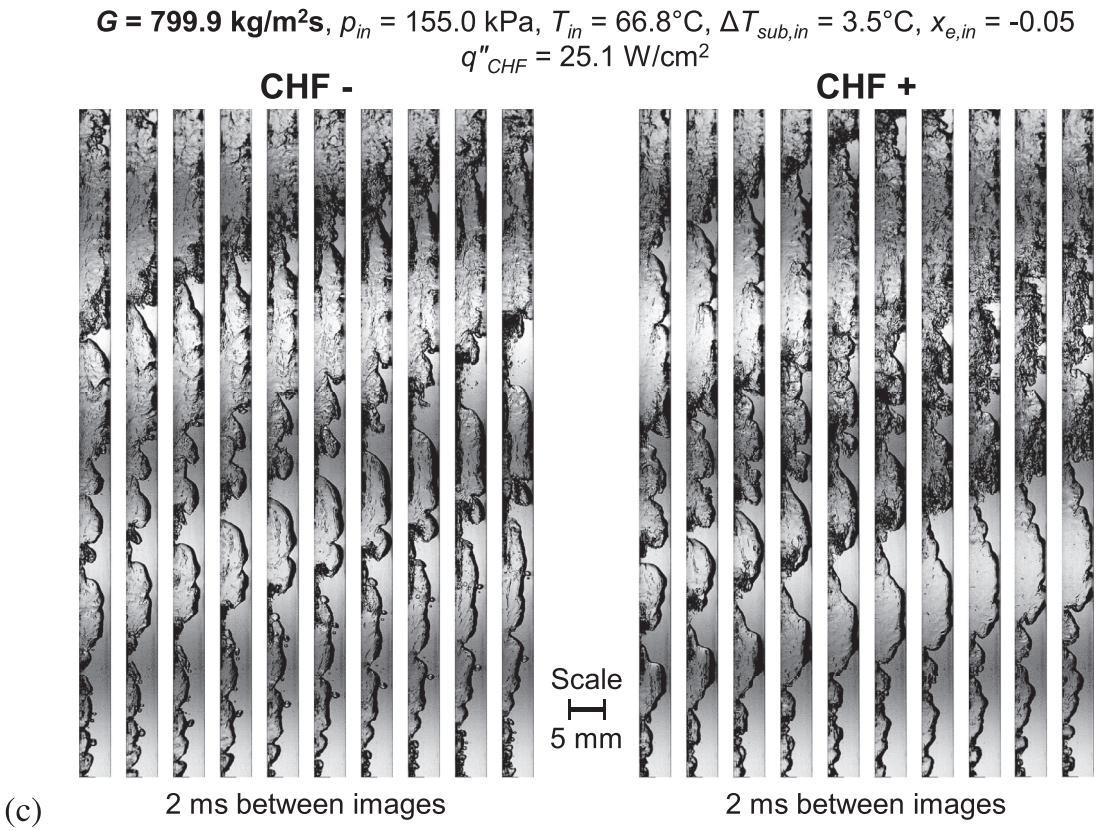

(c)

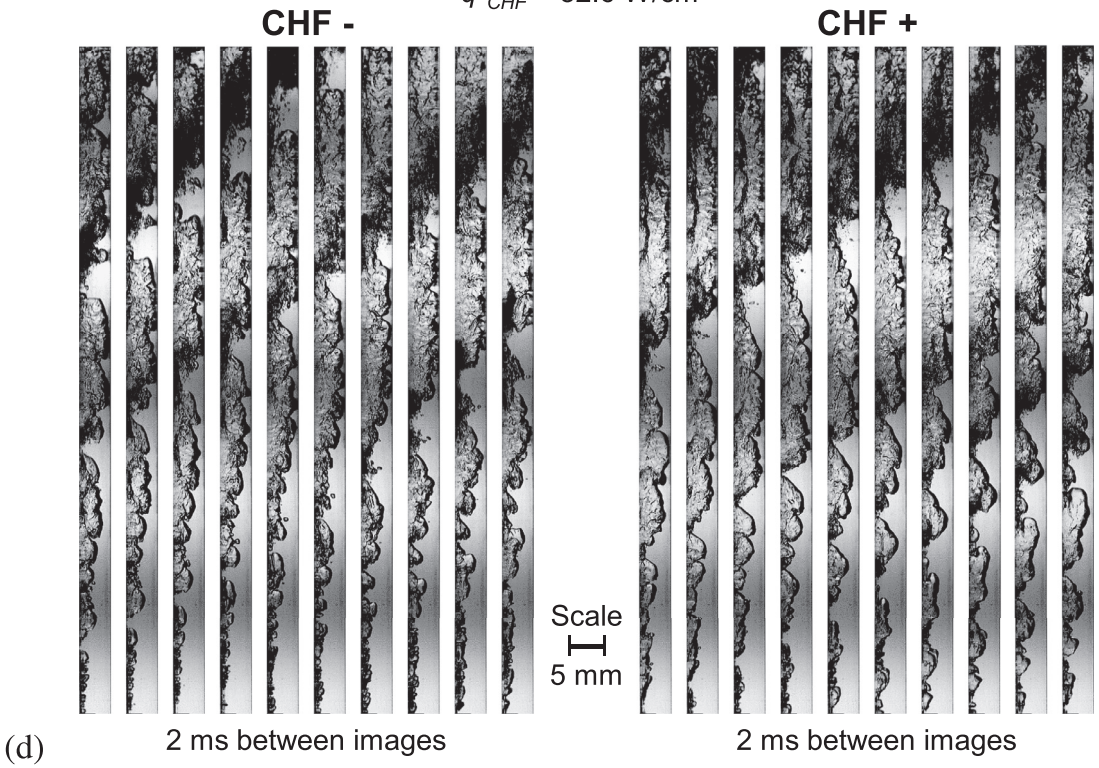

(d)

Fig. 11. Continued

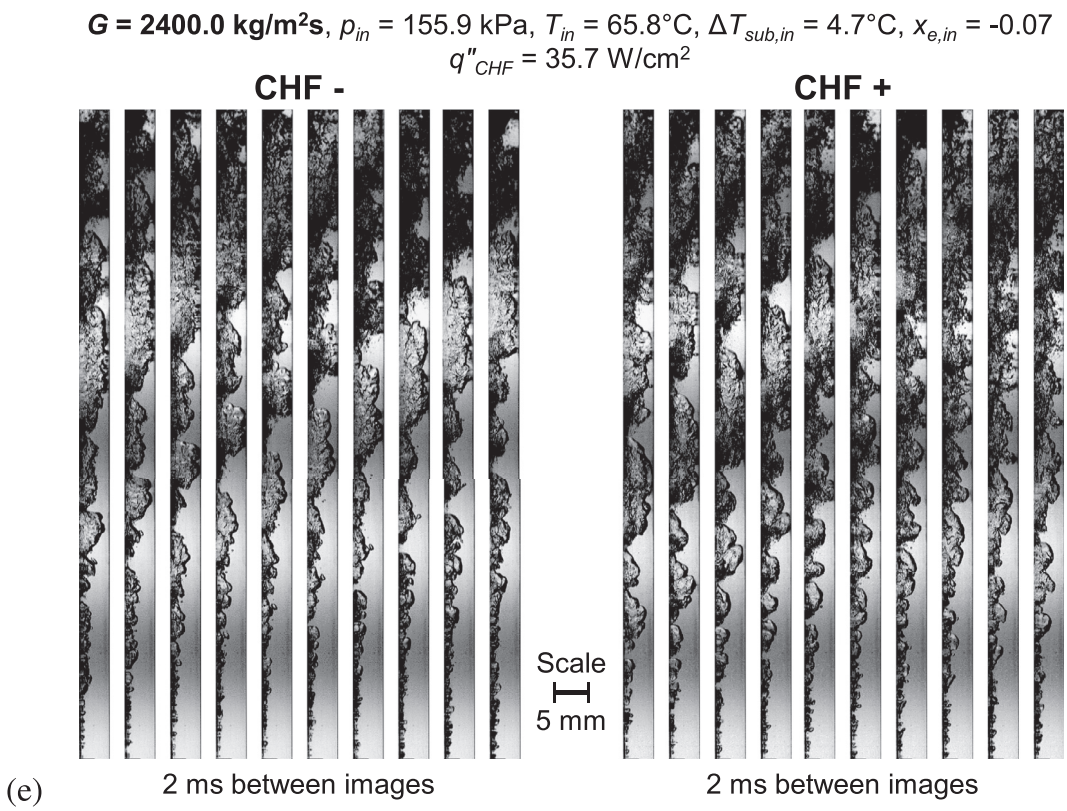

Fig. 11. Continued

halfway along the channel; this exits during the sequence. Other wetting fronts lift off the wall and trigger CHF, regardless of boiling in the upstream portion of the channel prior to the formation of the continuous vapor layer.

Fig. 12 displays image sequences around CHF with an elevated inlet subcooling of $\Delta T_{sub,in}$ = 13.0 – 14.9°C, for different mass velocities. In Fig. 12(a), G = 202.0 kg/m^{2}s, clear wetting fronts are present at CHF-, as opposed to CHF+, where a wetting front midway through the channel is extinguished and liquid loses contact with the heated wall. Increasing the mass velocity to G = 400.2 kg/m^{2}s, Fig. 12(b), the waviness of the interface increases. At CHF-, downstream wetting fronts accelerate towards the outlet as rigorous boiling occurs within them. Once downstream wetting fronts lift off the heated wall, heat dissipation is entrusted to upstream wetting fronts. At CHF+, liquid occasionally penetrates the vapor layer that covers the wall but is quickly separated by rapid vapor production. Subsequent increases in mass velocity to G = 800.4, 1600.1, and 2400.0 kg/m^{2}s, respectively shown in Figs. 12(c-e), result in a thinner, wavier vapor layer and greater $q"_{CHF}$. In Figs. 12(d) and (e), a short region upstream of the continuous vapor layer, where local subcooling is the highest, permits liquid contact with the heated wall. Regardless, CHF occurs when downstream wetting fronts are removed from the wall downstream, as depicted in CHF+ for each subfigure, respectively.

3.1.3. Effects of inlet pressure for single-sided heating

Fig. 13 shows images of single-sided heating at a low inlet subcooling of $\Delta T_{sub,in}$ = 3.5 – 6.4°C, for different mass velocities, similar to Fig. 11. However, the image sequences in Fig. 13 feature lower inlet pressures of p_{in} = 131.5 – 137.2 kPa compared to 151.3 – 155.9 kPa in Fig. 11. The $q"_{CHF}$ at each mass velocity in Figs. 13(a-e) are similar to the corresponding case in Fig. 11(a-e). The largest deviation is seen at the lowest mass velocity of G = 200.0 kg/m^{2}s, in Fig. 13(a). For this case, a slightly higher inlet subcooling of $\Delta T_{sub,in}$ = 6.4°C was adopted to maintain single-phase inlet during the experiments, as non-equilibrium effects within the bulk heater produced vapor at low inlet subcooling and low mass velocity. Overall, inlet pressure in the tested range has a weak influence on both flow patterns near CHF and $q"_{CHF}$.

3.2. Double-Sided heating

3.2.1. Effects of inlet subcooling for double-sided heating

Fig. 14 shows image sequences for double-sided heating with an intermediate mass velocity of G = 800.0 – 802.8 kg/m^{2}s, at a variety of inlet subcoolings. Fig. 14(a) features fluid entering the channel with a low inlet subcooling of $\Delta T_{sub,in}$ = 5.7°C, which promotes rapid growth of the vapor layer and merging of the vapor layers in the upstream region of the channel. Prior to the vapor layers merging, the wavy liquid-vapor interface, already observed during single-sided heating, develops along each heated wall. At CHF-, a vapor layer immediately forms along each heated wall and grow towards the center of the channel. Wetting fronts slide along the heated wall and provide cooling. As they reach the merging point, the remaining liquid becomes entrained within the vapor, and liquid-vapor mixture propagates downstream; note that this mixture initially exists as a wavy structure in-between the merging wavy vapor layers. Wetting fronts absorbed into the downstream mixture are replaced by newly formed ones upstream. At CHF+, flow patterns are similar to CHF- and the channel is predominantly filled with the liquid-vapor mixture formed by merged wavy vapor layers. However, the left wall does not become rewetted and is blanketed by vapor, resulting in CHF.

Higher inlet subcoolings of $\Delta T_{sub,in}$ = 10.9°C and 13.6°C are shown in Fig. 14(b) and (c), respectively. Increasing the inlet subcooling slows the growth of the vapor layers and pushes their merging point further downstream. However, the majority of the channel is still occupied by the liquid-vapor mixture, constraining

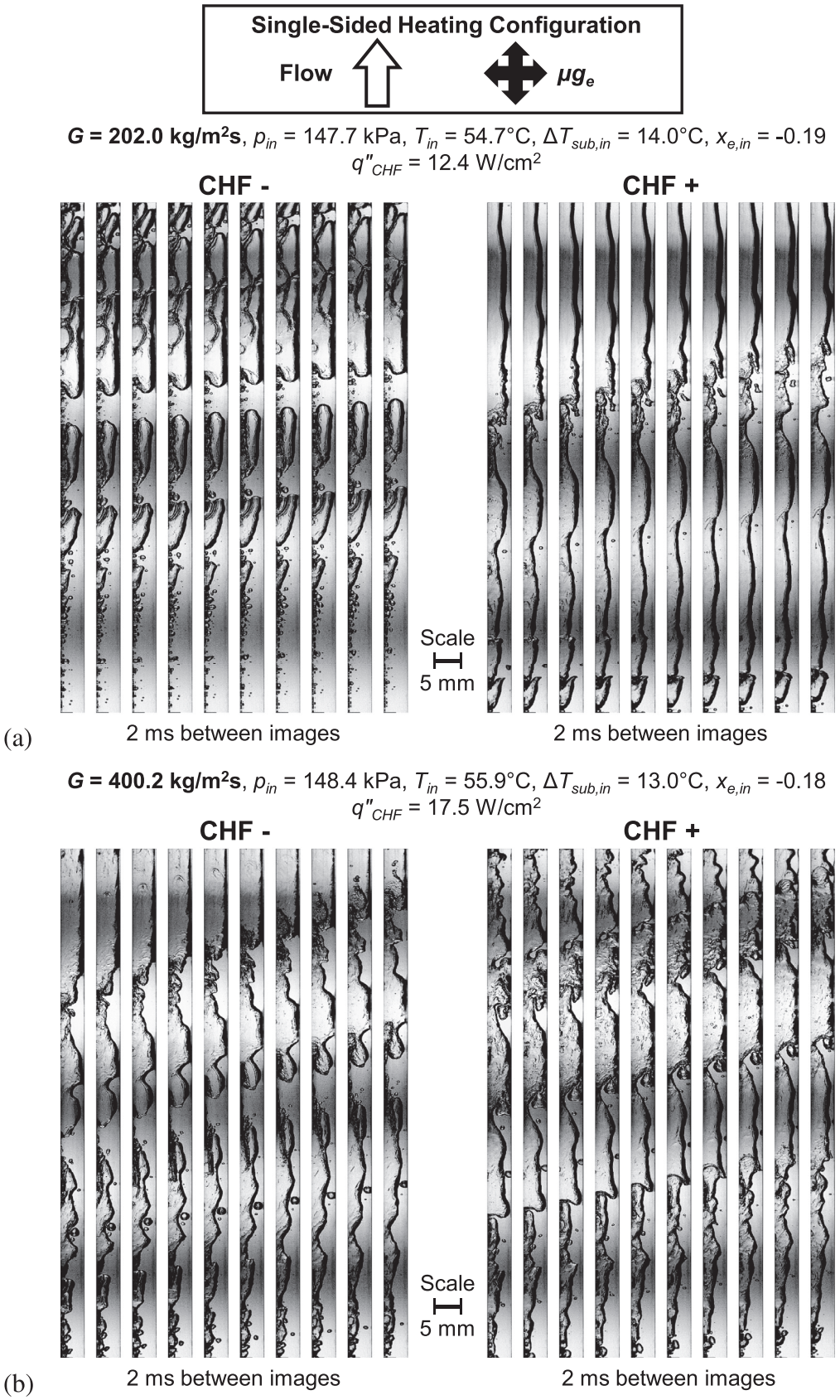

Fig. 12. Flow visualization image sequences around CHF for mass velocities G = (a) 202.0, (b) 400.2, (c) 800.4, (d) 1600.1, and (e) 2400.0 kg/m²s at fixed moderate inlet subcooling and high inlet pressure with single-sided heating. Time interval between successive images is mentioned below each sequence. Channel width is 5 mm.

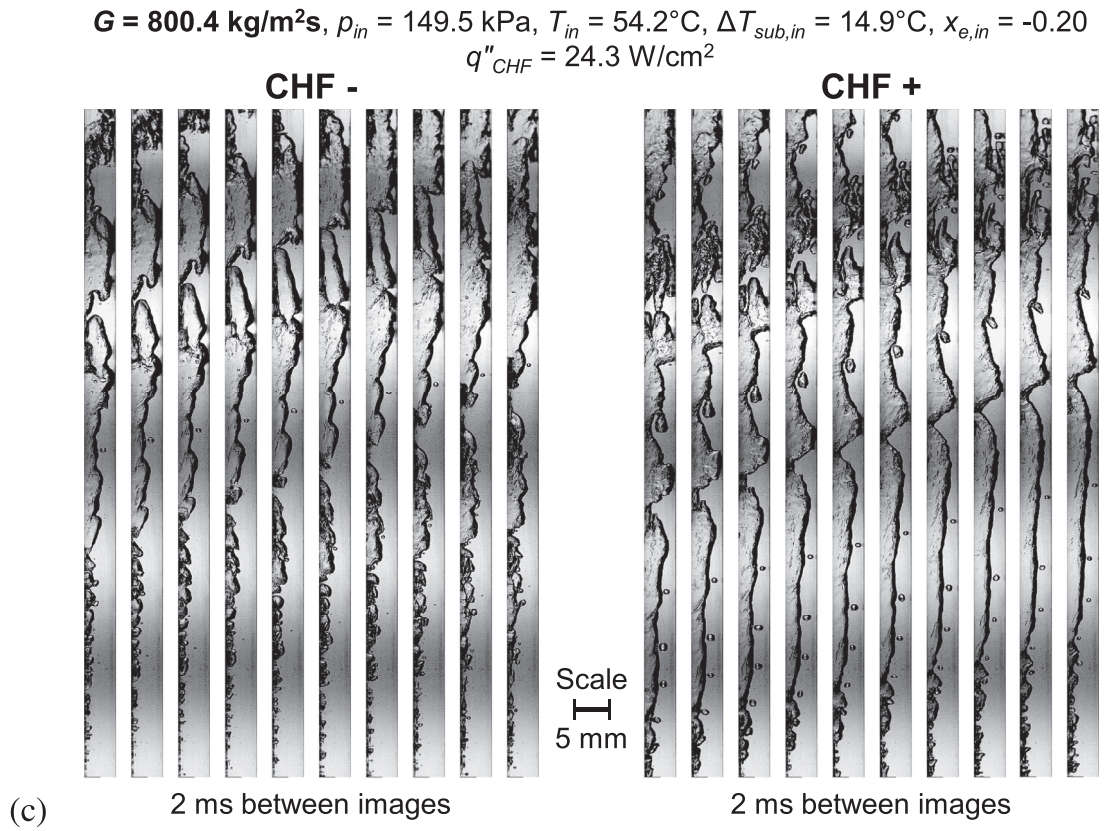

(c)

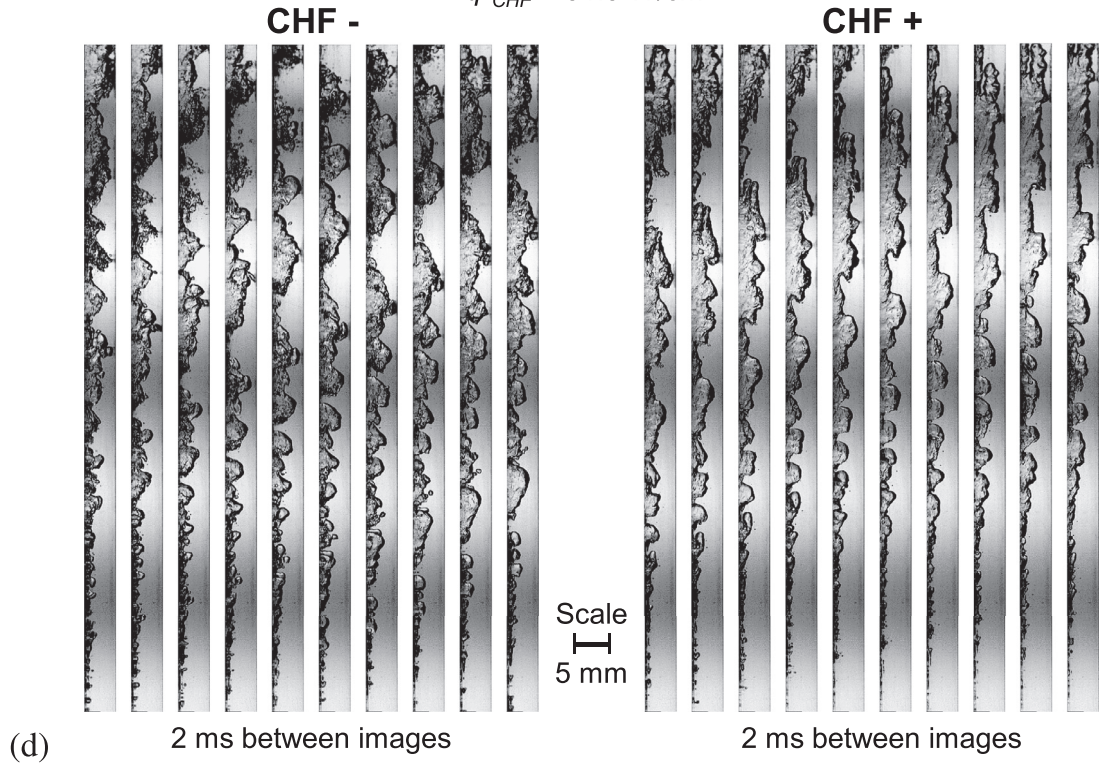

(d)

Fig. 12. Continued

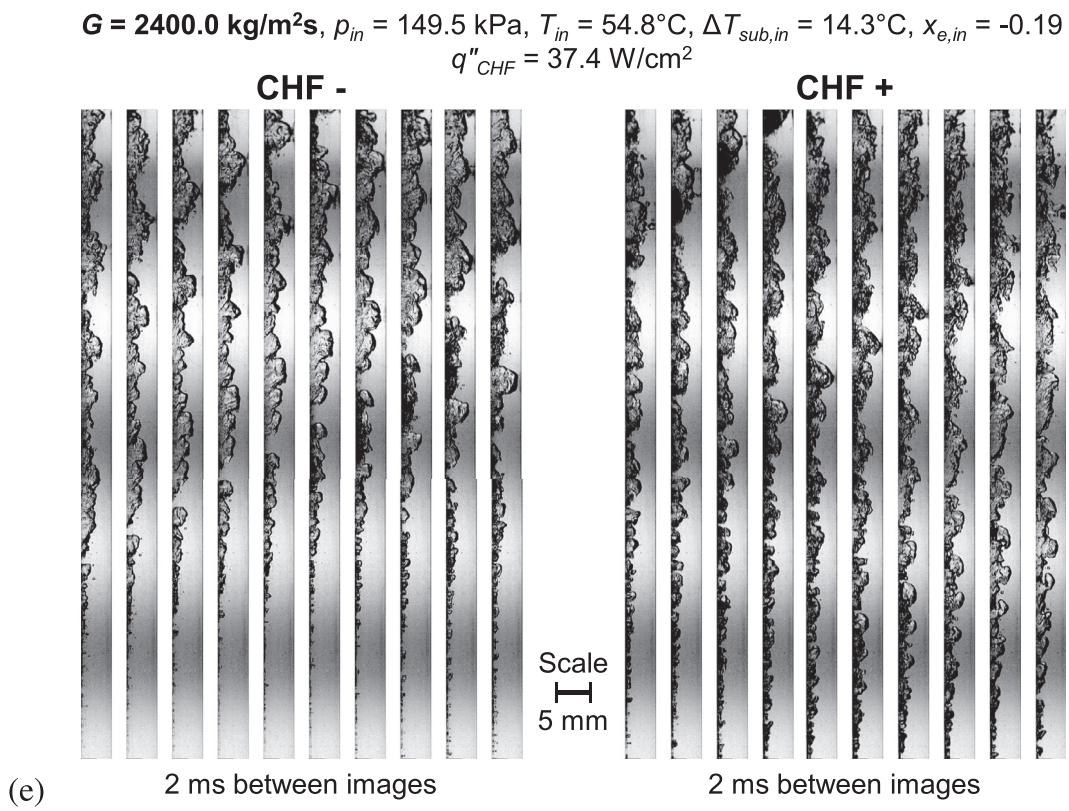

Fig. 12. Continued

wetting fronts to the upstream region of the channel, and q''_{CHF} is not enhanced. At $\Delta T_{sub,in}$ = 19.5°C, shown in Fig. 14(d), the liquid core is present throughout the channel and the vapor layers do not merge until just before the exit. However, at CHF+, a thin vapor layer covers the wall downstream, and wetting fronts are not seen along the wall except in the upstream region preceding the formation of the vapor layer. In Fig. 14(e), $\Delta T_{sub,in}$ = 28.5°C, the vapor layers no longer merge and mix together in the channel leading up to CHF. The influence of inlet subcooling is now strong enough to thin the vapor layers and increase q''_{CHF}. Throughout the channel, the two vapor layers align in a gear-tooth-mesh-like fashion, where the crests of one vapor layer correspond to the troughs of the other. Similar to single-sided heating, at the highest subcooling of $\Delta T_{sub,in}$ = 40.1°C, Fig. 14(f), an abundance of wetting fronts are present even at CHF+. However, a thin layer of vapor does grow along the left wall, preventing sufficient heat dissipation in the downstream region.

3.2.2. Effects of mass velocity for double-sided heating

Fig. 15 presents image sequences for double-sided heating with a low inlet subcooling of $\Delta T_{sub,in}$ = 6.9 – 7.0°C, at different mass velocities. At lower mass velocities of G = 199.9 and 480.0 kg/m^{2}s, respectively shown in Figs. 15(a) and (b), vapor layers grow rapidly and thick, merging in the upstream region of the channel. However, q''_{CHF} is significantly higher in Fig. 15(b), 27.3 W/cm^2, as compared to 18.2 W/cm^2 in Fig. 15(a). At a higher mass velocity, formation of wetting fronts to rewet the wall is more rapid, and the heat flux required to vaporize the supplied liquid is greater, resulting in higher q''_{CHF}. Fig. 15(c) shows cases with an intermediate velocity, similar to Fig. 14(a), and results in comparable flow patterns and q''_{CHF}. Further increasing mass velocity to G = 1600.0 kg/m^{2}s, shown in Fig. 15(d), increases the number of wetting fronts at CHF- as compared to lower mass velocities. Additionally, the downstream portion of the channel appears darker as mass velocity is increased. This is caused by turbulent mixing of the remaining liquid in the channel into the growing vapor layers. To the contrary, at the lower mass velocities in Fig. 15(a) and (b), the downstream portion of the channel is mostly vapor, visually light colored, and periodic waves of liquid-abundant dark regions pass through the channel. The highest mass velocity of G = 2400.0 kg/m^{2}s is presented in Fig. 15(e) and features the highest q''_{CHF} in the present figure. At both CHF- and CHF+ the wavy vapor layers develop near the upstream edge of the channel and slide along the wall. The vapor layers continue to grow as boiling persists within wetting fronts until lift off occurs at CHF+ and a thin vapor layer blocks liquid from most of the wall.

Similar image sequences, but with a higher inlet subcooling of $\Delta T_{sub,in}$ = 28.0 – 33.3°C, are presented in Fig. 16. The lowest mass velocity of G = 199.9 kg/m^{2}s is shown in Fig. 16(a). In the upstream region of the channel, vapor is contained to the near-wall region, even at the lowest mass velocity. Bubbles that detach from the wall condense into the subcooled liquid core. After some distance downstream, the thermal boundary layer is able to grow and the near-wall liquid rises in temperature, near saturation. This is conducive for bubble growth, and the wavy vapor layer grows, overtaking the channel core. At CHF+, wetting fronts are extinguished within the wavy vapor layer region but wetting of the wall occurs in the highly subcooled region upstream. As seen in previous figures, increasing the mass velocity to G = 319.5 and 801.7 kg/m^{2}s, respectively shown in Figs. 16(b) and (c), results in accelerated wetting fronts being pushed further into the channel, yielding higher q''_{CHF}.

Further raising the mass velocity to G = 1599.7 kg/m^{2}s, shown in Fig. 16(d), the upstream portion of the channel is predominantly liquid, with a few bubbles forming along the heated wall but condensing before growing. Further downstream, once the thermal boundary layer grows, bubbles that form along the wall grow as they slide further downstream. Bubbles coalesce into larger vapor

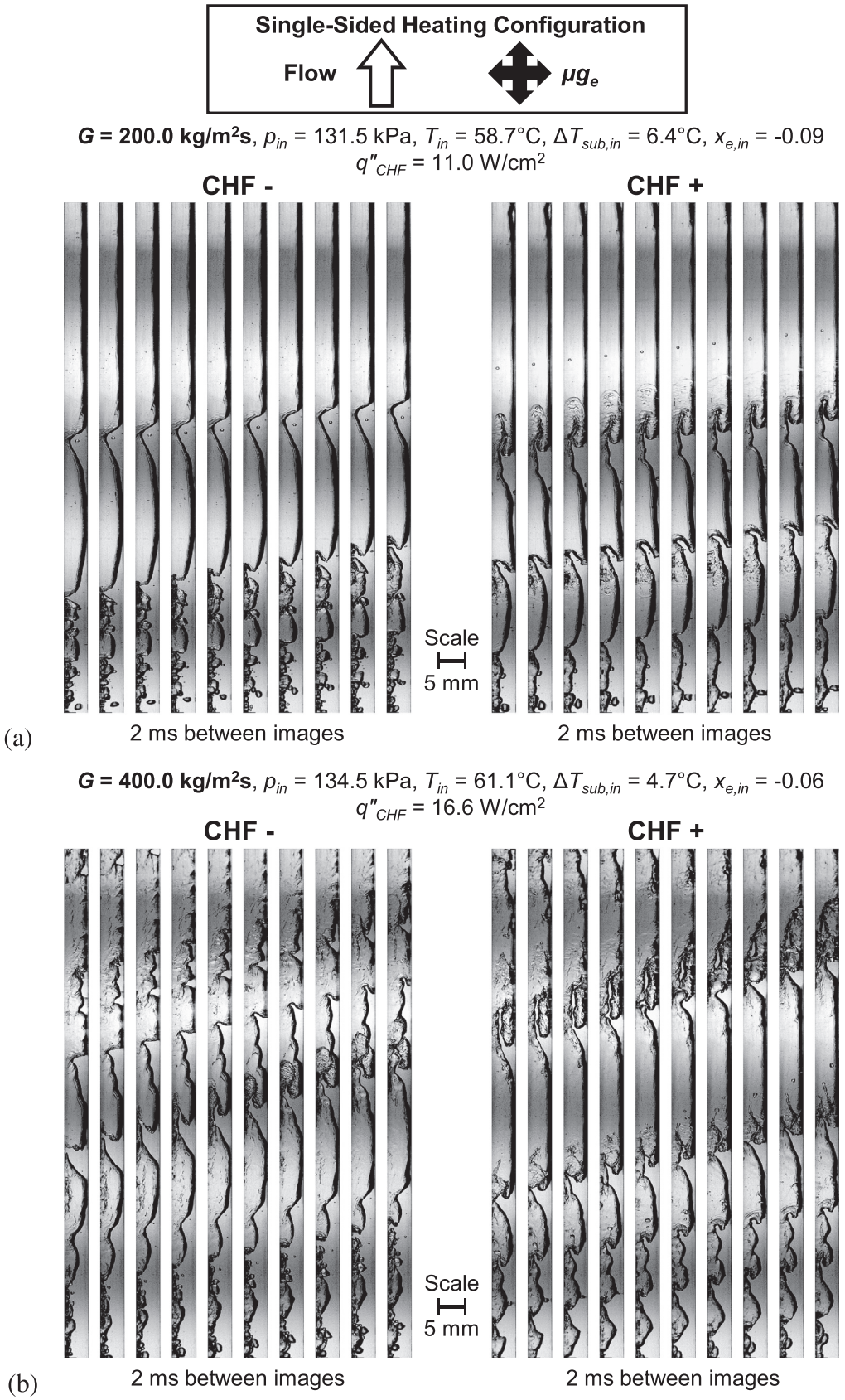

Fig. 13. Flow visualization image sequences around CHF for mass velocities G = (a) 200.0, (b) 400.0, (c) 800.0, (d) 1599.9, and (e) 2400.0 kg/m²s at fixed low inlet subcooling and low inlet pressure with single-sided heating. Time interval between successive images is mentioned below each sequence. Channel width is 5 mm.

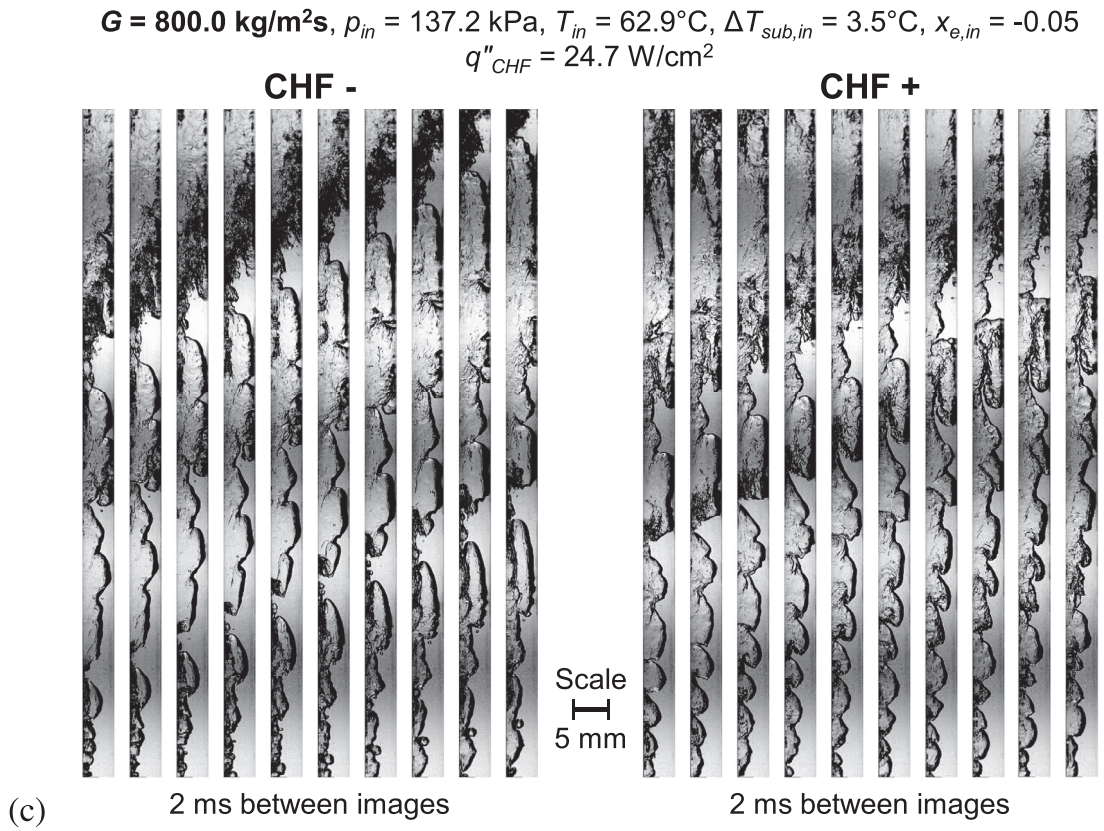

(c)

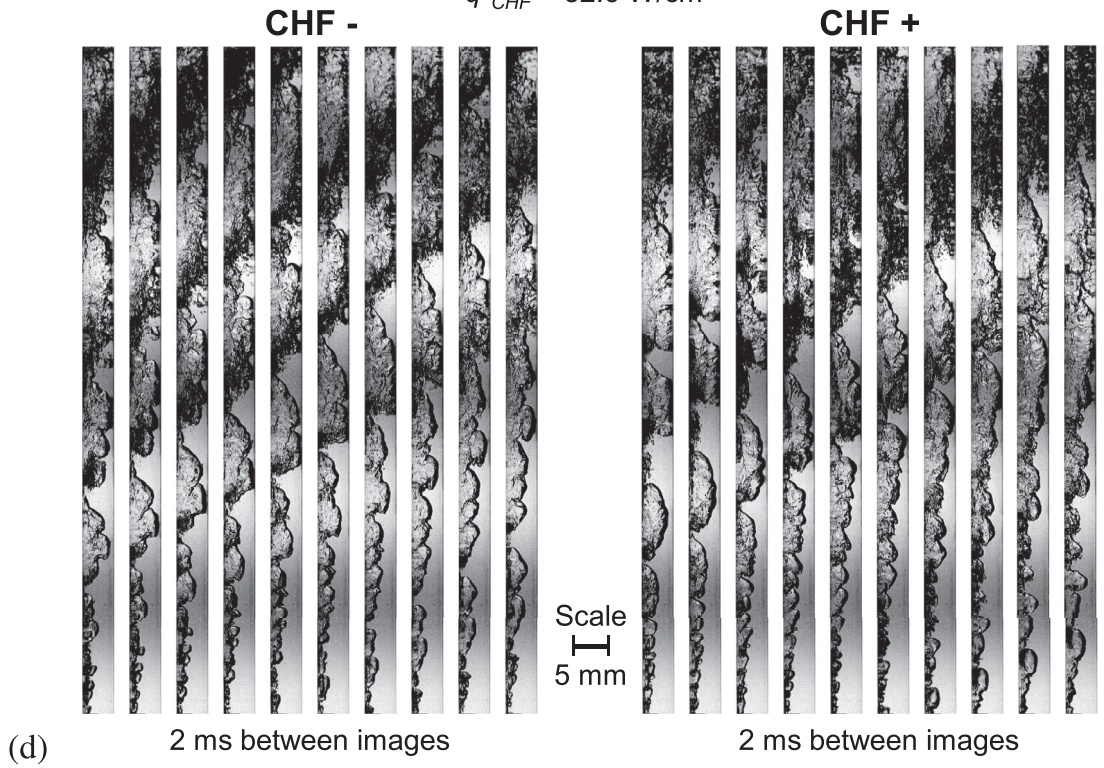

(d)

Fig. 13. Continued

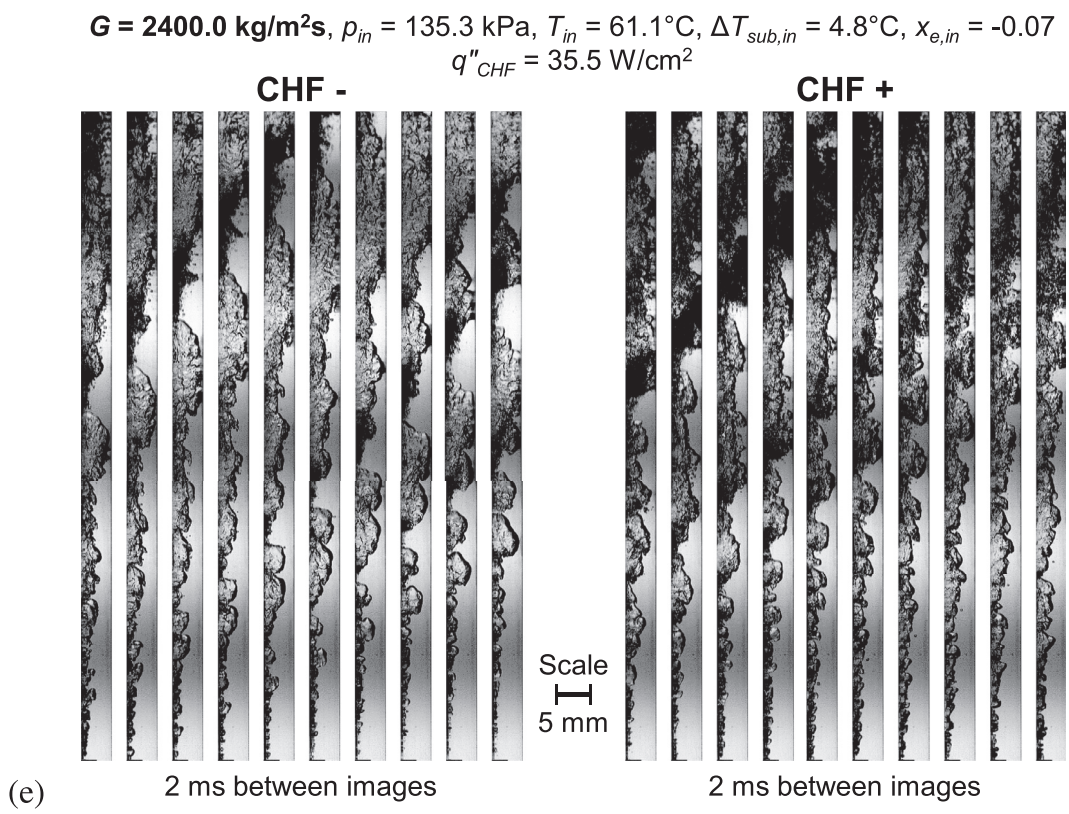

Fig. 13. Continued

structures that travel downstream as boiling continues within the wetting fronts between vapor patches. At CHF+, groups of wetting fronts lift off the wall, but localized cooling reaches downstream as periods of mostly subcooled liquid pass downstream, rewetting the wall. Regardless, cooling is insufficient to prevent the copper-strip thermocouples from reaching 122°C. At the highest mass velocity of $G = 2399.8$ kg/m^{2}s, shown in Fig. 16(e), even less vapor is present in the channel approaching CHF. The upstream region is occupied by highly subcooled liquid, and the vapor layer develops downstream. The combination of high mass velocity and high subcooling produces a thin vapor layer along each heated wall, as the strong influence of interfacial shear stresses and condensation at the liquid-vapor interface impede vapor growth.

3.3. Anomalous flow patterns

Certain operating conditions resulted in flow instabilities, which manifested as flow reversal at the outlet of the channel. Liquid that reentered the channel impeded or, in severe cases, destroyed the wavy vapor layer within the channel, complicating the flow patterns leading up to CHF. However, even during these transients, periods primarily featuring the wavy vapor layer regime exist. Severe instabilities were generally constrained to high inlet subcoolings and low flow rates. The current subsection discusses sequential images during the final heating increment culminating in CHF, which experienced flow instabilities. Time steps between consecutive images in each subfigure are larger than in previous figures in order to capture entire cycles of instability when possible. The images are numbered at the bottom of each sequence to enable easy cross-referencing.

Fig. 17(a) presents images with 7-ms spacing featuring double-sided heating, an intermediate mass velocity of $G = 801.7$ kg/m^{2}s, and a high subcooling of $\Delta T_{sub,in} = 28.5$°C. Images 1 and 2 show typical flow patterns observed in previous subsections. Then a period of flow reversal occurs where liquid renters the channel from the outlet and vapor structures are destroyed in the downstream section of the channel. This continues until about image 7, where flow inertia from the inlet eventually overcomes the reversed flow, standard flow pattern resumes, and the wavy vapor layer redevelops. Towards the end of the image sequence, in image 34, flow reversal from the outlet occurs again and the cycle repeats.

An image sequence with 7 ms between images and similar operating conditions to Fig. 17(a), $G = 803.1$ kg/m^{2}s, and $\Delta T_{sub,in} = 28.9$°C, but with a single heated wall is shown in Fig. 17(b). Flow instabilities are noticeably more severe for single-sided heating. At the beginning of the sequence, in image 1, a wavy vapor layer is observed sliding along the heated wall. In image 10, flow reversal begins and liquid flushes through the entire channel from the outlet, destroying the established vapor structures. In image 16, forward flow resumes, and the wavy vapor layer is briefly reestablished until flow reversal once again begins in image 33, clearing the channel. The severity of instability at CHF decreases with increasing mass velocity and decreasing inlet subcooling.

Fig. 17(c) shows an image sequence with a higher mass velocity of $G = 1599.9$ kg/m^{2}s, which requires a smaller time step of 3 ms to track flow transients. At an elevated mass velocity, flow reversal was unable to propagate through the entire channel and was constrained to the downstream section of the channel, unlike Fig. 17(b), where flow reversal affected the entire channel. Fig. 17(d) depicts an image sequence with a lower subcooling of $\Delta T_{sub,in} = 14.9$°C with 11 ms between images. Even at a lower mass velocity of $G = 403.9$ kg/m^{2}s, flow reversal is less severe than at higher subcooling, and the wavy vapor layer in the upstream portion of the channel continues to grow and travel downstream.

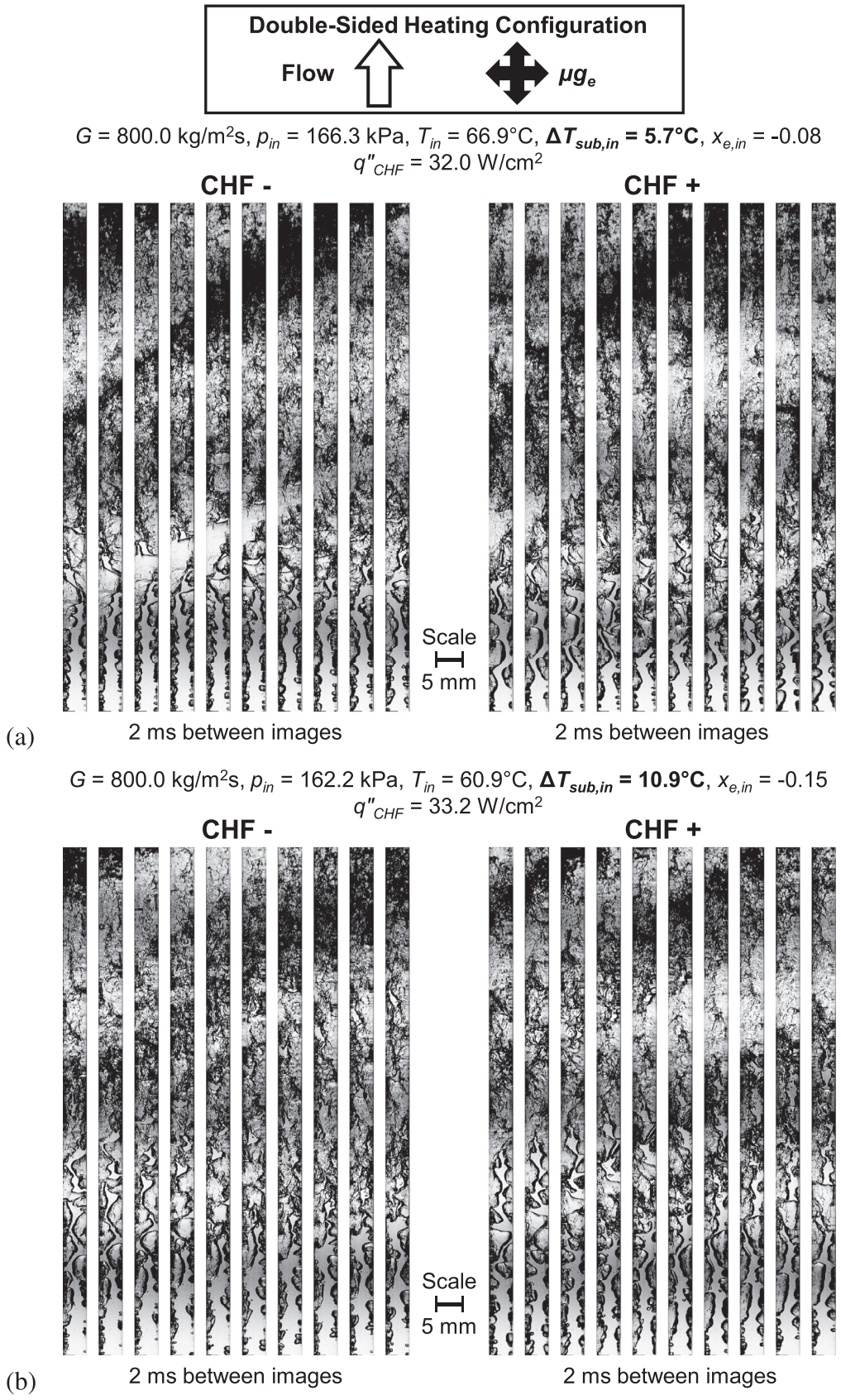

Fig. 14. Flow visualization image sequences around CHF for inlet subcoolings of $\Delta T_{sub,in}$ = (a) 5.7°C, (b) 10.9°C, (c) 13.6°C, (d) 19.5°C, (e) 28.5°C, and (f) 40.1°C at fixed moderate mass velocity and high inlet pressure with double-sided heating. Time interval between successive images is mentioned below each sequence. Channel width is 5 mm.

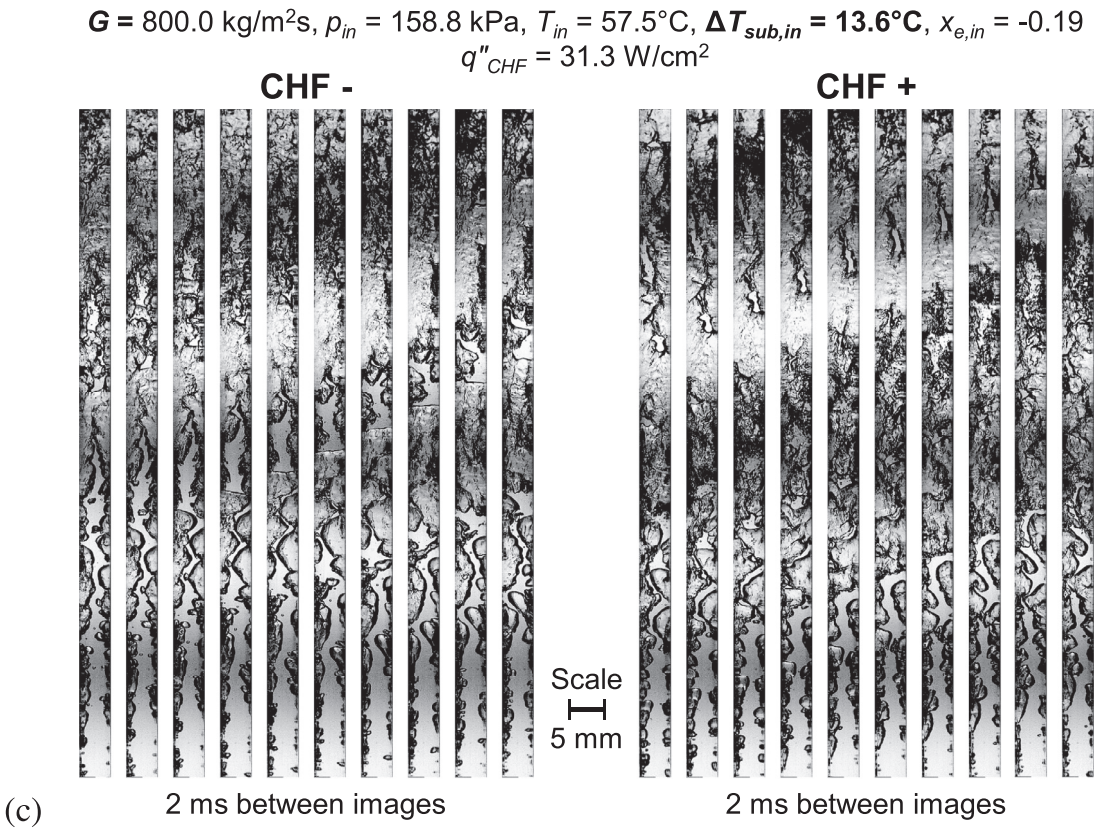

(c)

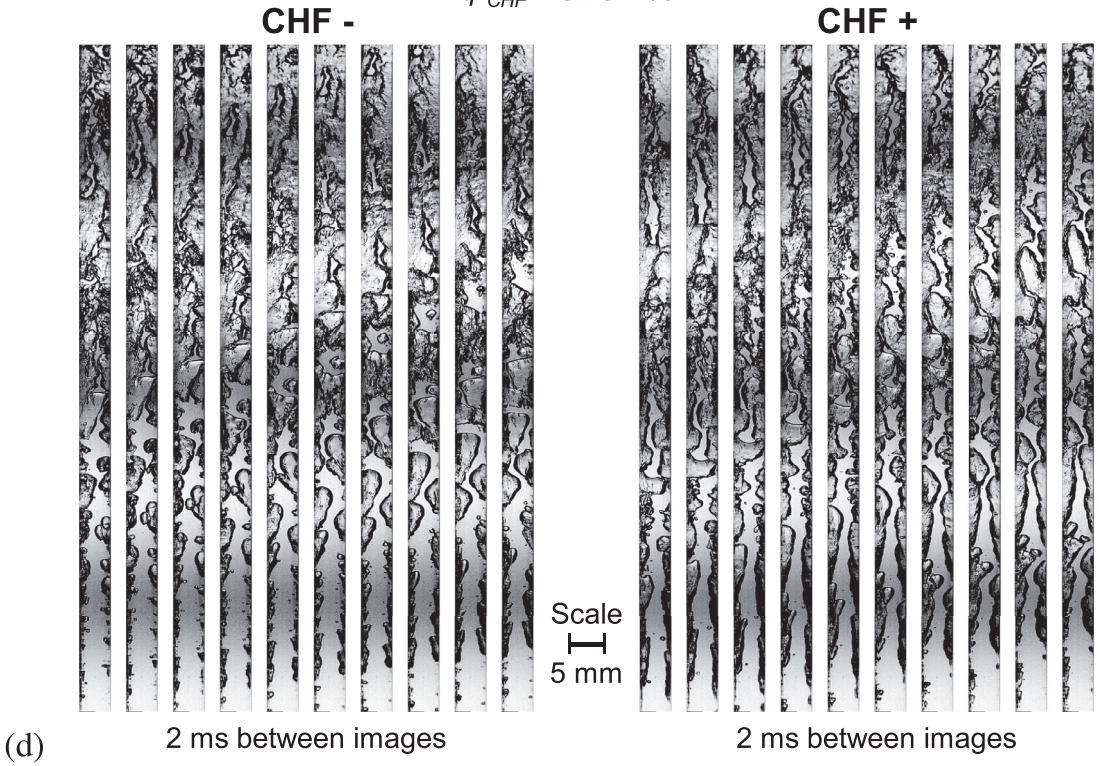

(d)

Fig. 14. Continued

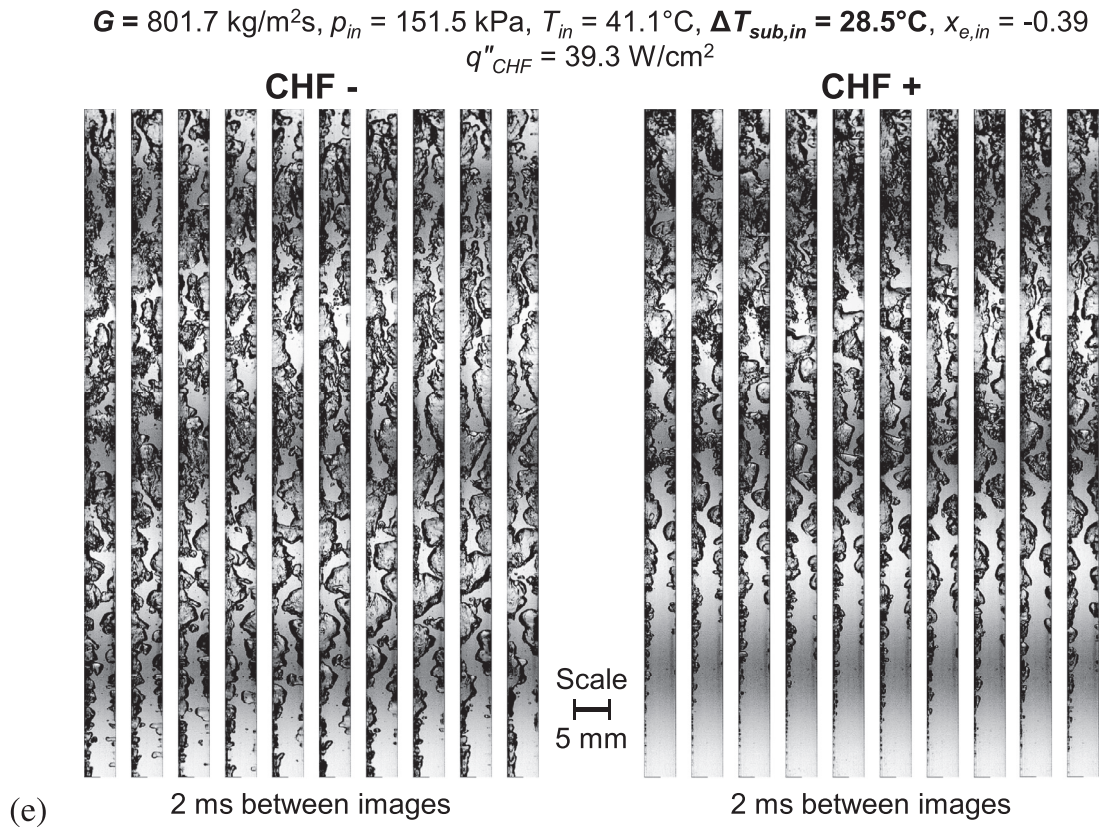

(e)

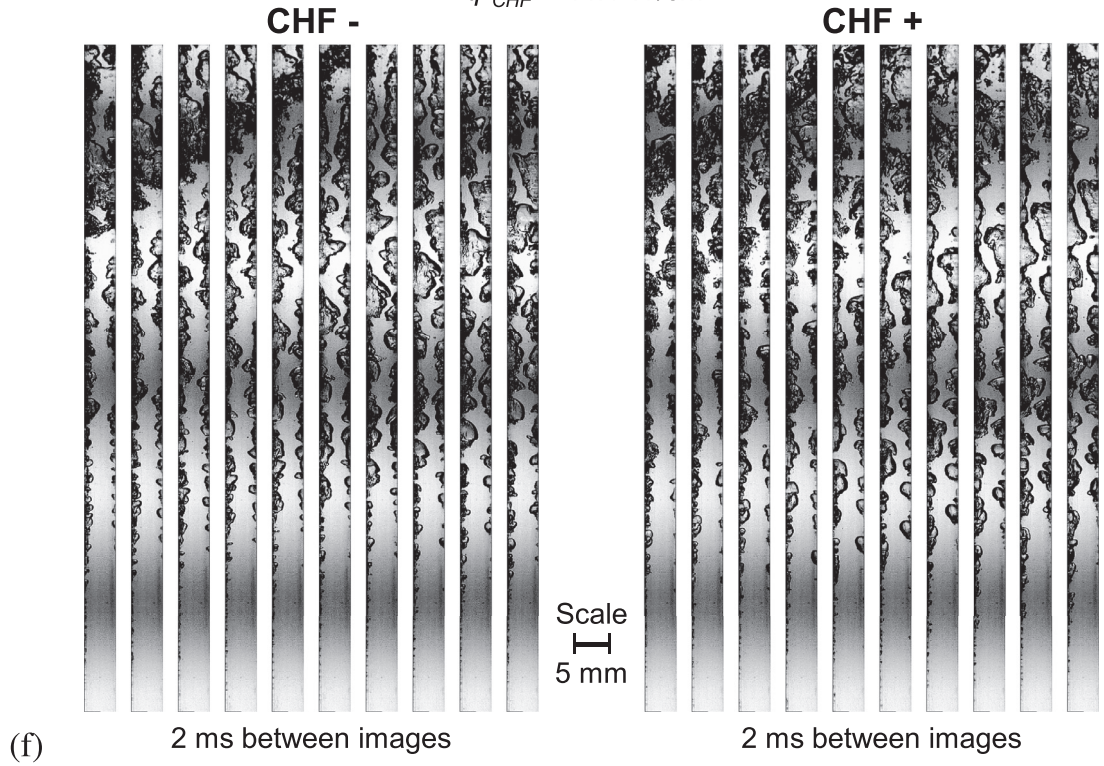

(f)

Fig. 14. Continued

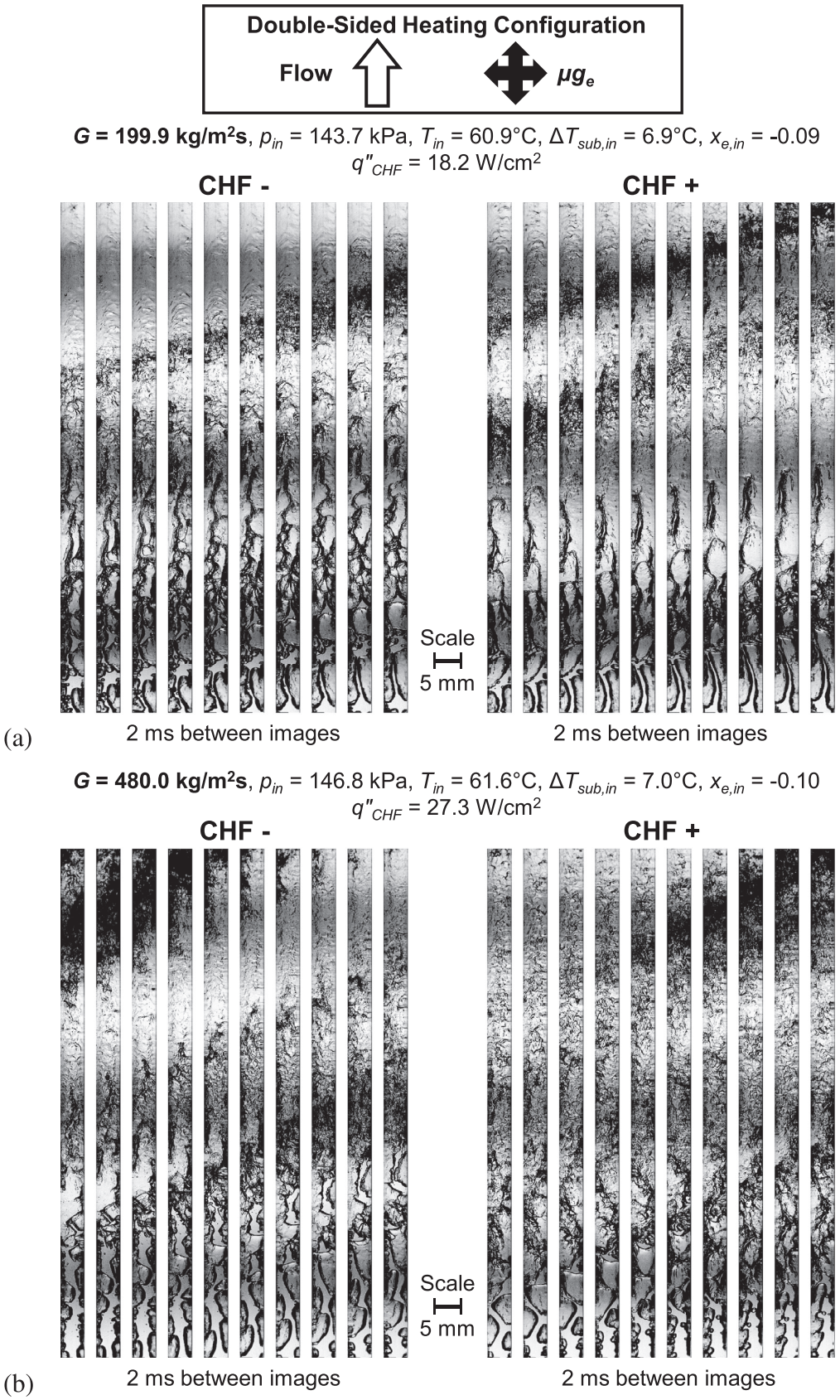

Fig. 15. Flow visualization image sequences around CHF for mass velocities G = (a) 199.9, (b) 480.0, (c) 800.0, (d) 1600.0, and (e) 2400.0 kg/m2s at fixed low inlet subcooling and high inlet pressure with double-sided heating. Time interval between successive images is mentioned below each sequence. Channel width is 5 mm.

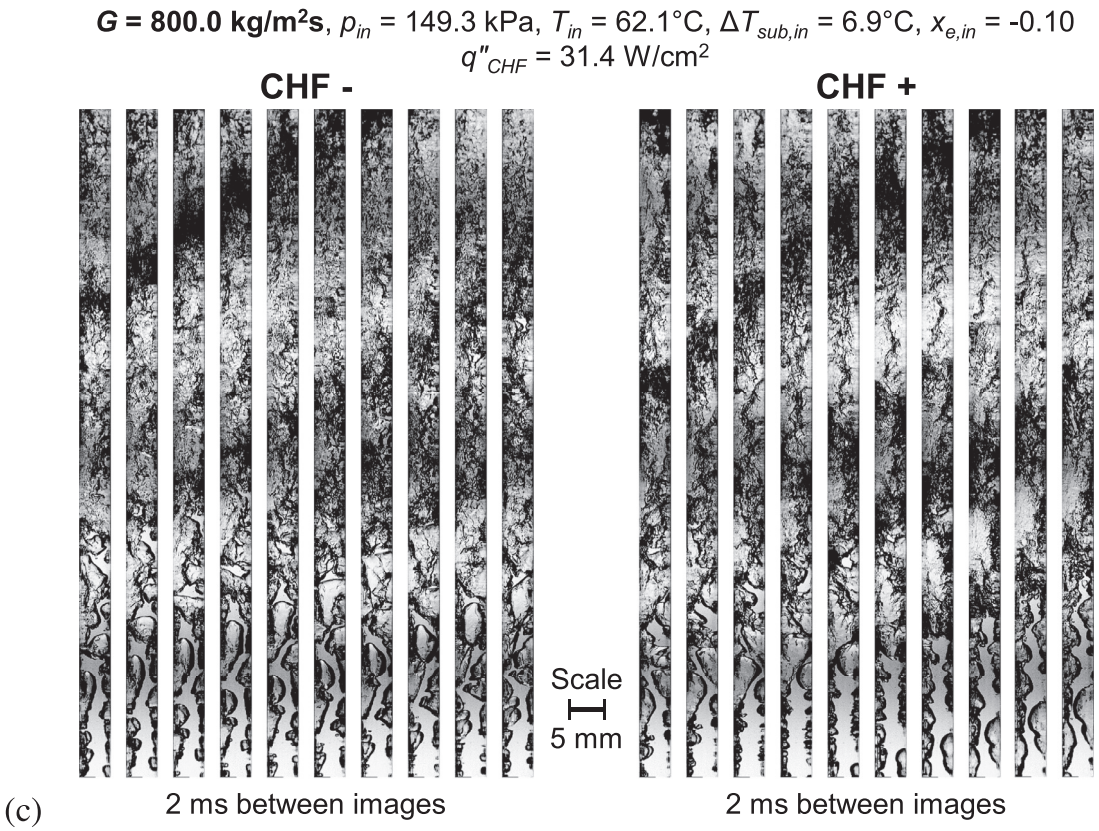

(c)

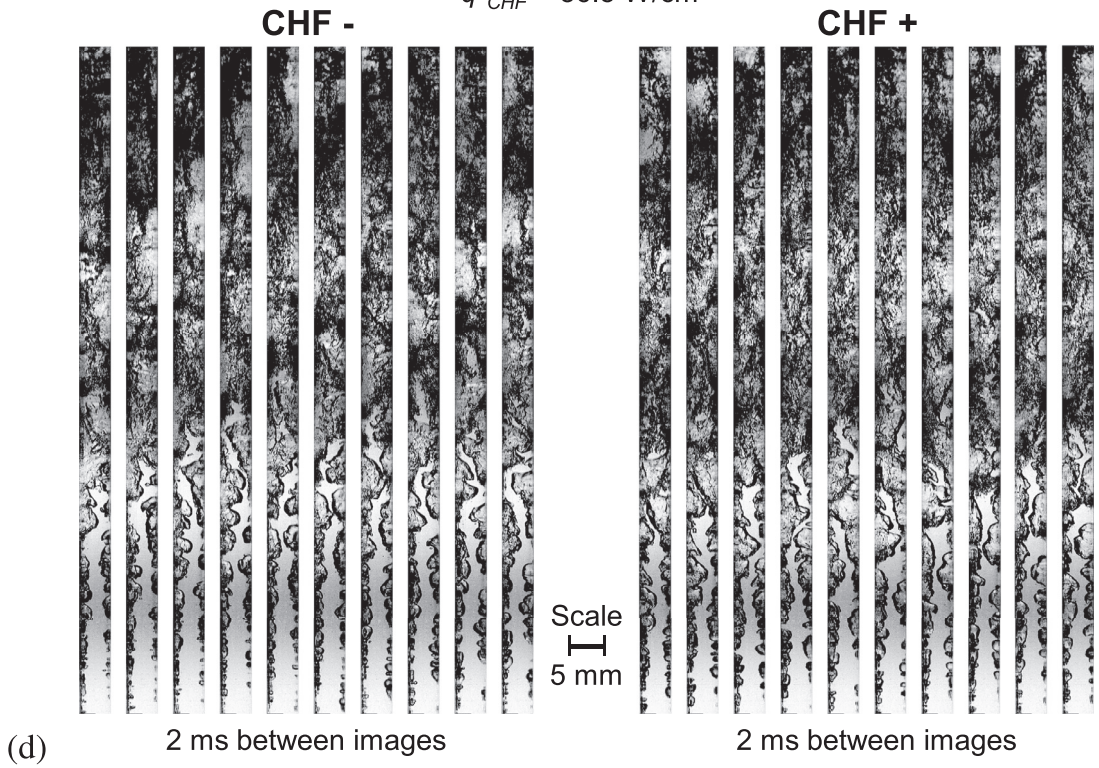

(d)

Fig. 15. Continued

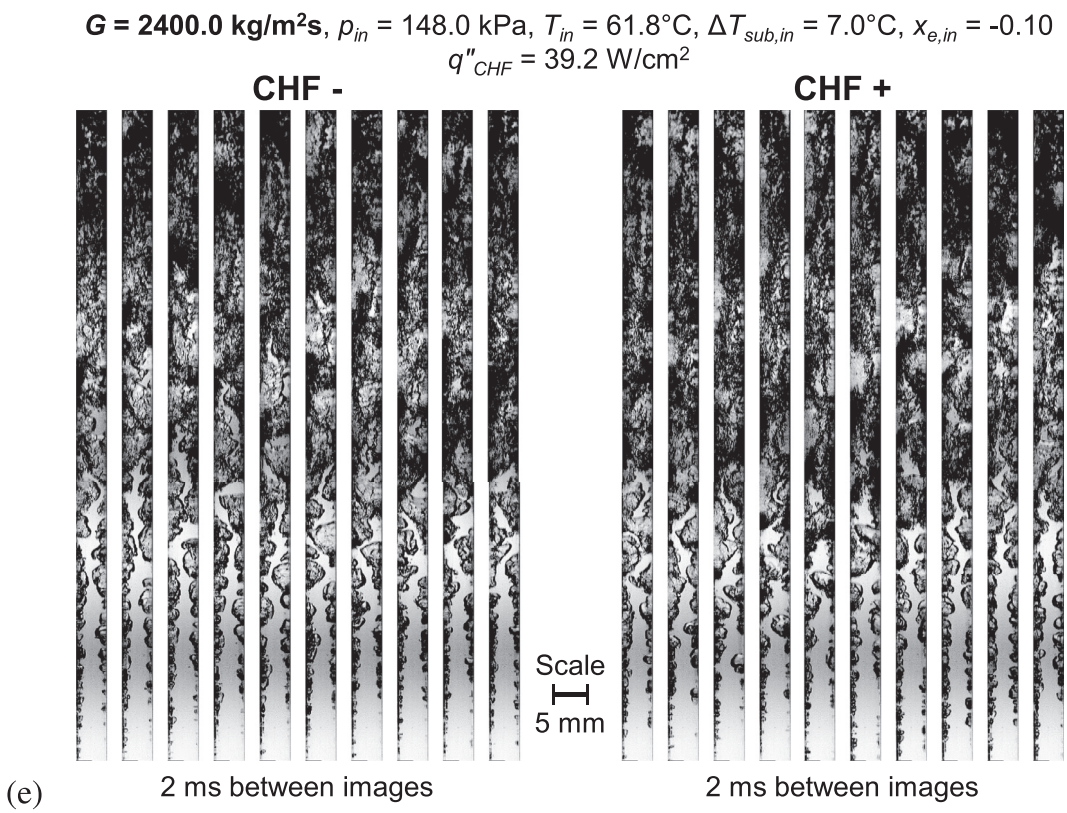

Fig. 15. Continued

4. CHF results and discussion

4.1. Parametric effects of inlet pressure, mass velocity, and inlet subcooling

Fig. 18 shows experimental q''_{CHF} versus G for different ranges of inlet subcooling. At the beginning of each run, inlet pressure was set to either 130.0 kPa (18.85 psia) or 151.7 kPa (22 psia); note for the latter pressure, 160.0 kPa (23.2 psia) was initially used as the set point, but the system could not consistently achieve this inlet pressure, so the set point was lowered for the remaining cases. However, maintaining a relatively constant mass flow rate along the boiling curve resulted in pressure drop to increase with increasing heat flux, which in turn caused inlet pressure to increase along the boiling curve. To best segregate the two p_{in} ranges, data at CHF is demarcated into two groups by p_{in} = 140 kPa for single-sided heating, and p_{in} = 150 kPa for double-sided heating in Figs. 18(a) and (b), respectively. Compared to mass velocity and inlet subcooling, inlet pressure variation for the present operating conditions has a mild influence on q''_{CHF}, typically within the uncertainty in q''_{CHF}. For this reason, subsequent plots will not differentiate inlet pressure ranges and will focus on more influential trends.

Figs. 18(c) and (d) show the overall plots of q''_{CHF} versus G for single- and double-sided heating, respectively. For each subcooling range, q''_{CHF} increases at a decaying rate with G for both single- and double-sided heating at all inlet subcooling ranges. At low G, double-sided heating exhibits greater q''_{CHF} than single-sided heating, specifically at lower inlet subcooling. This is due to vapor production along both heated walls resulting in greater flow acceleration, accentuating the influence of inertia. However, at high inlet subcooling, single-sided heating results in higher q''_{CHF} at relatively low G. During double-sided heating, heat gained from both walls accelerates the rise of the bulk fluid temperature along the length of the channel, diminishing the benefits achieved at high inlet subcooling. At high G, flow inertia becomes the dominant parameter and q''_{CHF} converges for both single- and double-sided heating. For both single- and double-sided heating, subcooling has a weak influence on q''_{CHF} at relatively low subcoolings, and curves for the majority of inlet subcooling ranges overlap.

The effect of subcooling is further explored in Figs. 19(a) and 19(b) which show q''_{CHF} versus $\Delta T_{sub,in}$ for different mass velocity ranges with single- and double-sided heating, respectively. For all mass velocity ranges, q''_{CHF} does not initially vary with inlet subcooling, with some perturbations within uncertainty. In this region, the bulk fluid temperature is close enough to saturation that non-equilibrium effects caused by condensation are weak and do not significantly impede vapor production, as seen in Figs. 10 and 14. Once inlet subcooling exceeds ~15°C, q''_{CHF} increases at a near linear rate with inlet subcooling. q''_{CHF} increases at a faster rate with respect to inlet subcooling for single-sided heating, where the bulk fluid better retains its subcooling throughout the channel. For single-sided heating, the highest inlet subcooling was achieved for G = 799.9 – 805.1 kg/m^{2}s and it resulted in constant q''_{CHF} at high inlet subcooling. Maximum subcooling was limited by flow instabilities at lower mass velocities, while at high mass velocities, it was limited by the maximum heater power practically not reaching CHF. However, at G = 799.9 – 805.1 kg/m^{2}s, where wall substrate temperatures were able to reach 122°C, temporal records reveal heater shut down was possibly triggered by a singular large temperature fluctuation, indicating the onset of more severe instabilities, at high subcooling. Fig. 7 showed temporal records of wall substrate temperatures and heater power for a typical case, free of any instabilities. Clearly CHF is reached indicated by the inflection point in substrate temperatures as they rapidly escalate to 122°C. Fig. 20(a) show temporal records of wall substrate temperatures and heater power for a case with $\Delta T_{sub,in}$ = 29.8°C, just before the high-subcooling region where q''_{CHF} is insensitive to further in-

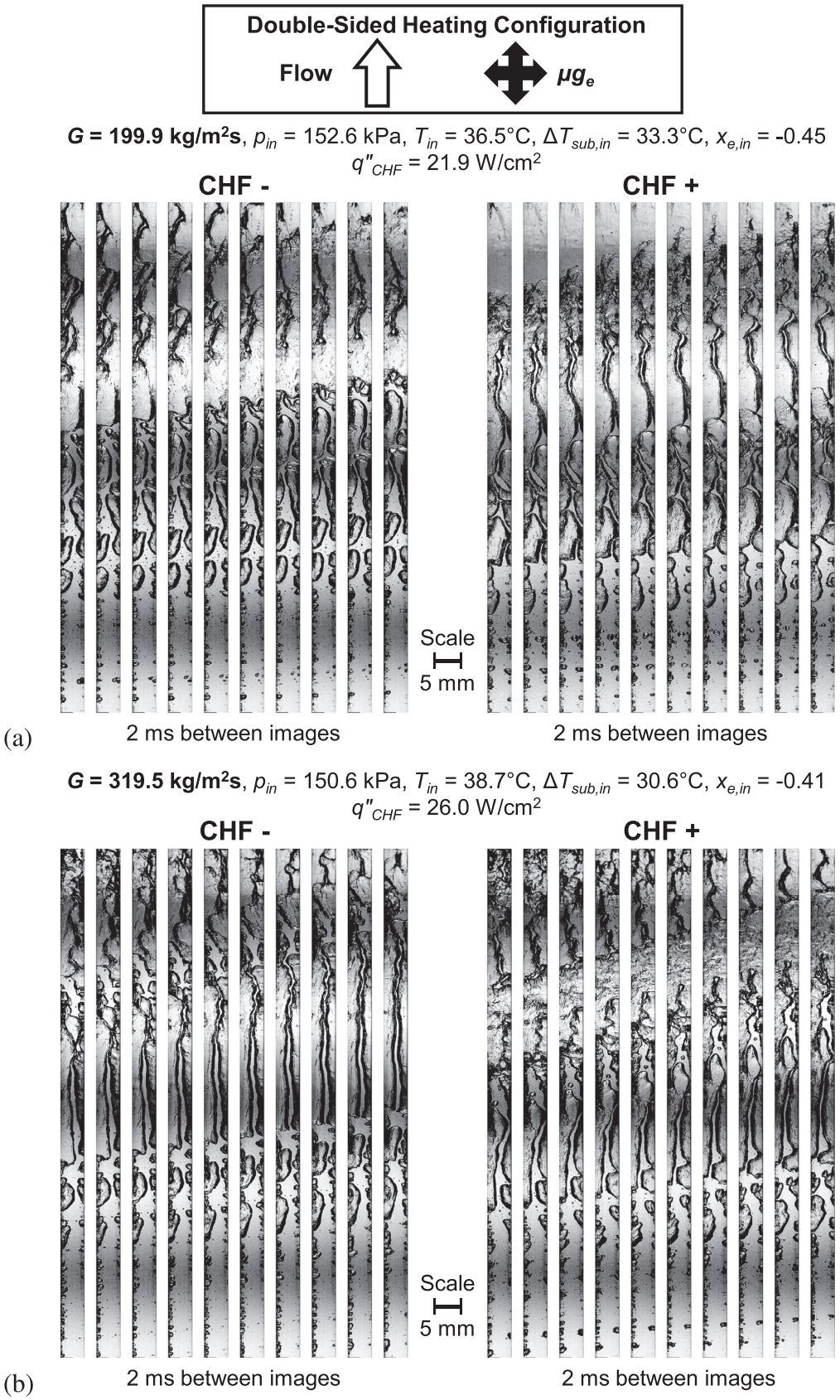

Fig. 16. Flow visualization image sequences around CHF for mass velocities G = (a) 199.9, (b) 319.5, (c) 801.7, (d) 1599.7, and (e) 2399.8 kg/m²s at fixed high inlet subcooling and high inlet pressure with double-sided heating. Time interval between successive images is mentioned below each sequence. Channel width is 5 mm.

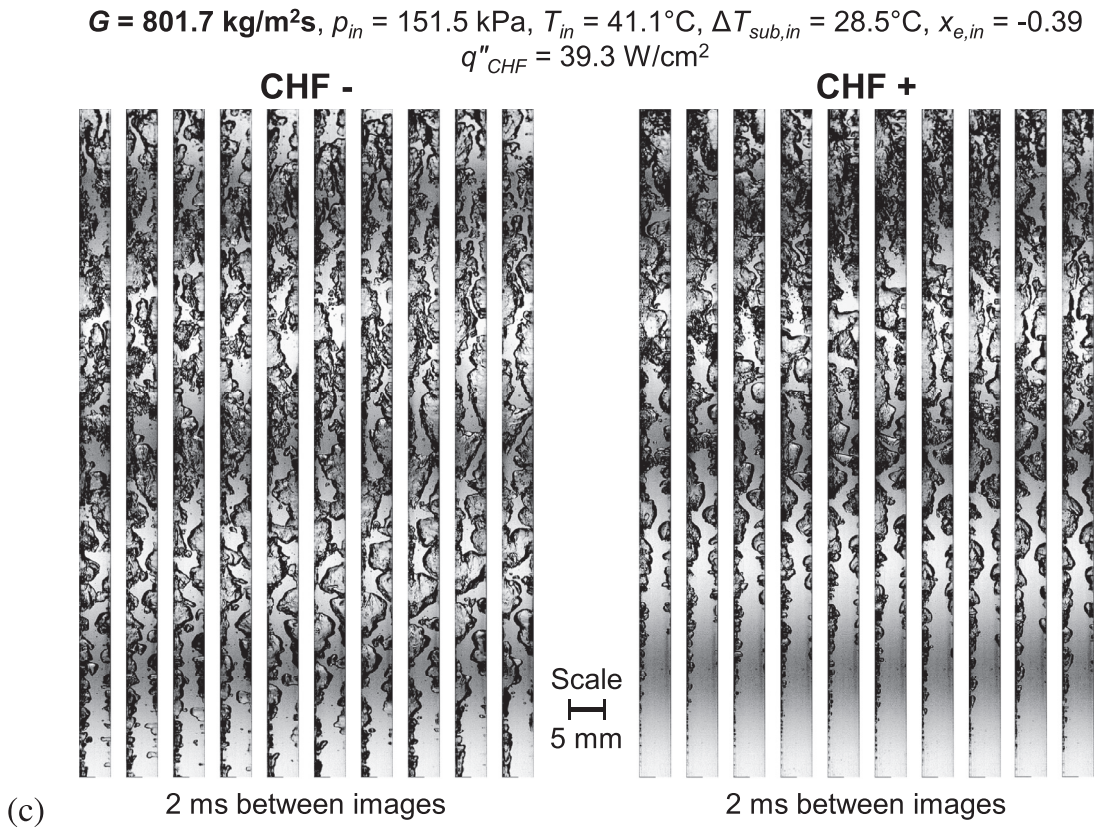

(c)

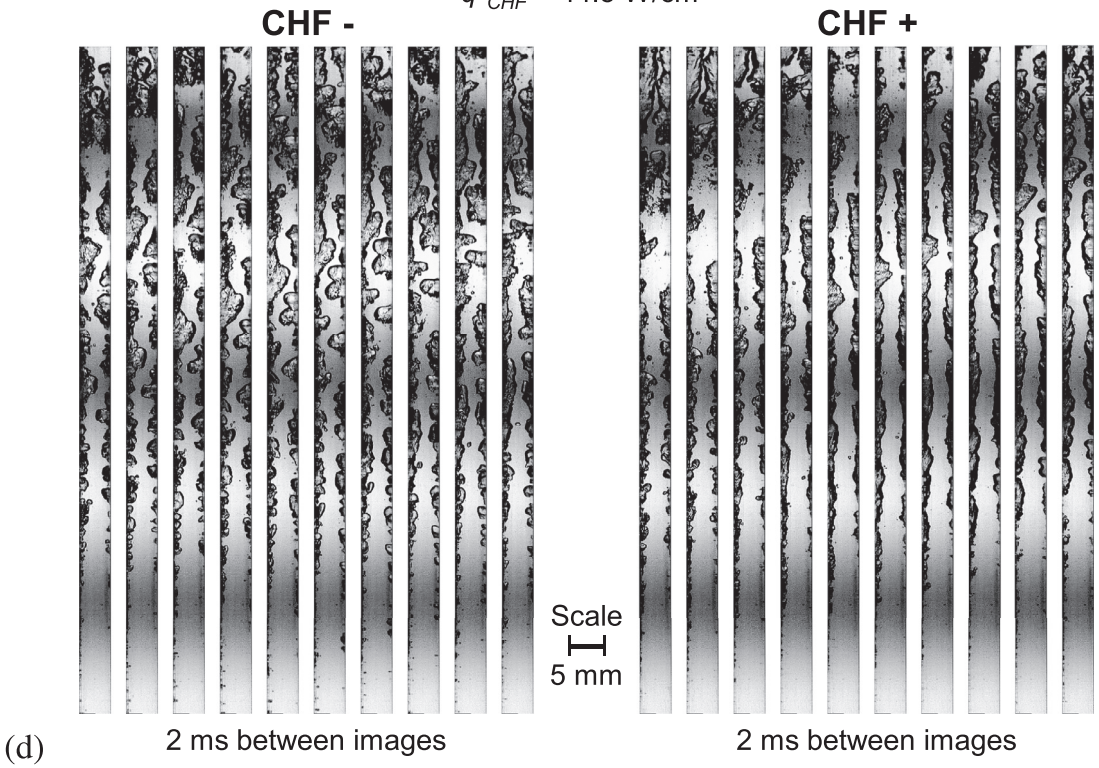

(d)

Fig. 16. Continued

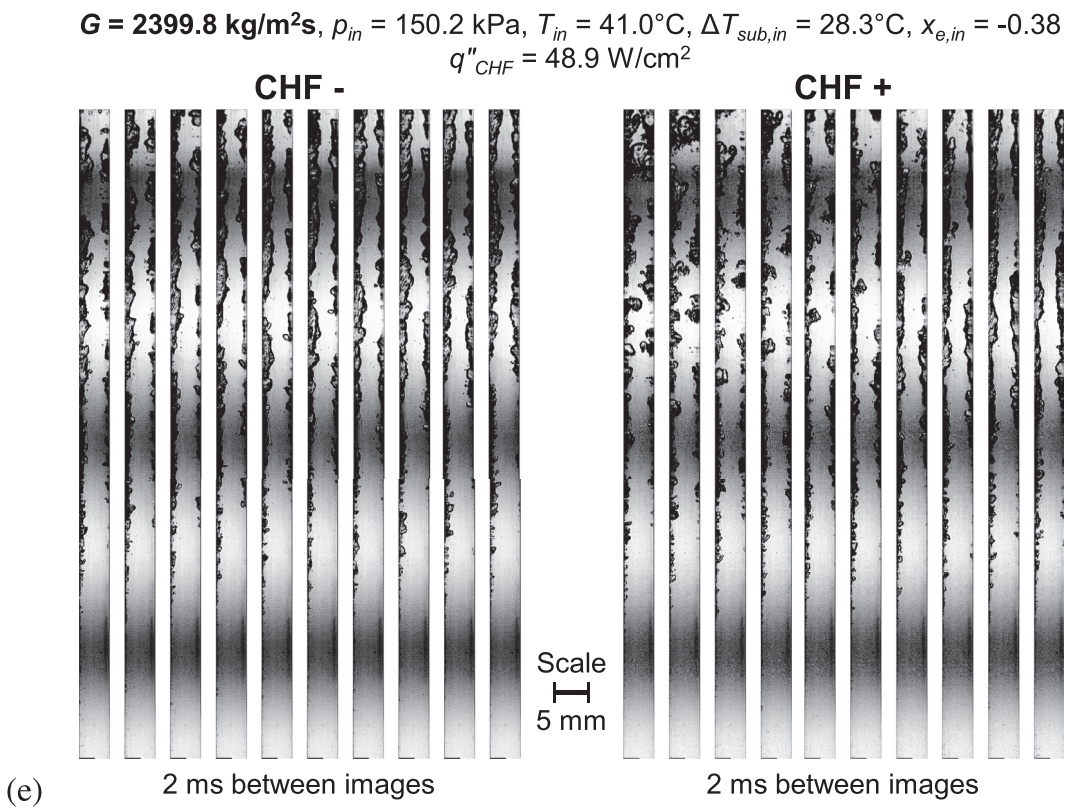

Fig. 16. Continued

creases in $\Delta T_{sub,in}$. The last heater power increment caused a sudden, concave up, rise in wall temperature triggering CHF. Wall temperatures were relatively steady before this point, unlike Fig. 20(b), which features a case within the insensitive region and an inlet subcooling of $\Delta T_{sub,in} = 39.3°C$. Prior to CHF, comparatively severe temporal fluctuations, continually peak near 122°C. These fluctuations could produce similar $q"_{CHF}$ anywhere in this region. Double-sided heating did not experience as severe instabilities as single-sided heating, and $q"_{CHF}$ continually increased with inlet subcooling after the insensitive region observed at low inlet subcooling. Interestingly, the operating conditions exhibiting temperature fluctuations are similar to those which produced periodic flow patterns, as discussed in Fig. 17, high subcooling and exacerbated during single-sided heating and at low flow rates. Detailed analysis of the transient characteristics during these cases is outside the scope of the present study but may be explored in the future. However, severe temperature fluctuations leading up to CHF appear to be correlated to flow instabilities.

4.2. Dimensionless group relationships

Figs. 21(a) and (b) show plots of $q"_{CHF}$ versus $x_{e,out}$, which link mass flow rate, inlet subcooling, and heat flux, for single- and double-sided heating, respectively. All datapoints are segregated into different mass velocity ranges. For both heating configurations, $q"_{CHF}$ increases with decreasing $x_{e,out}$. Larger $q"_{CHF}$ at large negative outlet qualities is attributed to non-equilibrium effects promoting condensation at the interface and delayed thermal boundary layer development, thinning the vapor layer. $q"_{CHF}$ decreases as $x_{e,out}$ increases until a certain value, approaching the transition to saturated CHF, $x_{e,out} \geq 0$, where $q"_{CHF}$ becomes insensitive to $x_{e,out}$. The threshold of insensitivity moves towards lower outlet qualities as mass velocity increases. For double-sided heating, shown in Fig. 21(b), $q"_{CHF}$ decreases with increasing $x_{e,out}$ well into saturated CHF at low mass velocities.

The same datapoints are reorganized by inlet subcooling in Figs. 21(c) and (d), which show $q"_{CHF}$ versus $x_{e,out}$ at different inlet subcooling ranges for single- and double-sided heating, respectively. The saturated CHF cases in Fig. 21(b) showing strong sensitivity to $x_{e,out}$ correspond to cases with high inlet subcooling in Fig. 21(d), where regardless of the outlet being saturated, high inlet subcooling enhances $q"_{CHF}$, as shown in Fig. 19.

Non-dimensionalizing the vertical axis from $q"_{CHF}$ to Bo, Figs. 22(a) and (b) show Bo versus $x_{e,out}$ for single- and double-sided heating, respectively. Drawn on each plot are lines of constant $x_{e,in}$ assuming constant pressure. For both single- and double-sided heating, clear segregations are observed for different mass velocity ranges. As expected from the definition of Bo, increasing mass velocity results in lower Bo values for a given $x_{e,out}$. Similar to the dimensional results of $q"_{CHF}$, as $x_{e,out}$ increases, Bo decreases more rapidly for single-sided heating than for double-sided heating, with higher mass velocities being less sensitive. For a given $x_{e,in}$, increasing $x_{e,out}$ results in a larger change in Bo for single-sided heating than double-sided. A larger Bo corresponds to a larger $q"_{CHF}$, which results in more heat added to the fluid for double-sided heating.

To isolate the influence of $q"_{CHF}$, the dimensionless term Bo^2We_D, which is a product of $q"_{CHF}$ and saturated fluid properties, is plotted against $x_{e,out}$. Eliminating the influence of mass velocity collapses the data onto a single, near-linear trend for each heating configuration as shown in Figs. 22(c) and (d), respectively. Bo^2We_D decreases as outlet quality increases, and mimics the trends observed in Fig. 21.

Similar dimensionless results are presented in Figs. 23(a) and (b), depicting Bo^2We_D versus Re_f, and Figs. 23(c) and (d), depicting Bo^2We_D versus $x_{e,in}$. Figs. 23(a) and (b) mirror the results of $q"_{CHF}$ versus G in Figs. 18(c) and (d) for single- and double-sided heat-

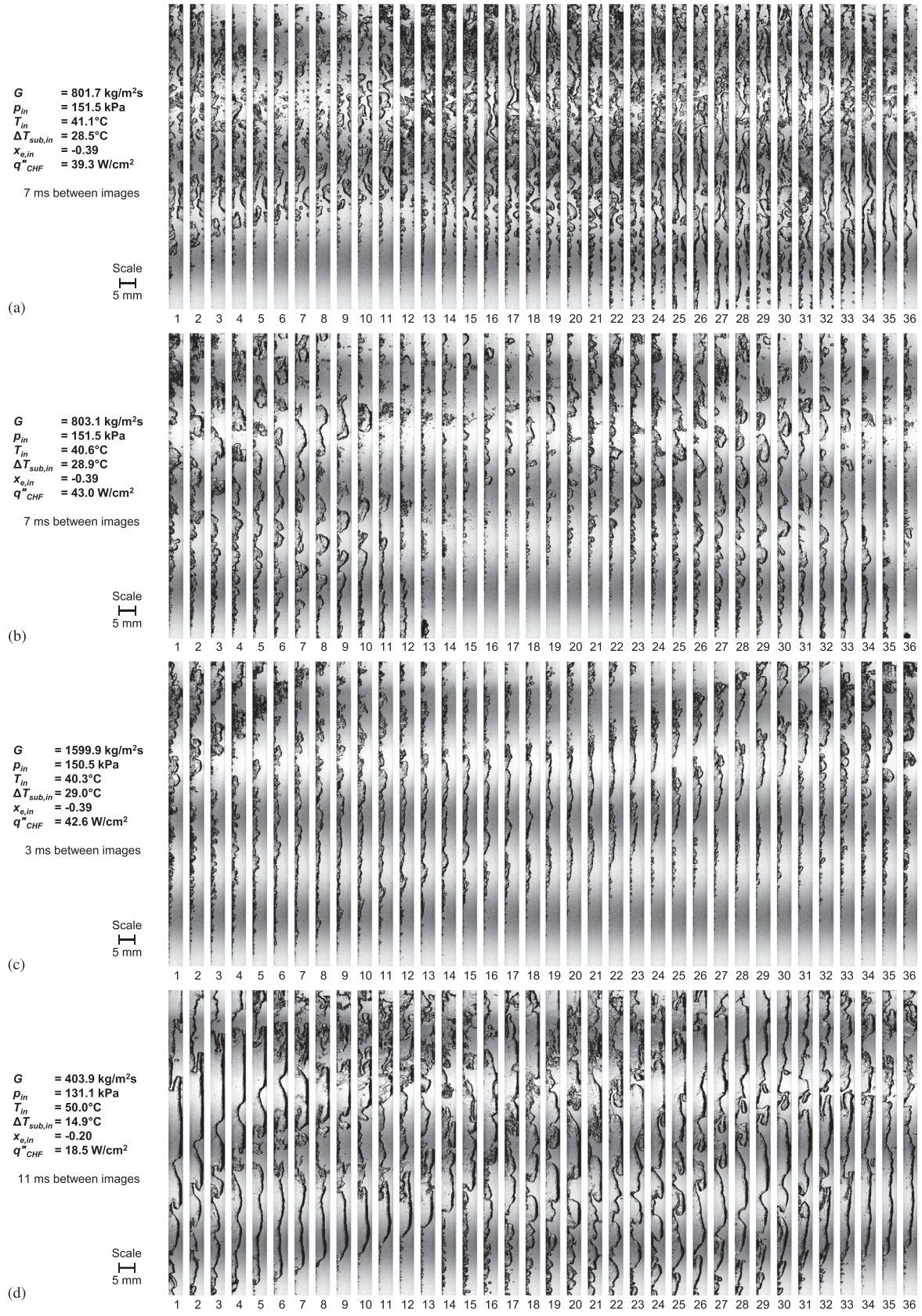

Fig. 17. Flow visualization image sequences at CHF for double-sided heating with (a) G = 801.7 kg/m^{2}s and $\Delta T_{sub,in}$ = 28.5°C, and single-sided heating with (b) G = 803.1 kg/m^{2}s and $\Delta T_{sub,in}$ = 28.9°C, (c) G = 1599.9 kg/m^{2}s and $\Delta T_{sub,in}$ = 29.0°C, and (d) G = 403.9 kg/m^{2}s and $\Delta T_{sub,in}$ = 14.9°C. Time interval between successive images is mentioned within each part. Channel width is 5 mm.

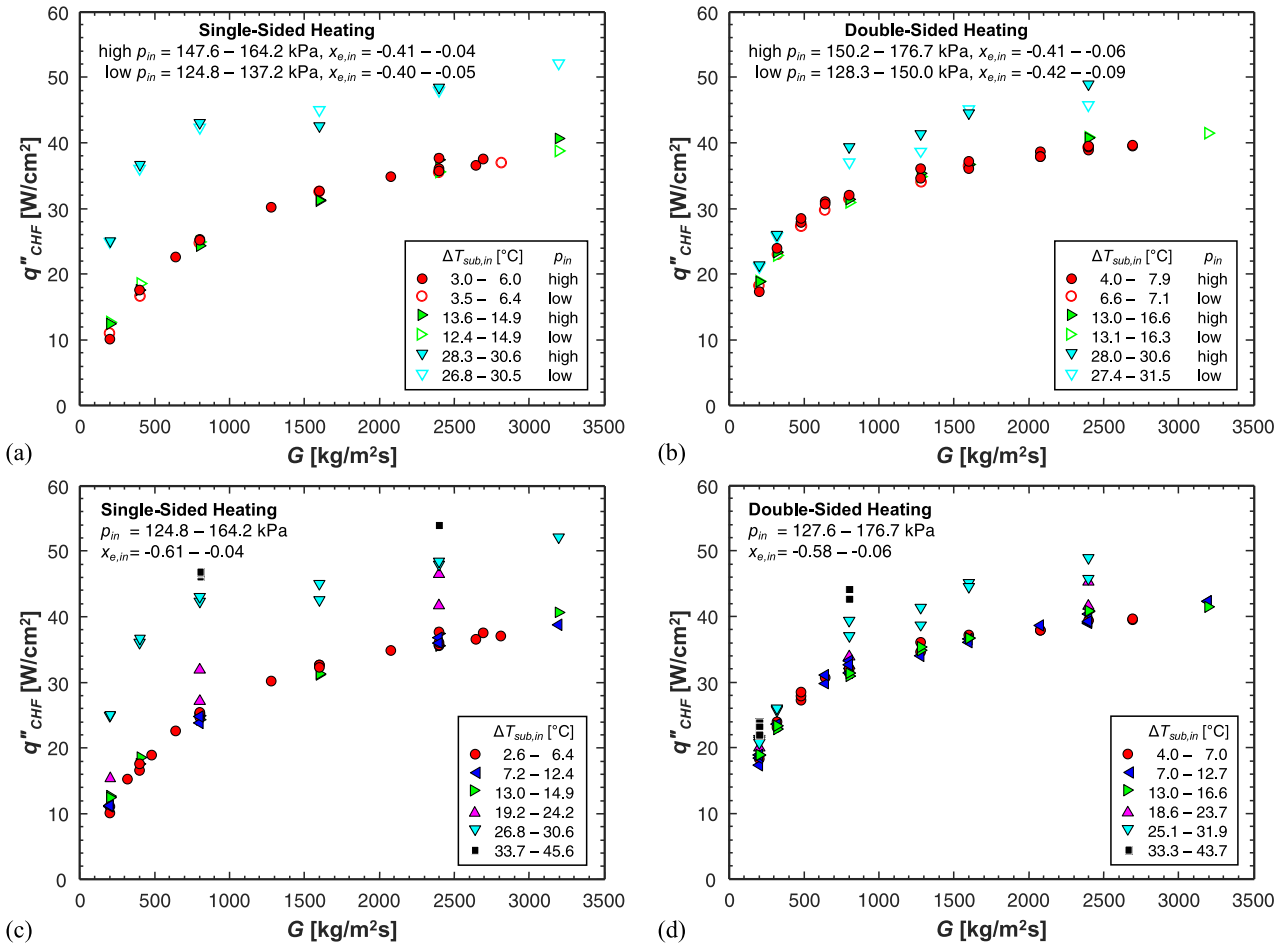

Fig. 18. Variations of experimental CHF results versus mass velocity highlighting different pressure ranges for a subset of the database with (a) single- and (b) double-sided heating, and for the entire database with (c) single- and (d) double-sided heating.

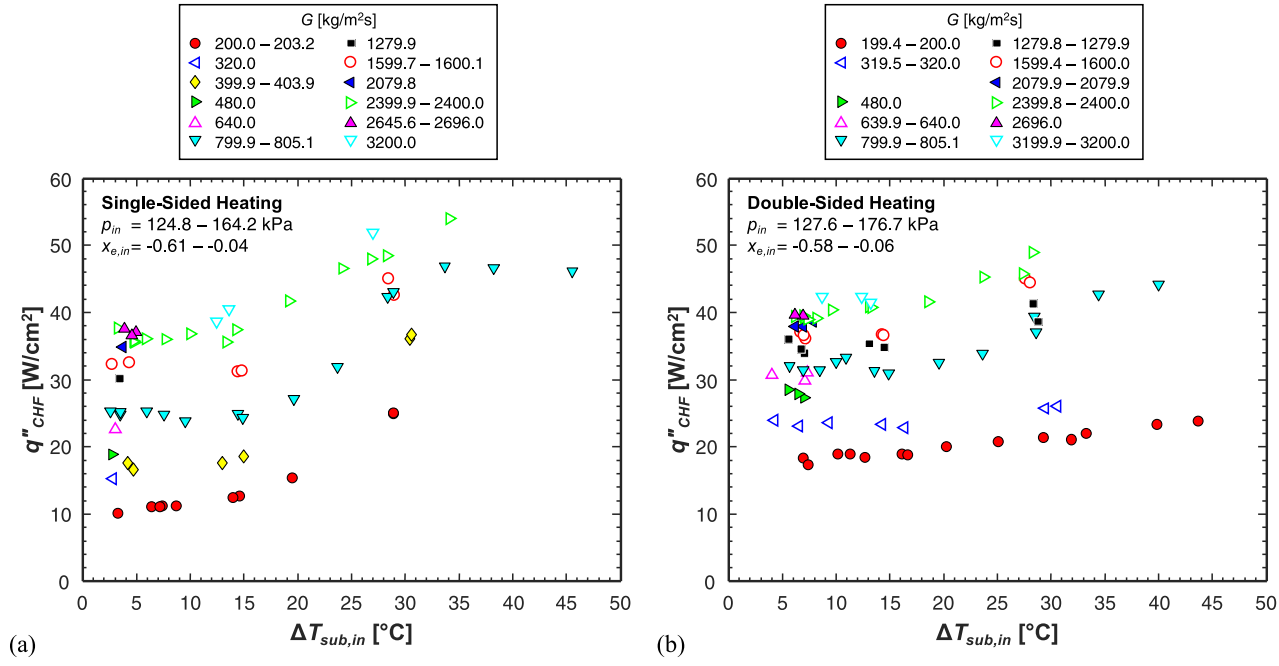

Fig. 19. Variations of experimental CHF results versus inlet subcooling for (a) single- and (b) double-sided heating.

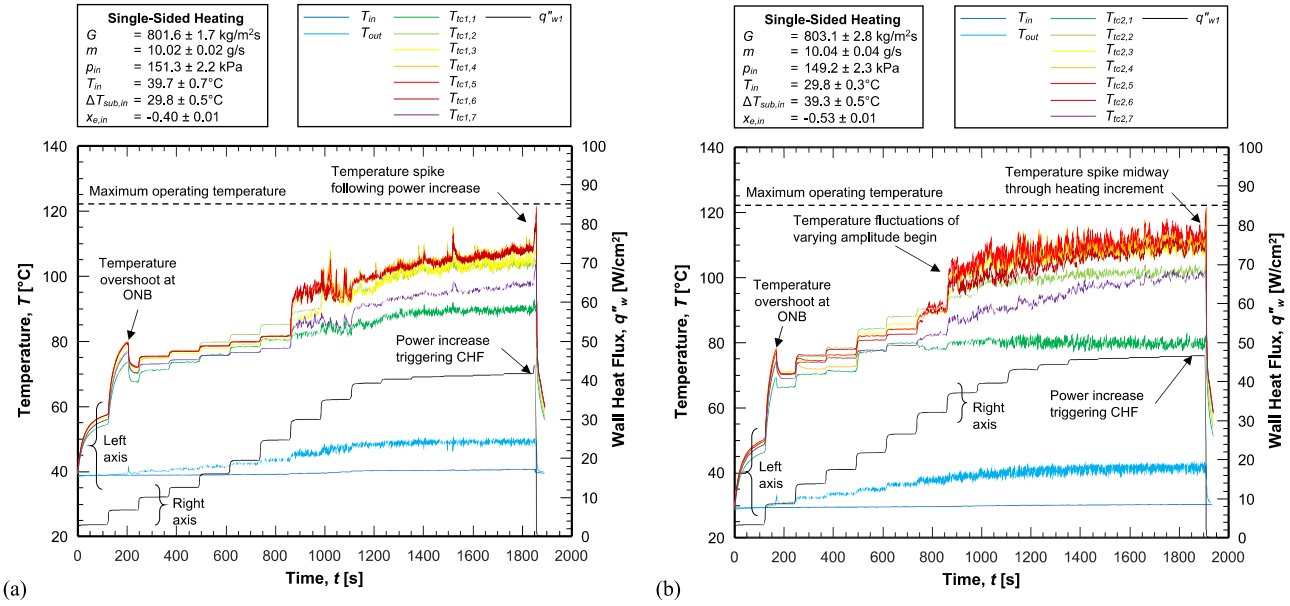

Fig. 20. Temporal records of heated wall substrate temperatures and heater power (proportional to heat flux) for cases in which q''_{CHF} is (a) sensitive and (b) insensitive to variations in inlet subcooling.

ing, respectively. Likewise, Figs. 23(c) and 23(d) mirror the results of q''_{CHF} versus $\Delta T_{sub,}$ in Figs. 19(a) and (b) for single- and double-sided heating, respectively. While no new trends are revealed by nondimensionalizing the CHF results, nondimensional results can easily be applied to results from other databases containing different fluids and operating conditions. Additionally, many common correlations rely on dimensionless groups to predict q''_{CHF} and provide constraints.

4.3. Comparison to earth gravity data

Prior to launch, mission sequence testing (MST) was completed with the FBCE system in Earth gravity to assure its readiness for the ISS. During MST, the FBM was oriented for vertical upflow, and a subset of the operating conditions performed on the ISS were tested [47]. Detailed CHF results with subcooled inlet obtained during MST were previously published [49]. Fig. 24 compare the data obtained on the ISS to the MST results, *i.e.*, microgravity versus Earth gravity results. For single-sided heating, shown in Fig. 24(a), large discrepancies exist between the ISS data and MST data at low mass velocity, and q''_{CHF} is degraded by ~38% at the lowest mass velocity. CHF in microgravity is consistently lower than vertical upflow in g_e, wherein buoyancy facilitates vapor removal from the channel. As mass velocity increases and the influence of buoyancy diminishes relative to inertia, the μg_e results converge towards the g_e vertical upflow results. For double-sided heating, shown in Fig. 24(b), q''_{CHF} in μg_e is almost identical to q''_{CHF} in g_e during vertical upflow at all mass velocities. During double-sided heating, the additional flow acceleration from phase change along two heated walls decreases the relative influence of buoyancy, and closes the gap between μg_e and vertical upflow at lower G than that was observed during single-sided heating.

5. CHF prediction tools

5.1. Assessment of chf correlations

An abundance of flow boiling CHF correlations are readily available in the literature, each tuned to a database comprised of specific fluids, channel geometries and materials, and operating conditions. The vast majority were developed from data acquired in a terrestrial environment and may be unreliable for the present, unique, microgravity database. In a recent study by the present authors [50], a comprehensive assessment of flow boiling CHF correlations was conducted for a large, consolidated, pre-launch, FBCE-CHF database to identify correlations that well predict the current combination of fluid, test section, and approximate operating conditions, regardless of the origin of each correlation. The consolidated database features a rectangular channel with both single- and double-sided heating, a broad range of operating conditions, and Earth-gravity data acquired at different channel orientations and microgravity data acquired onboard a parabolic flight. Correlations are typically designed for either subcooled CHF ($x_{e,CHF} < 0$) or saturated CHF ($x_{e,CHF} \geq 0$) and are assessed with the appropriate subset of the consolidated database, employing the following guidelines:

(i) Correlations that utilize channel diameter D are replaced by hydraulic diameter D_h, otherwise, the length scale prescribed by the original authors is used.
(ii) CHF is assumed to occur at the outlet of the channel corresponding to, $x_{e,CHF} = x_{e,out}$ and $L_{CHF} = L_h$.
(iii) Saturated thermophysical properties are evaluated at either the inlet or outlet pressure, as appropriate, using NIST-REFPROP [46].

The best performing correlations for the microgravity subset of the consolidated database, determined via mean absolute error, MAE, are chosen for an assessment of their predictive capability of the ISS database. MAE, for N data points is calculated as,

$$MAE(\%) = \frac{1}{N}\sum\left|\frac{q''_{CHF,pred} - q''_{CHF,exp}}{q''_{CHF,exp}}\right| \times 100\%. \quad (5)$$

The other statistical parameters evaluated include root mean square error, RMSE, defined as

$$RMSE(\%) = \sqrt{\frac{1}{N}\sum\left(\frac{q''_{CHF,pred} - q''_{CHF,exp}}{q''_{CHF,exp}}\right)^2} \times 100, \quad (6)$$

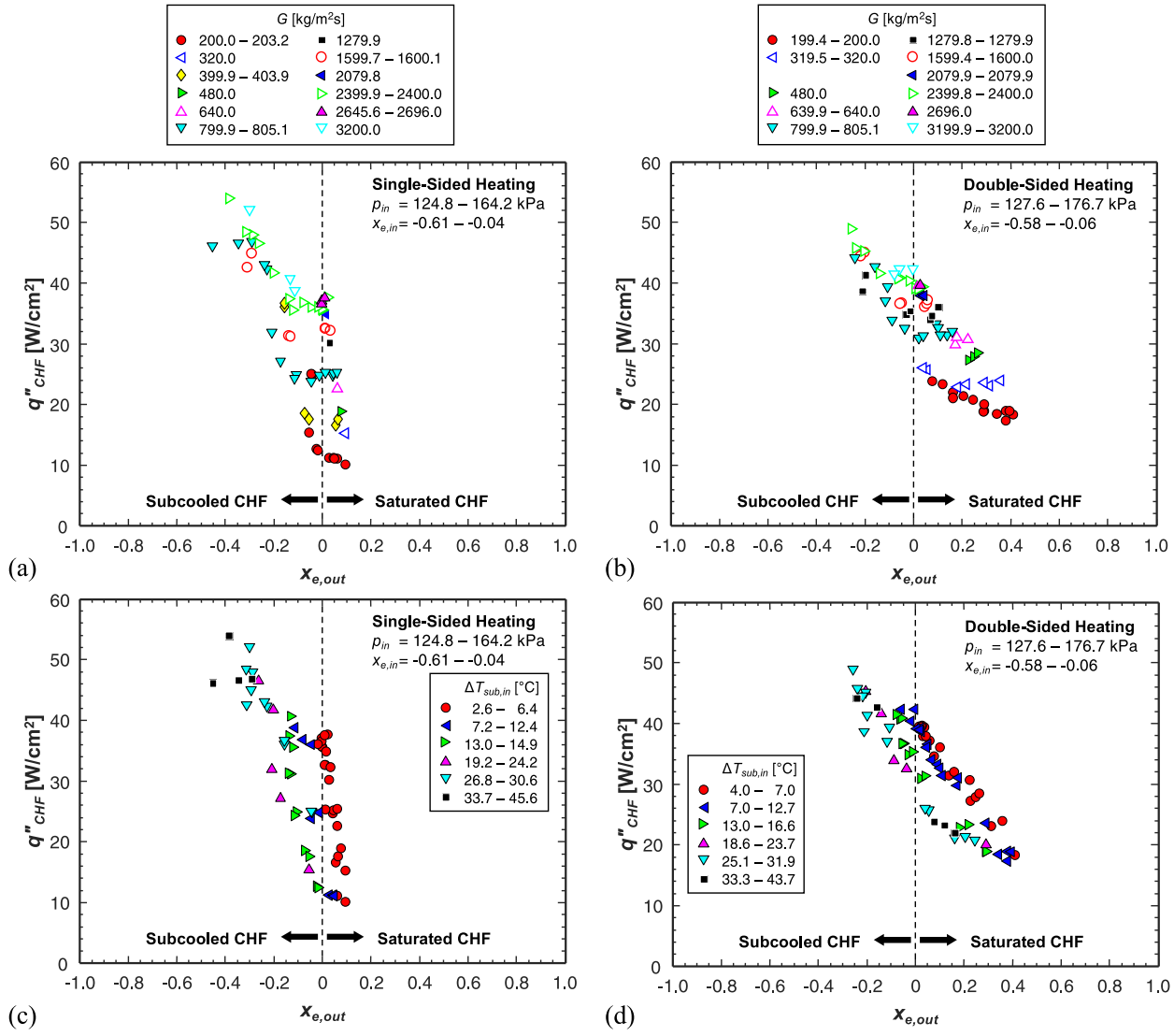

Fig. 21. Variations of experimental CHF results versus outlet equilibrium quality highlighting trends with respect to mass velocity for (a) single- and (b) double-sided heating, and inlet subcooling for (c) single- and (d) double-sided heating.

and the percentage of predictions within ±30% and ±50% of $q''_{CHF,exp}$, ξ_{30} and ξ_{50}, respectively.

Subcooled CHF correlations that are chosen for assessment are listed in Table 2 along with remarks regarding their development and various statistical performance indices, including MAE, RMSE, ξ_{30}, and ξ_{50}. Corresponding parity plots for each correlation and select statistics are presented in Fig. 25. The correlation by the present authors (Darges *et al.* [50]), shown in Fig. 25(a), was developed with the consolidated prelaunch database and yielded the best predictions for subcooled CHF with a MAE of 18.06%. This correlation was developed using data acquired with the present or near-identical test module and operating conditions similar to the present database. Its functional form was chosen to highlight the effects of gravity on flow boiling CHF while capturing other conventional trends. It is equally as accurate for the ISS database as it was for the prelaunch data, which encompassed a variety of buoyancy effects. The correlation by Tso *et al.* [51], shown in Fig. 25(b), was developed from vertical upflow boiling experiments in a rectangular channel using FC-72 (a commercial mixture of different perfluorohexane isomers resulting in near-identical properties to nPFH). These similarities resulted in a relatively low MAE of 22.01%, even though only a small portion of the present database falls within the correlation's recommended application range. A slightly larger drop-off of accuracy, MAE = 43.28%, resulted from the correlation by Celata *et al.* [52], shown in Fig. 25(c). Their correlation was developed from a consolidated CHF database comprised of water in small diameter circular channels, and consistently under-predicted the database. Similarly, the correlation by Sarma *et al.* [53], depicted in Fig. 25(d) under-predicted the database and was developed for water and R-12. The form of the correlation was inspired by the evaporation of a liquid layer underneath a slug bubble, which differs from the mechanism of CHF experienced in the present study. Regardless, the correlation performs reasonably well with an MAE of 51.52%.

The best performing saturated CHF correlations for microgravity data subset of the prelaunch consolidated FBM database are listed in Table 3, with corresponding parity plots shown in Fig. 26. Mirroring subcooled CHF, the correlation by the present authors [50], which is applicable for both subcooled and saturated CHF, performed the best with a MAE of 18.82% and is featured in Fig. 26(a).

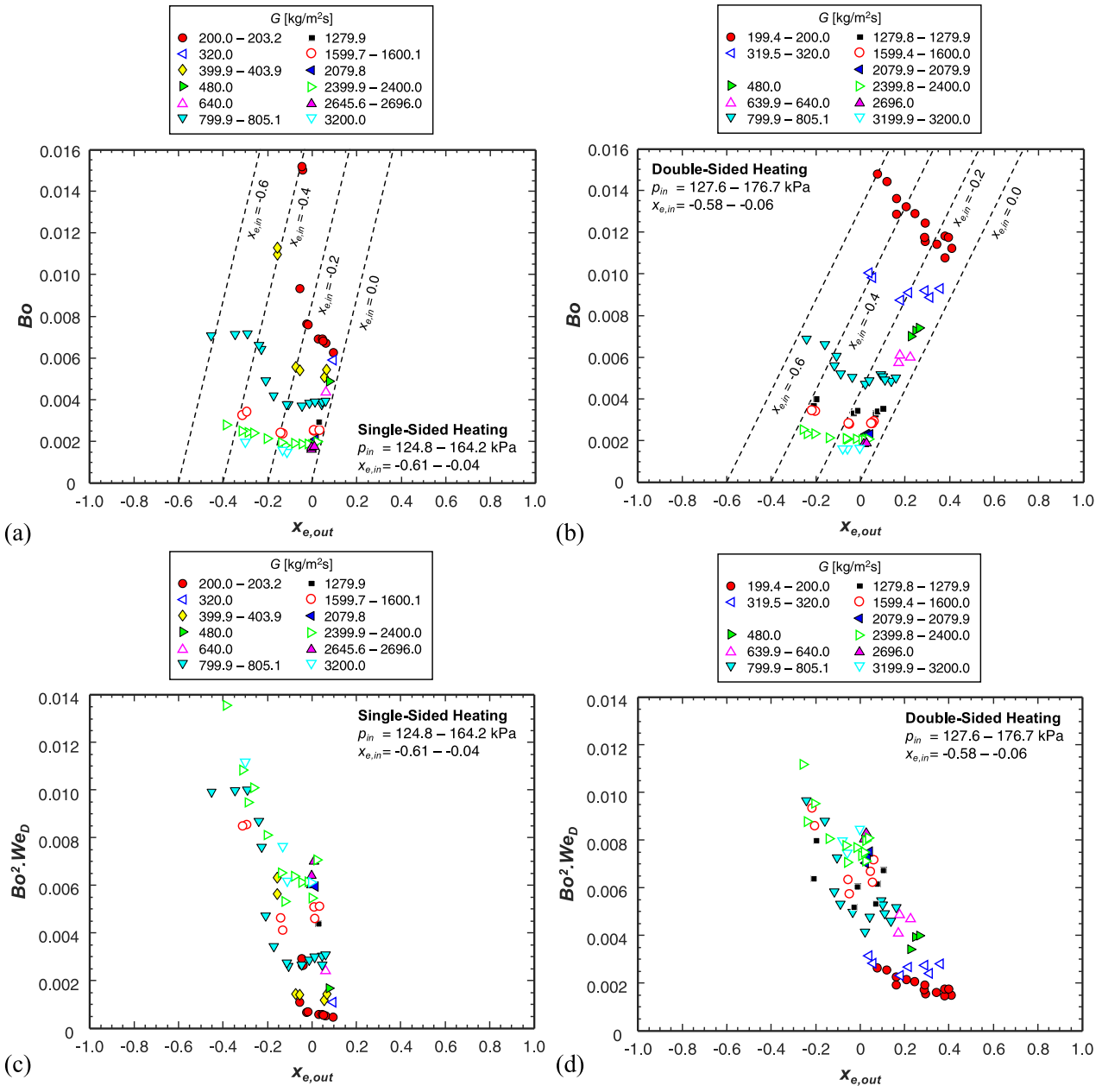

Fig. 22. Variations of dimensionless experimental CHF results versus outlet equilibrium quality: *Bo* vs $x_{e,out}$ for (a) single- and (b) double-sided heating, and Bo^2We_D vs $x_{e,out}$ for (c) single- and (d) double-sided heating.

Tibiriçá *et al.* [54] took inspiration from the correlation by Katto and Ohno [35] and developed their own correlation, shown in Fig. 26(b), to fit their database of uniformly heated elliptical tubes. Despite the niche intended application, their correlation yielded good predictions and resulted in an MAE of 23.36%. Its parent correlation, by Katto and Ohno [35], is one of the most robust and popular correlations for saturated flow boiling CHF in uniformly heated tubes. It was validated for 15 different fluids and a broad range of operating conditions during its development and predicted the ISS database reasonably well with an MAE of 31.55%, as shown in Fig. 26(c). Zhang *et al.* [55] consolidated a CHF database consisting of water in uniformly heated tubes and developed a correlation for saturated CHF. Their correlation, shown in Fig. 26(d), covered a broad range of operating conditions and consistently under-predicted the ISS database with a MAE of 40.84%.

5.2. Interfacial lift-off model

5.2.1. Model description

The observations of flow patterns in Section 3 justify the use of the *Interfacial Lift-off Model* to predict q''_{CHF}. Originally proposed by Galloway and Mudawar in [56], the *Interfacial Lift-off Model* describes a periodic wavy vapor layer that develops along the heated wall leading up to CHF. Fig. 27 depicts a schematic of the modeled flow patterns for double-sided heating; single-sided would be similar but with only one vapor layer. Preceding CHF, cooling of the heated wall is sustained at troughs in the wavy vapor layer, known as wetting fronts, where the bulk liquid is permitted access to the wall. Boiling at wetting fronts is assumed to be the primary source of heat dissipation for the heated wall. CHF is postulated to occur once the momentum (normal to the heated wall) of va-

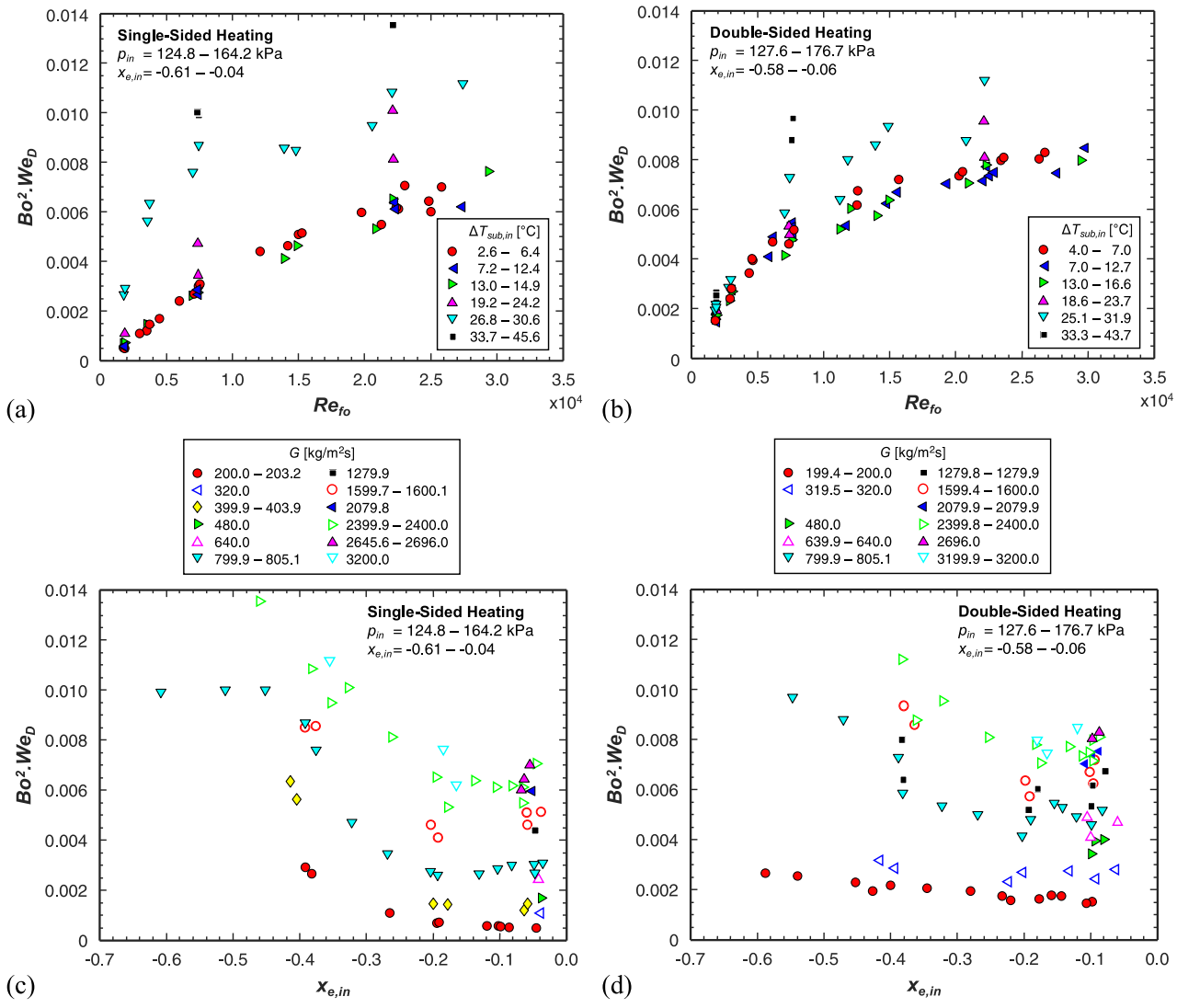

Fig. 23. Variations of dimensionless experimental CHF results versus liquid Reynolds number for (a) single-and (b) double-sided heating, and inlet equilibrium quality for (c) single- and (d) double-sided heating.

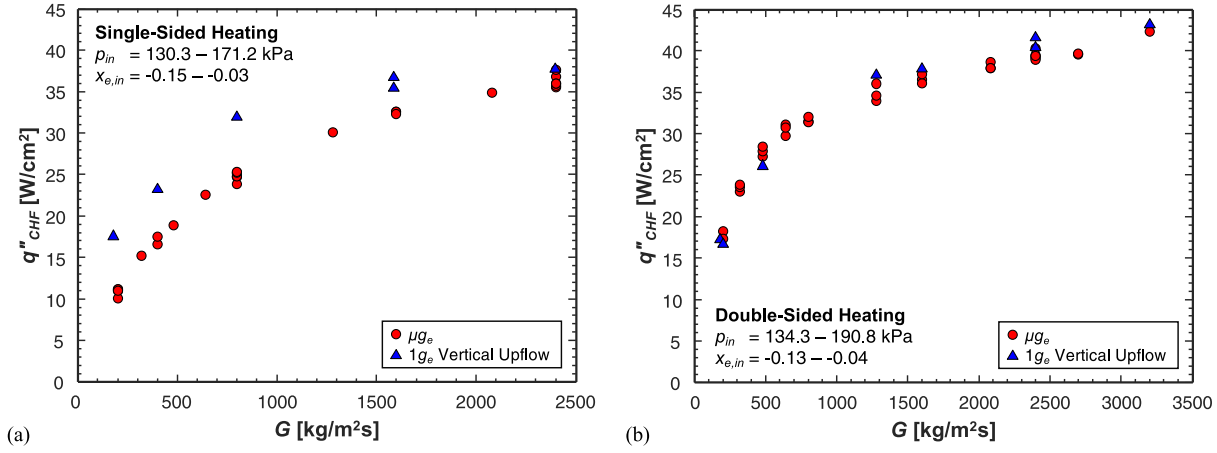

Fig. 24. Comparison of experimental CHF results in microgravity (from ISS experiments [40,41]) to Earth gravity (pre-launch ground experiments [49]) for (a) single- and (b) double-sided heating.

Table 2
Selected correlations applicable to subcooled CHF.

Correlation	Remarks	Recommended/Validated Applicability Ranges	Assessment Statistics
Darges *et al.* (2022) [50] $Bo = 0.353We_{D_e}^{-0.314}\left(\frac{L_h}{D_e}\right)^{-0.226}\left(\frac{\rho_f}{\rho_g}\right)^{-0.481}\left(1-\left(\frac{\rho_f}{\rho_g}\right)^{-0.094}x_{e,in}\right)$ $\ldots\left(1+0.034\frac{1}{Fr_{\theta,D_e}}\right)\left(1+0.008\frac{Bd_{\theta,D_e}}{We_{D_e}^{0.543}}\right)$	• Based on inlet conditions • nPFH • Any orientation • g_e and μg • Rectangular channel heated on 1 or 2 opposite walls • Developed from a consolidated database of 417 datapoints	We_{De} = 15.24 – 19,540.26 L_h/D_e = 5.73 – 11.46 ρ_f/ρ_g= 48.15 – 123.90 $x_{e,in}$ = −0.50 – 0.68 $1/Fr_{\theta,De}$ = −5.82 – 14.68 $Bd_{\theta,De}$ = −864.80 – 865.34 Bo = 0.0012 – 0.0285	MAE = 18.06% RMSE = 21.74% ξ_{30} = 81.54% ξ_{50} = 100.00%
Tso *et al.* (2000) [51] $\frac{q''_{CHF}}{\rho_g u h_{fg}} = 0.203We_L^{\frac{-11}{23}}\left(\frac{\rho_f}{\rho_g}\right)^{\frac{15}{23}}\left(\frac{L_h}{D_h}\right)^{\frac{1}{23}}\left(1+\frac{c_{p,f}\Delta T_{sub,in}}{h_{fg}}\right)^{\frac{7}{23}}$ $\times\left(1+0.021\frac{\rho_f}{\rho_g}\frac{c_{p,f}\Delta T_{sub,in}}{h_{fg}}\right)^{\frac{16}{23}}$	• Based on inlet conditions • FC-72 • Vertical upflow • Rectangular channel • Developed using 16 datapoints	We_L = 1 – 1000	MAE = 22.01% RMSE = 40.32% ξ_{30} = 83.08% ξ_{50} = 89.23%
Celata *et al.* (1994) [52] $Bo = \frac{C}{Re^{0.5}}$; $C = (0.216 + 4.74\times10^{-2}p)\Psi$ p is in MPa $\Psi = \begin{cases} 1, & x_{e,out} < -0.1 \\ 0.825 + 0.986x_{e,out}, & -0.1 < x_{e,out} < 0 \\ 1/(2+30x_{e,out}), & x_{e,out} > 0 \end{cases}$	• Based on outlet conditions • Water • Not orientation-specific • Small diameter circular channels • Validated for a consolidated database of 1865 datapoints	D = 0.3 – 25.4 mm L_h = 2.5 – 610 mm G = 900 – 90,000 kg/m^{2}s p = 0.1 – 8.4 MPa T_{in} = 0.3 – 242.7°C q''_{CHF} = 3.3 – 227.9 MW/m^2	MAE = 43.28% RMSE = 45.59% ξ_{30} = 16.92% ξ_{50} = 73.85%
Sarma *et al.* (2006) [53] $Bo = 0.118\mathrm{Re}^{-0.23}p_r^{0.2}\left(\frac{D}{L_h}\right)^{0.45}\left(\frac{c_{p,f}\Delta T_{sub}}{h_{fg}}\right)$	• Based on inlet conditions • Water and R-12 • Not orientation-specific • Small diameter circular tubes • Validated for a consolidated database consisting of 2718 datapoints	D = 0.25 – 37.5 mm L_h =1.77 – 2300 mm G = 385.3 – 90,000 kg/m^{2}s p = 0.953 – 206.69 bar T_{in} = 1.5 – 354.03°C q''_{CHF} = 1.104 – 227.95 MW/m^2	MAE = 51.52% RMSE = 53.55% ξ_{30} = 6.15% ξ_{50} = 46.15%

por generated at the wetting front overcomes the pressure force exerted by the curvature of the interface. At this point, the wetting front lifts off the heated wall. The ensuing axial conduction upstream provokes a chain-reaction-like process marching upstream, during which, wetting fronts are extinguished one by one until a vapor blanket covers the entire wall. The *Interfacial Lift-off Model* has since been adapted to handle q''_{CHF} predictions for a broad range of operating conditions. A brief summary regarding details of the model and its procedure will be provided, with key equations of the model for both single-sided and double-sided heating available in Table 4. For the present microgravity database, the gravitational acceleration is negligible and $g \approx 0$. This renders the inclination angle of the channel, θ, irrelevant. Further details of the model, including its application to Earth gravity, are provided in [49].

The *Interfacial Lift-Off Model* can be divided into four sub-models. First, a separated flow model is used to predict local pressure, phase velocities, quality, and void fraction along the length of the channel. The following assumptions are made during the separated flow model:

(1) Vapor layer is initiated at the leading edge of the heated wall.
(2) Velocity of each phase is uniform within the channel's cross-section.
(3) Pressure is uniform across the channel's entire cross-section.
(4) Vapor is maintained at the local saturation temperature.
(5) Vapor produced at the wetting front does not contribute to streamwise momentum.
(6) In the case of double-sided heating, equal heat flux is applied to each heated wall.

In order to capture non-equilibrium effects that occur in subcooled CHF ($x_{e,out} < 0$), the heat utility ratio, ε, proposed by Zhang *et al.* [57] is included within the separated flow model. The heat utility ratio partitions total heat flux into the portions going to sensible heat of the bulk fluid or latent heat of the near-wall fluid. For saturated CHF, $x_{e,out} \geq 0$, the heat utility ratio is fixed to unity by assuming all the heat transferred to the working fluid goes into vaporizing the fluid, and the bulk fluid temperature remains constant. As shown in Table 4, the heat utility ratio is an empirical correlation developed from a database of the authors' own experiments and those by Sturgis and Mudawar [58]. The heat utility ratio was later adapted by the present authors [49] and shown to be effective for their own database.

The second sub-model is based on classic instability analysis of two-fluid systems moving at different velocities [59,60]. This assumes a wavy sinusoidal interface described by $\eta(z,t)$ which exists between the two fluids and moves at a wave speed, c. The stability of the interface can be determined by the relative magnitudes of inertia, surface tension, and body force. From this, both the critical wavelength, λ_c, corresponding to the wavelength of the interface that triggers instability, and the pressure force associated with the interface's curvature, are calculated. As shown in Fig. 27, the absence of body force in μg_e results in an identical critical wavelength for each heated wall. In environments with an influential gravitational field, a component of gravity perpendicular the heated surface would result in different λ_c along each heated wall.

The final two sub-models are used in tandem to find the wall heat flux needed to trigger CHF. An energy balance at the wetting front yields the momentum of vapor emitting from the wetting front, which is equated to the pressure force determined from the

Table 3
Selected correlations applicable to saturated CHF.

Correlation	Remarks	Recommended/Validated Applicability Ranges	Assessment Statistics
Darges *et al.* (2022) [50] $Bo = 0.353We_{D_e}^{-0.314}\left(\frac{L_h}{D_e}\right)^{-0.226}\left(\frac{\rho_f}{\rho_g}\right)^{-0.481}\left(1-\left(\frac{\rho_f}{\rho_g}\right)^{-0.094}x_{e,in}\right)$ $\ldots\left(1+0.034\frac{1}{Fr_{\theta,D_e}}\right)\left(1+0.008\frac{Bd_{\theta,D_e}}{We_{D_e}^{0.543}}\right)$	• Based on inlet conditions • nPFH • Any orientation • g_e and μg • Rectangular channel heated on 1 or 2 opposite walls • Developed from a consolidated database of 417 datapoints	We_{De} = 15.24 – 19,540.26 L_h/D_e = 5.73 – 11.46 ρ_f/ρ_g= 48.15 – 123.90 $x_{e,in}$ = −0.50 – 0.68 $1/Fr_{\theta,De}$ = −5.82 – 14.68 $Bd_{\theta,De}$ = −864.80 – 865.34 Bo = 0.0012 – 0.0285	MAE = 18.81% RMSE = 20.26% ξ_{30} = 93.06% ξ_{50} = 100.00%
Tibiriçá et al. (2012) [54] $q''_{CHF} = \min(q''_1, q''_2) \times (1+\max(K_1,K_2)\frac{(h_f-h_{in})}{h_{fg}})$ $q''_1 = CGh_{fg}\left(\frac{\sigma\rho_f}{G^2L_{eq}}\right)^{0.0298}\frac{D_{eq}}{L_{eq}}$ $q''_2 = 0.06213Gh_{fg}\left(\frac{\rho_g}{\rho_f}\right)^{0.085}\left(\frac{\sigma\rho_f}{G^2L_{eq}}\right)^{0.31348}\frac{1}{1+0.0031\frac{L_{eq}}{D_{eq}}}$ $K_1 = \frac{1.043}{4C\left(\frac{\sigma\rho_f}{G^2L_{eq}}\right)^{0.043}}$; $K_2 = \frac{5\left(0.0124+\frac{D_{eq}}{L_{eq}}\right)}{6\left(\frac{\rho_g}{\rho_f}\right)^{0.133}\left(\frac{\sigma\rho_f}{G^2L_{eq}}\right)^{\frac{1}{3}}}$ $C = \begin{cases}0.25, & L_{eq}/D_{eq} < 50\\ 0.25+0.00076(L_{eq}/D_{eq}-50), & 50 \le L_{eq}/D_{eq} \le 150\\ 0.32576, & L_{eq}/D_{eq} > 150\end{cases}$ $D_{eq} = \sqrt{\frac{4A_c}{\pi}}$; $L_{eq} = \frac{P_hL_h}{\pi D_{eq}}$	• Based on inlet conditions • R-134a, R-245fa, R-1234ze(E) • Horizontal flow • Uniformly heated elliptical tubes of different aspect ratios • Developed using a consolidated database of 150 datapoints	D = 1.0 – 2.2 mm L_h = 90 – 361 mm β = 0.25 – 4 G = 100 – 1500 kg/m^{2}s $\Delta T_{sub,in}$ = 4 – 10°C	MAE = 23.36% RMSE = 30.64% ξ_{30} = 75.00% ξ_{50} = 88.89%
Katto & Ohno (1984) [35] $q''_{CHF} = q''_o\left(1+K\frac{(h_f-h_{in})}{h_{fg}}\right)$ If $\rho_g/\rho_f < 0.15$: $q''_o = \begin{cases}q''_{o2}, & q''_{o2} < q''_{o3}\\ \max\left(q''_{o3}, q''_{o4}\right), & q''_{o2} > q''_{o3}\end{cases}$; $K = \max\left(\ K_6,\quad K_7\ \right)$ If $\rho_g/\rho_f > 0.15$: $q''_o = \begin{cases}q''_{o2}, & q''_{o2} < q''_{o13}\\ \max\left(q''_{o13}, q''_{o5}\right), & q''_{o2} > q''_{o13}\end{cases}$; $K = \begin{cases}K_6, & K_6 > K_7\\ \min(K_7, K_9), & K_6 < K_7\end{cases}$ $\frac{q''_{o2}}{Gh_{fg}} = CWe_L^{-0.043}\frac{D}{L_h}$; $\frac{q''_{o3}}{Gh_{fg}} = 0.10\left(\frac{\rho_g}{\rho_f}\right)^{0.133}We_L^{-\frac{1}{3}}\frac{1}{1+0.0031\frac{L_h}{D}}$ $\frac{q''_{o4}}{Gh_{fg}} = 0.098\left(\frac{\rho_g}{\rho_f}\right)^{0.133}We_L^{-0.433}\frac{\left(\frac{L_h}{D}\right)^{0.27}}{1+0.0031\frac{L_h}{D}}$ $\frac{q''_{o5}}{Gh_{fg}} = 0.0384\left(\frac{\rho_g}{\rho_f}\right)^{0.6}We_L^{-0.173}\frac{1}{1+0.28We_L^{-0.233}\frac{L_h}{D}}\frac{q''_{o13}}{Gh_{fg}} =$ $0.234\left(\frac{\rho_g}{\rho_f}\right)^{0.513}We_L^{-0.433}\frac{\left(\frac{L_h}{D}\right)^{0.27}}{1+0.0031\frac{L_h}{D}}$ $C = \begin{cases}0.25, & L_h/D < 50\\ 0.25+0.0009(\frac{L_h}{D}-50), & 50 \le L_h/D \le 150\\ 0.34, & L_h/D > 150\end{cases}$ $K_6 = \left(\frac{1.043}{4CWe_L^{-0.043}}\right)$; $K_7 = \left(\frac{5(0.0124+\frac{D}{L_h})}{6\left(\frac{\rho_g}{\rho_f}\right)^{0.133}We_L^{-\frac{1}{3}}}\right)$ $K_8 = 0.416\left(\frac{\left(0.0221+\frac{D}{L_h}\right)\left(\frac{D}{L_h}\right)^{0.27}}{\left(\frac{\rho_g}{\rho_f}\right)^{0.133}We_L^{-0.433}}\right)$; $K_9 = 1.12\left(\frac{1.52We_L^{-0.233}+\frac{D}{L_h}}{\left(\frac{\rho_g}{\rho_f}\right)^{0.6}We_L^{-0.173}}\right)$	• Based on inlet conditions • Water, anhydrous ammonia, benzene, ethanol, helium I, para-hydrogen, monoisopropylbiphenyl, nitrogen, potassium, R-12, R-21, R-22, R-113, R-114, R-115 • Vertical upflow • Uniformly heated circular tubes • Validated for a consolidated database consisting of > 1000 datapoints	D = 1 – 38.1 mm L_h/D = 5 – 940 ρ_g/ρ_f = 0.00027 – 0.517	MAE = 31.55% RMSE = 33.10% ξ_{30} = 26.39% ξ_{50} = 100.00%
Zhang et al. (2006) [55] $Bo = 0.0352\left(We_D+0.0119\left(\frac{L_h}{D_h}\right)^{2.31}\left(\frac{\rho_g}{\rho_f}\right)^{0.361}\right)^{-0.295}$ $\times\left(\frac{L_h}{D_h}\right)^{-0.311}\left(2.05\left(\frac{\rho_g}{\rho_f}\right)^{0.170}-x_{e,in}\right)$	• Based on inlet conditions • Water • Not orientation-specific • Uniformly heated small diameter circular tubes • Developed from a consolidated database containing 3837 datapoints, of which 2539 are saturated • Database consists of both subcooled and saturated data • Hall & Mudawar (2000) was recommended for subcooled CHF predictions (as discussed in [50])	D = 0.33 – 6.22 mm L/D = 1.0 – 975 p_{out} = 0.101 – 19.0 MPa G = 5.33 – 134,000 $x_{e,in}$ = −2.35 – 0.00 $x_{e,out}$ = −1.75 – 0.999 q''_{CHF} = 0.00935 – 276 MW/m^2	MAE = 40.84% RMSE = 41.91% ξ_{30} = 11.11% ξ_{50} = 75.00%

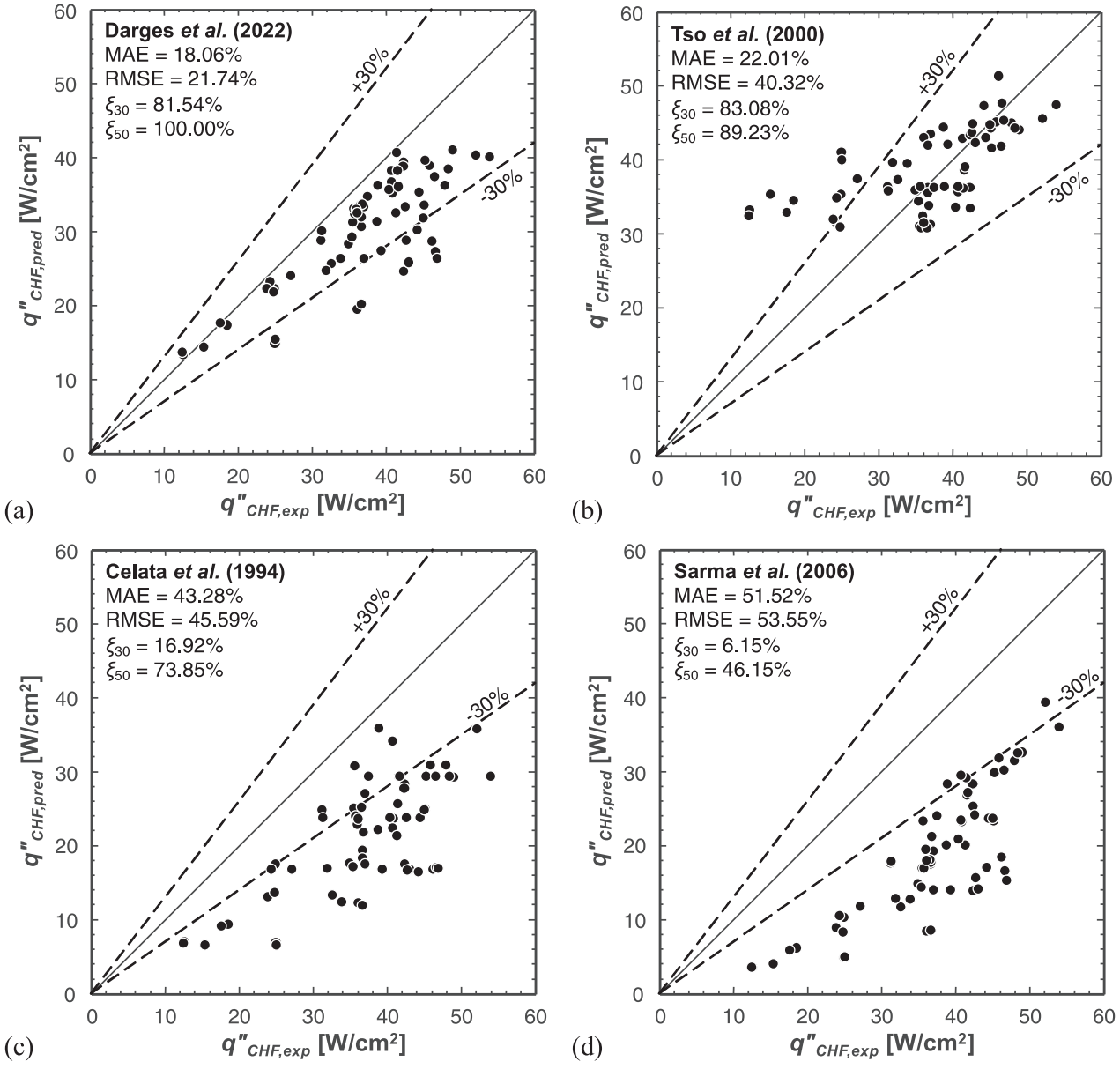

Fig. 25. Parity plots of correlations for subcooled CHF: (a) Darges et al. (2022) [50], (b) Tso *et al.* (2000) [51], (c) Celata et al. (1994) [52], and (d) Sarma et al. (2006) [53].

instability analysis. An energy balance is then performed for the entire wall to relate the supplied wall heat flux to the heat flux at the wetting front required for lift-off.

The *Interfacial Lift-off Model* is iterative in its procedure, due to the implicit relationship between the critical wavelength, local properties, and applied heat flux. The model is initiated by assuming q''_{CHF} and using the separated flow model coupled with a fourth-order Runge-Kutta to advance along the channel until the axial location where the velocity of the vapor layer along the heated wall surpasses the velocity of the bulk liquid, z_o. From z_o, a critical wavelength is assumed, and the separated flow model continues until z^* defined as $z^* = z_o+\lambda_c$. At z^*, the local properties are used to calculate the critical wavelength using the equation in Table 4. This process is repeated until the locally calculated critical wavelength matches the assumed value. Once the critical wavelength is determined, the equation for q''_{CHF} in Table 4 is evaluated at z^*. Again, if the calculated q''_{CHF} does not match the assumed q''_{CHF}, an updated q''_{CHF} is assumed, and the entire process is repeated until convergence is reached. For a case with double-sided heating, the *Interfacial Lift-off Model* is performed for both heated walls and the resulting lower value yields the true q''_{CHF}. However, in the absence of gravity perpendicular to the heated wall, predictions will be identical for each wall.

5.2.2. Comparison of model predictions to experimental data

Previous studies [61] have identified operating conditions in a terrestrial environment which the wavy vapor interface is not observed, and the Interfacial Lift-off Model is not applicable. However, the wavy vapor interface is observed for the present operating range tested in microgravity, agreeing with preliminary microgravity experiments performed via parabolic flight [10,12]. Hence,

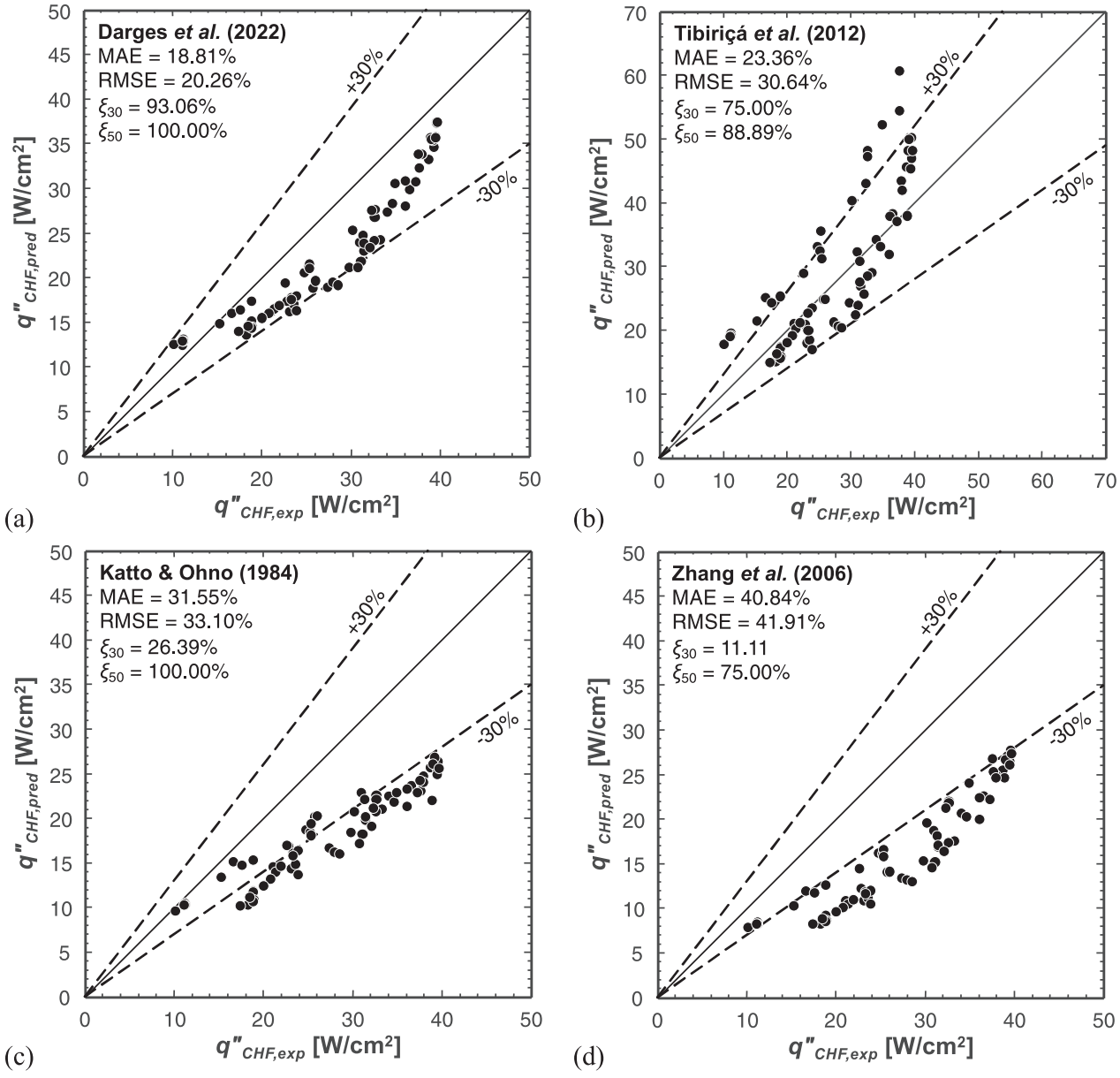

Fig. 26. Parity plots of correlations for saturated CHF: (a) Darges et al. (2022) [50], (b) Tibiriçá *et al.* (2012) [54], (c) Katto & Ohno (1984) [35], and (d) Zhang et al. (2006) [55].

predictions of $q"_{CHF}$ are made with the Interfacial Lift-off Model for the entire ISS database with subcooled inlet. The model predicts the present database with an overall MAE of 23.09%, and a parity plot of the results is presented in Fig. 28(a). The model performs similarly for single- and double-sided with MAEs of 25.26% and 21.13%, respectively. The majority (65.44%) of datapoints are predicted within ±30% error, while all datapoints are predicted within ±50% error. Overall, the Interfacial Lift-off model performs satisfactorily, even outperforming most correlations. Figs. 28(b) and (c) show variations of error with respect to mass velocity and inlet subcooling, respectively. The model generally underpredicts the present database with a larger spread of error produced at relatively low mass velocity and low inlet subcooling.

In order to highlight trends of the sub-models, Table 5 includes outputs from the separated flow model and instability analysis for select cases (the ISS case reference numbers are as per [40,41]). Results from different mass velocities at two subcooling ranges are chosen for both single- and double-sided heating. The leading columns until $q"_{CHF,exp}$, which is included for reference, are inputs into the model. Following and including column $q"_{CHF,pred}$ are outputs from various components of the model. Some key trends are, for each subcooling range, the critical wavelength, λ_c, and vapor layer thickness, δ, decrease with increasing mass velocity. Similarly observed in flow visualization, provided in Figs. 11 and 14 for single- and double-sided heating, respectively, cases with higher mass velocity resulted in thinner vapor layers with shorter vapor structures. Decreasing the distance between wetting fronts, or wavelength of the interface, with increasing mass velocity corresponds to increasing $q"_{CHF,pred}$. The two subcooling ranges output similar results for each mass velocity. However the heat utility ratio, ε, is lesser at higher subcooling, resulting in greater $q"_{CHF,pred}$.

Table 4
Summary of equations used in the *Interfacial Lift-off Model.*

Conservation of momentum for single-sided heating

$$G^2\frac{d}{dz}\left[\frac{x_1^2}{\rho_g\alpha_1}\right] = -\alpha_1\frac{dp}{dz} - \frac{\tau_{w1,g}P_{w1,g}}{A_c} \pm \frac{\tau_i P_i}{A_c} - \rho_g\alpha_1 g\sin\theta$$

$$G^2\frac{d}{dz}\left[\frac{(1-x_1)^2}{\rho_b(1-\alpha_1)}\right] = -(1-\alpha_1)\frac{dp}{dz} - \frac{\tau_{w,b}P_{w,b}}{A_c} \mp \frac{\tau_i P_i}{A_c} - \rho_b(1-\alpha_1)g\sin\theta$$

Conservation of momentum for double-sided heating

$$G^2\frac{d}{dz}\left[\frac{x_1^2}{\rho_g\alpha_1}\right] = -\alpha_1\frac{dp}{dz} - \frac{\tau_{w1,g}P_{w1,g}}{A_c} \pm \frac{\tau_{i,1}P_{i,1}}{A_c} - \rho_g\alpha_1 g\sin\theta$$

$$G^2\frac{d}{dz}\left[\frac{x_2^2}{\rho_g\alpha_2}\right] = -\alpha_2\frac{dp}{dz} - \frac{\tau_{w2,g}P_{w2,g}}{A_c} \pm \frac{\tau_{i,2}P_{i,2}}{A_c} - \rho_g\alpha_2 g\sin\theta$$

$$G^2\frac{d}{dz}\left[\frac{(1-x_1-x_2)^2}{\rho_b(1-\alpha_1-\alpha_2)}\right] = -(1-\alpha_1-\alpha_2)\frac{dp}{dz} - \frac{\tau_{w,b}P_{w,b}}{A_c} \mp \frac{\tau_{i,1}P_{i,1}}{A_c} \mp \frac{\tau_{i,2}P_{i,2}}{A_c} - \rho_b(1-\alpha_1-\alpha_2)g\sin\theta$$

Local vapor velocity

$$u_{ga} = \frac{x_a G}{\rho_g\alpha_a}$$

Local liquid velocity (single-sided heating)

$$u_f = \frac{(1-x_1)G}{(1-\alpha_1)\rho_b}$$

Local liquid velocity (double-sided heating)

$$u_f = \frac{(1-x_1-x_2)G}{(1-\alpha_1-\alpha_2)\rho_b}$$

Wall shear stress [62]

$$\tau_{w,k} = \frac{1}{2}\rho_k u_k f_k$$

Wall friction factor

$$f_k = C_1 + \frac{C_2}{Re_k^{1/C_3}}$$

Phase Reynolds number

$$Re_k = \frac{\rho_k u_k D_k}{\mu_k}$$

Friction factor constants for laminar flow ($Re_k \le 2100$)

$C_1 = 0\,;\, C_2 = 16\,;\, C_3 = 1$

Friction factor constants for transitional flow ($2100 < Re_k \le 4000$)

$C_1 = 0.0054\,;\, C_2 = 2.3\times10^{-8}\,;\, C_3 = -2/3$

Friction factor constants for turbulent flow ($Re_k > 4000$)

$C_1 = 0.00128\,;\, C_2 = 0.1143\,;\, C_3 = 3.2154$

Interfacial shear stress

$\tau_{ia} = C_{f,a}\rho_g(u_{ga}-u_f)^2$ where $C_{f,i} = 0.5$ [56]

Conservation of energy

$$\frac{dx_a}{dz} = \frac{\varepsilon q''_w W}{GA[h_{fg}(z)+\Delta h_{sub}]}$$

Local liquid enthalpy (single-sided heating)

$$h_b = \frac{h_{in} - x_1 h_g + \frac{q''_w P_h}{GA_c}z}{(1-x_1)}$$

Local liquid velocity (double-sided heating)

$$h_b = \frac{h_{in} - (x_1+x_2)h_g + \frac{q''_w P_h}{GA_c}z}{(1-x_1-x_2)}$$

Critical wavelength

$$k_{c,a} = \frac{2\pi}{\lambda_{c,a}} = \frac{\rho''_b\rho''_{ga}(u_{ga}-u_f)^2}{2\sigma(\rho''_b+\rho''_{ga})} + \sqrt{\left[\frac{\rho''_b\rho''_{ga}(u_{ga}-u_f)^2}{2\sigma(\rho''_b+\rho''_{ga})}\right]^2 + \frac{(\rho_b-\rho_{ga})g_n}{\sigma}}$$

where $\rho''_{ga} = \rho_{ga}\coth(k\delta_a)$ and $\rho''_b = \begin{cases}\rho_b\coth(k(H-\delta_1)), \text{single}-\text{sided}\\ \rho_b\coth(k(H-\delta_1-\delta_2)), \text{double}-\text{sided}\end{cases}$

Lift-off criteria

$$q''_{CHF,a} = \begin{cases}\frac{\rho_g}{\varepsilon}(c_{p,f}\Delta T_{sub,out}+h_{fg})\left[\frac{4\pi\sigma b}{\rho_g}\sin(\pi b)\right]^{0.5}\frac{\delta_a^{0.5}}{\lambda_{c,a}}\Big|_{z^*}, & x_{e,out}<0\\ \rho_g(c_{p,f}\Delta T_{sub,in}+h_{fg})\left[\frac{4\pi\sigma b}{\rho_g}\sin(\pi b)\right]^{0.5}\frac{\delta_a^{0.5}}{\lambda_{c,a}}\Big|_{z^*}, & x_{e,out}\ge 0\end{cases}$$

Heat utility ratio

$$\varepsilon = 1 - 0.00285\frac{\rho_f}{\rho_g}\frac{c_{p,f}\Delta T_{sub,out}}{h_{fg}}\left(\frac{\rho_f u_{in}^2 D}{\sigma}\right)$$

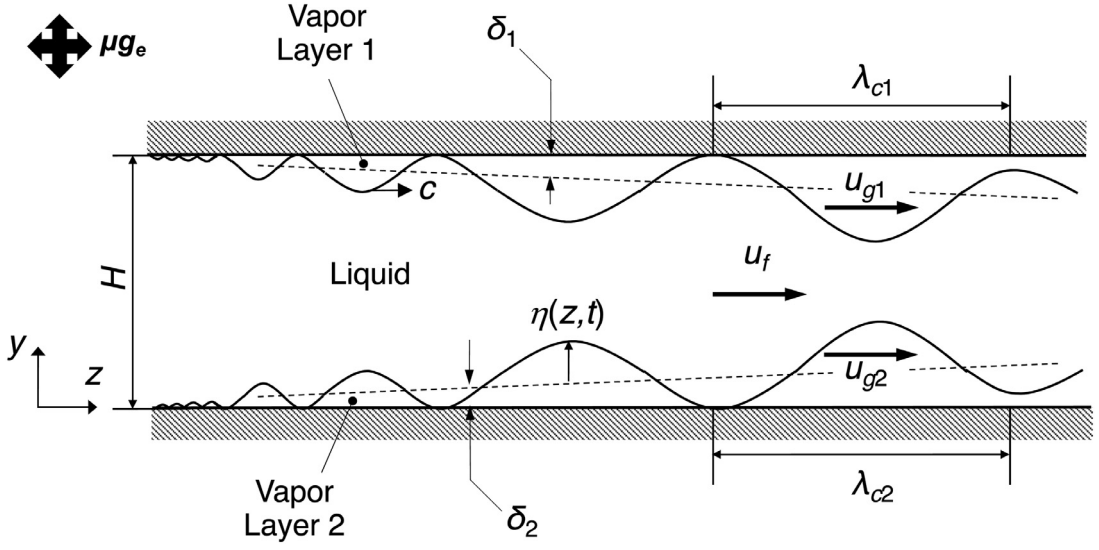

Fig. 27. Schematics of the idealized formation of wavy liquid-vapor interface in μg_e.

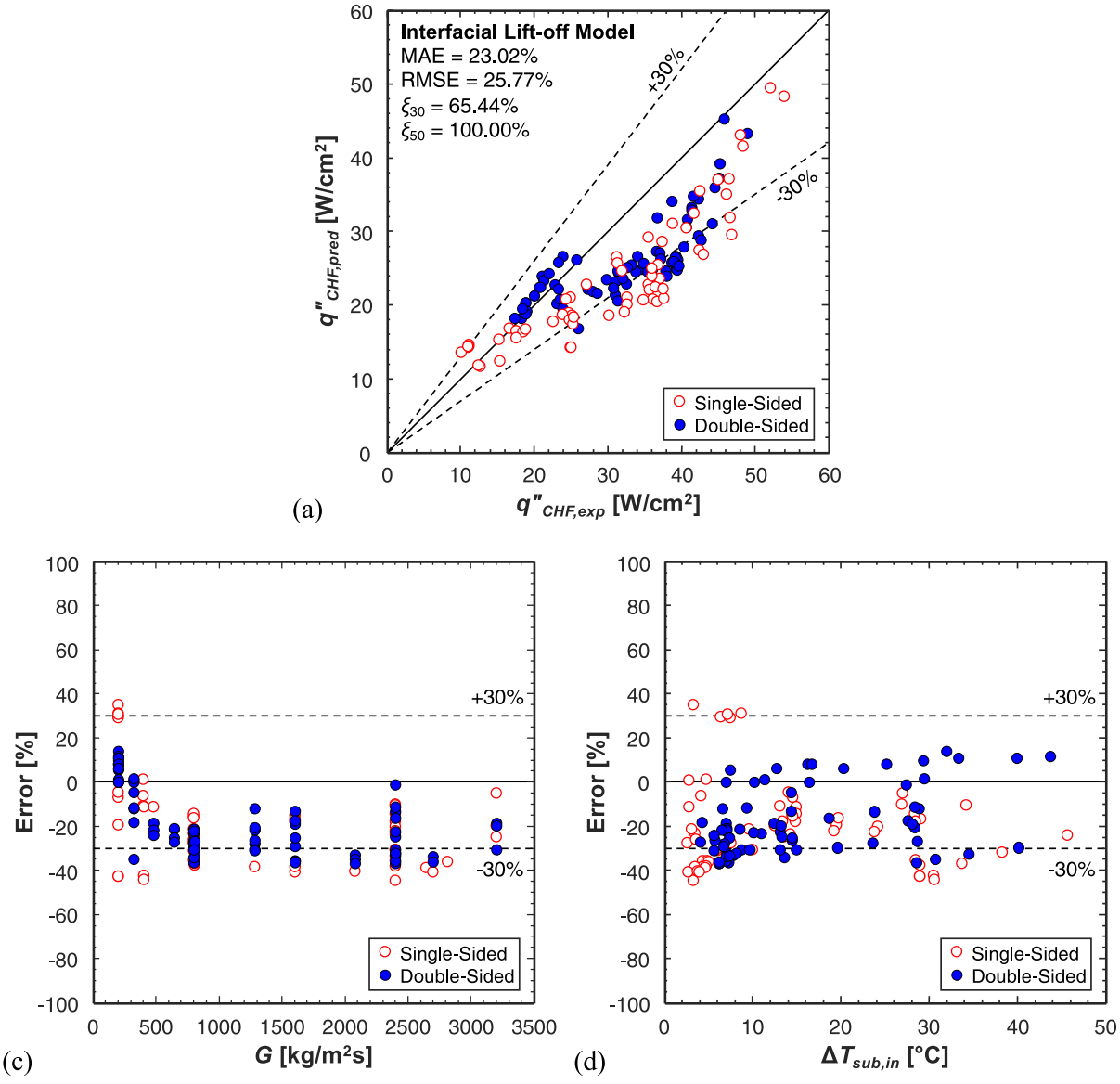

Fig. 28. (a) Parity plot of predictions by the *Interfacial Lift-off Model*, and error of model predictions over the entire range of (b) mass velocity and (c) inlet subcooling.

Table 5
Submodel outputs of the *Interfacial Lift-off Model*.

Heating configuration	Inlet subcooling	ISS case number [40,41]	G [kg/m^{2}s]	p_{in} [kPa]	T_{in} [°C]	$\Delta T_{sub,in}$ [°C]	$x_{e,in}$	$q''_{CHF,exp}$ [W/cm^2]	$q''_{CHF,pred}$ [W/cm^2]	z_o [mm]	λ_c [mm]	δ [mm]	$x_{e,out}$	ε
Single	Low	234	200.0	148.2	61.4	7.4	−0.10	11.2	14.4	0.24	11.46	1.70	0.10	1.00
		242	800.0	150.9	59.9	9.5	−0.13	23.8	18.8	0.70	4.93	0.52	−0.06	0.96
		251	2400.0	151.8	59.6	10.0	−0.14	36.8	25.5	1.40	2.69	0.23	−0.11	0.89
		2129	3200.0	124.8	51.0	12.4	−0.17	38.8	31.1	1.18	2.17	0.19	−0.14	0.82
	High	2136	202.2	131.6	36.2	28.9	−0.38	24.9	14.4	0.26	12.72	1.59	−0.18	0.92
		3138	801.8	130.6	36.4	28.4	−0.38	42.3	27.5	0.52	4.80	0.53	−0.28	0.80
		2140	2399.9	125.1	36.7	26.8	−0.35	47.9	43.1	0.94	2.49	0.23	−0.30	0.65
Double	Low	207	200.0	161.3	61.4	10.1	−0.14	18.8	18.9	0.13	7.36	1.10	0.40	1.00
		2217	2400.0	164.5	63.7	8.5	−0.12	31.4	24.6	0.34	3.28	0.38	0.06	1.00
		2224	2400.0	153.0	60.3	9.6	−0.13	40.3	28.0	0.77	1.89	0.16	−0.07	0.94
		27	3200.0	127.6	51.7	12.4	−0.17	42.3	34.4	0.66	1.51	0.13	−0.11	0.86
	High	204	199.9	155.5	45.3	25.1	−0.34	20.8	22.5	0.11	7.31	1.11	0.30	1.00
		3037	803.3	131.7	36.5	28.6	−0.38	37.0	27.1	0.30	3.45	0.36	−0.19	0.86
		2040	2400.0	128.3	36.9	27.4	−0.36	45.8	45.3	0.54	1.75	0.16	−0.26	0.71

6. Conclusions

This study investigated flow boiling critical heat flux (CHF) of nPFH in a rectangular channel with single- and double-sided heating for subcooled inlet conditions in microgravity. Experiments were conducted as the first phase of the Flow Boiling and Condensation Experiment (FBCE) with the Flow Boiling Module (FBM) installed, for over a period of ~6 months onboard the International Space Station (ISS). The database covered a wide range of mass velocities and inlet subcoolings at two pressure ranges for both single- and double-sided heating of rectangular channel. Key conclusions of this study are:

(1) High-speed-video flow visualization of the FBM's heated section surrounding CHF was used to explain experimental trends and describe the physical mechanism of CHF observed in microgravity. Additionally, operating conditions, that resulted flow reversal and disrupted typical flow behavior leading up to CHF, were identified. These were most prominent at low mass velocities and large degrees of inlet subcooling.
(2) The parametric effects of various operating conditions were investigated for both single- and double-sided heating. For both heating configurations, q''_{CHF} was strongly dependent on and increased monotonically with mass velocity. Trends with respect to inlet subcooling were more complex. Increases in inlet subcooling at high inlet subcooling resulted in larger q''_{CHF}, while variation in inlet subcooling showed a negligible effect on q''_{CHF} near saturation. Depending on the inlet subcooling, either single- or double-sided heating yielded greater q''_{CHF} at low mass velocity. However, increasing G converged q''_{CHF} for the two heating configurations.
(3) Generally q''_{CHF} decreases with increasing $x_{e,out}$ until a certain point, depending on mass velocity, where q''_{CHF} becomes insensitive to $x_{e,out}$. Non-dimensionalizing heat flux reinforces conventional trends observed with respect to mass velocity and subcooling.
(4) The new microgravity CHF data was compared against CHF data for vertical upflow in Earth gravity. For single-sided heating, CHF in μg_e was consistently lower than in $1g_e$ for all mass velocities, and severely degraded at low mass velocity, with diminishing differences at as mass velocity is increased. For double-sided heating, less significant differences in CHF were observed between the two gravitational environments throughout the entire mass velocity range.
(5) Conventional prediction methods of flow boiling q''_{CHF} were assessed for the ISS database. A brief correlation assessment was performed with available correlations that have already proven capable for flow boiling in microgravity. The best performing correlation was one by the present authors [50] with an overall MAE of 18.46%.
(6) Flow patterns observed during flow visualization resembled those described in the Interfacial Lift-off model. The model performed reasonably well with an overall MAE of 23.02%, outperforming most correlations.

Declaration of Competing Interest

The authors declare the following financial interests/personal relationships which may be considered as potential competing interests:

Issam Mudawar reports financial support was provided by NASA.

CRediT authorship contribution statement

Issam Mudawar: Conceptualization, Methodology, Supervision, Writing – review & editing, Funding acquisition. **Steven J. Darges:** Validation, Software, Formal analysis, Investigation, Writing – original draft. **V.S. Devahdhanush:** Methodology, Formal analysis, Investigation, Data curation, Writing – original draft, Writing – review & editing.

Data availability

The experimental raw data used in this paper will be publicly made available in a NASA repository later.

Acknowledgement

The authors acknowledge the support of the National Aeronautics and Space Administration (NASA) under grant no. 80NSSC22K0328. The authors thank their collaborators at NASA Glenn Research Center, especially Mohammad M. Hasan, Henry K. Nahra, R. Balasubramaniam, and Jeffrey R. Mackey. The authors also thank the FBCE team at NASA Glenn Research Center, Cleveland, Ohio, especially Nancy Hall (FBCE Project Manager), Rochelle May and Phillip Gonia (Software Engineering), Mark Sorrells (Assembly, Integration and Test Lead), Jesse DeFiebre (Fluids Lead), Monica Guzik (FBCE Chief Engineer), and ZIN FCF Mission Operations Team, for their dedicated technical assistance and successful completion of ISS testing of FBCE's FBM.

References

[1] F.P. Chiaramonte, J. McQuillen, H.K. Nahra, P. Manoharan, H. Vanhala, B.J. Motil, J. Kim, V. Carey, W.G. Anderson, J. Plawsky, L. Carter, A. Jackson, 2019 NASA division of space and life and phyiscal sciences research and applications fluid physics workshop report, Cleveland, OH, USA, 2020.
[2] The National Academies, Recapturing a Future For Space Exploration, National Academies Press, Washington, D.C., USA, 2011, doi:10.17226/13048.
[3] C. Konishi, I. Mudawar, M.M. Hasan, Criteria for negating the influence of gravity on flow boiling critical heat flux with two-phase inlet conditions, Int. J. Heat Mass Transfer 65 (2013) 203–218, doi:10.1016/j.ijheatmasstransfer.2013.05.070.
[4] L.E. O'Neill, I. Park, C.R. Kharangate, V.S. Devahdhanush, V. Ganesan, I. Mudawar, Assessment of body force effects in flow condensation, part II: criteria for negating influence of gravity, Int. J. Heat Mass Transfer 106 (2017) 313–328, doi:10.1016/j.ijheatmasstransfer.2016.07.019.
[5] T. Oka, Y. Aba, K. Tanaka, Y.H. Mori, A. Nagashima, Observational study of pool boiling under microgravity, JSME Int. J. Ser. 2 35 (2) (1992) 280–286, doi:10.1299/jsmeb1988.35.2_280.
[6] M. Saito, N. Yamaoka, K. Miyazaki, M. Kinoshita, Y. Abe, Boiling two-phase flow under microgravity, Nucl. Eng. Des. 146 (1–3) (1994) 451–461, doi:10.1016/0029-5493(94)90350-6.
[7] H. Ohta, Experiments on microgravity boiling heat transfer by using transparent heaters, Nucl. Eng. Des. 175 (1–2) (1997) 167–180, doi:10.1016/S0029-5493(97)00172-6.
[8] H. Ohta, K. Kawasaki, S. Okada, H. Azuma, S. Yoda, T. Nakamura, On the heat transfer mechanisms in microgravity nucleate boiling, Adv. Space Res. 24 (10) (1999) 1325–1330, doi:10.1016/S0273-1177(99)00741-3.
[9] Y. Ma, J.N. Chung, An experimental study of critical heat flux (CHF) in microgravity forced-convection boiling, Int. J. Multiphase Flow 27 (10) (2001) 1753–1767, doi:10.1016/S0301-9322(01)00031-3.
[10] H. Zhang, I. Mudawar, M.M. Hasan, Flow boiling CHF in microgravity, Int. J. Heat Mass Transfer 48 (15) (2005) 3107–3118, doi:10.1016/j.ijheatmasstransfer.2005.02.015.
[11] C. Konishi, H. Lee, I. Mudawar, M.M. Hasan, H.K. Nahra, N.R. Hall, J.D. Wagner, R.L. May, J.R. Mackey, Flow boiling in microgravity: part 1 – Interfacial behavior and experimental heat transfer results, Int. J. Heat Mass Transfer 81 (2015) 705–720, doi:10.1016/j.ijheatmasstransfer.2014.10.049.
[12] C. Konishi, H. Lee, I. Mudawar, M.M. Hasan, H.K. Nahra, N.R. Hall, J.D. Wagner, R.L. May, J.R. Mackey, Flow boiling in microgravity: part 2 - Critical heat flux interfacial behavior, experimental data, and model, Int. J. Heat Mass Transfer 81 (2015) 721–736, doi:10.1016/j.ijheatmasstransfer.2014.10.052.
[13] Y.F. Xue, J.F. Zhao, J.J. Wei, J. Li, D. Guo, S.X. Wan, Experimental study of nucleate pool boiling of FC-72 on smooth surface under microgravity, Microgravity Sci. Tec. 23 (S1) (2011) 75–85, doi:10.1007/s12217-011-9274-5.
[14] X. Wang, Y. Zhang, B. Qi, J. Zhao, J. Wei, Experimental study of the heater size effect on subcooled pool boiling heat transfer of FC-72 in microgravity, Exp. Therm. Fluid Sci. 76 (2016) 275–286, doi:10.1016/j.expthermflusci.2016.03.031.

[15] R. Raj, J. Kim, Heater size and gravity based pool boiling regime map: transition criteria between buoyancy and surface tension dominated boiling, J. Heat Transfer 132 (9) (2010), doi:10.1115/1.4001635.
[16] D. Brutin, V.S. Ajaev, L. Tadrist, Pressure drop and void fraction during flow boiling in rectangular minichannels in weightlessness, Appl. Therm. Eng. 51 (1–2) (2013) 1317–1327, doi:10.1016/j.applthermaleng.2012.11.017.
[17] R.R. Souza, J.C. Passos, E.M. Cardoso, Confined and unconfined nucleate boiling under terrestrial and microgravity conditions, Appl. Therm. Eng. 51 (1–2) (2013) 1290–1296, doi:10.1016/j.applthermaleng.2012.09.035.
[18] M. Narcy, E. de Malmazet, C. Colin, Flow boiling in tube under normal gravity and microgravity conditions, Int. J. Multiphase Flow 60 (2014) 50–63, doi:10.1016/j.ijmultiphaseflow.2013.11.011.
[19] Y. Zhang, B. Liu, J. Zhao, Y. Deng, J. Wei, Experimental study of subcooled flow boiling heat transfer on a smooth surface in short-term microgravity, Microgravity Sci. Tec. 30 (6) (2018) 793–805, doi:10.1007/s12217-018-9629-2.
[20] Y. Yang, X. Chen, Y. Huang, G. Li, Experimental study on pool boiling of distilled water and HFE7500 fluid under microgravity, Acta Astronaut 143 (2018) 362–371, doi:10.1016/j.actaastro.2017.11.011.
[21] M.T. Lebon, C.F. Hammer, J. Kim, Gravity effects on subcooled flow boiling heat transfer, Int. J. Heat Mass Transfer 128 (2019) 700–714, doi:10.1016/j.ijheatmasstransfer.2018.09.011.
[22] D.M. Iceri, G. Zummo, L. Saraceno, G. Ribatski, Convective boiling heat transfer under microgravity and hypergravity conditions, Int. J. Heat Mass Transfer 153 (2020) 119614, doi:10.1016/j.ijheatmasstransfer.2020.119614.
[23] B. Liu, B. Yuan, P. Xu, J. Zhao, Y. Zhang, J. Wei, Y. Yang, Q. Cao, A method for approximating the CHF of subcooled flow boiling in microgravity by ground tests, Int. J. Multiphase Flow 122 (2020) 103161, doi:10.1016/j.ijmultiphaseflow.2019.103161.
[24] C. Konishi, I. Mudawar, Review of flow boiling and critical heat flux in microgravity, Int. J. Heat Mass Transfer 80 (2015) 469–493, doi:10.1016/j.ijheatmasstransfer.2014.09.017.
[25] P. Di Marco, W. Grassi, Pool boiling in microgravity: assessed results and open issues, in: Proc. 3rd European Therm. Conf., Heidelberg, Germany, 2000, pp. 81–90.
[26] R. Raj, J. Kim, J. McQuillen, Pool boiling heat transfer on the International Space Station: experimental results and model verification, J. Heat Transfer 134 (10) (2012), doi:10.1115/1.4006846.
[27] N.J. Penley, C.P. Schafer, J.-D.F. Bartoe, The international space station as a microgravity research platform, Acta Astronaut 50 (11) (2002) 691–696, doi:10.1016/S0094-5765(02)00003-6.
[28] H.S. Lee, H. Merte, F. Chiaramonte, Pool boiling curve in microgravity, J. Thermophys. Heat Transfer 11 (2) (1997) 216–222, doi:10.2514/2.6225.
[29] J.F. Zhao, G. Liu, S.X. Wan, N. Yan, Bubble dynamics in nucleate pool boiling on thin wires in microgravity, Microgravity Sci. Tec. 20 (2) (2008) 81–89, doi:10.1007/s12217-008-9010-y.
[30] J.F. Zhao, J. Li, N. Yan, S.-.F. Wang, Bubble behavior and heat transfer in quasi-steady pool boiling in microgravity, Microgravity Sci. Tec. 21 (S1) (2009) 175–183, doi:10.1007/s12217-009-9151-7.
[31] V.K. Dhir, G.R. Warrier, E. Aktinol, D. Chao, J. Eggers, W. Sheredy, W. Booth, Nucleate pool boiling experiments (NPBX) on the International Space Station, Microgravity Sci. Tec. 24 (5) (2012) 307–325, doi:10.1007/s12217-012-9315-8.
[32] H. Ohta, H. Asano, O. Kawanami, K. Suzuki, R. Imai, Y. Shinmoto, S. Matsumoto, T. Kurimoto, H. Takaoka, K. Fujii, M. Sakamoto, K. Sawada, H. Kawasaki, A. Okamoto, K. Kogure, T. Oka, K. Usuku, T. Tomobe, M. Takayanagi, Development of boiling and two-phase flow experiments on board ISS (research objectives and concept of experimental setup), Int. J. Microgravity Sci. Appl. 33 (2016) 330102, doi:10.15011/ijmsa.33.330102.
[33] K. Inoue, H. Ohta, Y. Toyoshima, H. Asano, O. Kawanami, R. Imai, K. Suzuki, Y. Shinmoto, S. Matsumoto, Heat loss analysis of flow boiling experiments onboard international space station with unclear thermal environmental conditions (1st report: subcooled liquid flow conditions at test section inlet), Microgravity Sci. Tec. 33 (2) (2021) 28, doi:10.1007/s12217-021-09869-5.
[34] K. Inoue, H. Ohta, H. Asano, O. Kawanami, R. Imai, K. Suzuki, Y. Shinmoto, T. Kurimoto, S. Matsumoto, Heat loss analysis of flow boiling experiments onboard international space station with unclear thermal environmental conditions (2nd report: liquid-vapor two-phase flow conditions at test section inlet), Microgravity Sci. Tec. 33 (5) (2021) 57, doi:10.1007/s12217-021-09902-7.
[35] Y. Katto, H. Ohno, An improved version of the generalized correlation of critical heat flux for the forced convective boiling in uniformly heated vertical tubes, Int. J. Heat Mass Transfer 27 (9) (1984) 1641–1648, doi:10.1016/0017-9310(84)90276-X.
[36] M.M. Shah, Improved general correlation for critical heat flux during upflow in uniformly heated vertical tubes, Int. J. Fluid Fl. 8 (4) (1987) 326–335, doi:10.1016/0142-727X(87)90069-5.
[37] S.S. Kutateladze, A.I. Leont'ev, Some applications of the asymptotic theory of the turbulent boundary layer, in: Proc. Int. Heat Transfer Conf. 3, Begellhouse, Chicago, IL, USA, 1966, pp. 1–6, doi:10.1615/IHTC3.1920.
[38] J. Weisman, B.S. Pei, Prediction of critical heat flux in flow boiling at low qualities, Int. J. Heat Mass Transfer 26 (10) (1983) 1463–1477, doi:10.1016/S0017-9310(83)80047-7.
[39] C.H. Lee, I. Mudawwar, A mechanistic critical heat flux model for subcooled flow boiling based on local bulk flow conditions, Int. J. Multiphase Flow 14 (6) (1988) 711–728, doi:10.1016/0301-9322(88)90070-5.
[40] I. Mudawar, V.S. Devahdhanush, S.J. Darges, M.M. Hasan, H.K. Nahra, R. Balasubramaniam, J.R. Mackey, Heat transfer and interfacial flow physics of microgravity flow boiling in single-side-heated rectangular channel with subcooled inlet conditions – Experiments onboard the International Space Station, Int. J. Heat Mass Transfer 207 (2023) 123998, doi:10.1016/j.ijheatmasstransfer.2023.123998.
[41] I. Mudawar, V.S. Devahdhanush, S.J. Darges, M.M. Hasan, H.K. Nahra, R. Balasubramaniam, J.R. Mackey, Effects of heating configuration and operating parameters on heat transfer and interfacial physics of microgravity flow boiling with subcooled inlet conditions – Experiments onboard the International Space Station, Int. J. Heat Mass Transfer (2023) under review.
[42] A. Habibi Khalaj, S.K. Halgamuge, A review on efficient thermal management of air- and liquid-cooled data centers: from chip to the cooling system, Appl. Energy 205 (2017) 1165–1188, doi:10.1016/j.apenergy.2017.08.037.
[43] W.A. Arnold, T.G. Hartman, J. McQuillen, Chemical characterization and thermal stressing studies of perfluorohexane fluids for space-based applications, J. Spacecraft Rockets 44 (1) (2007) 94–102, doi:10.2514/1.22537.
[44] J. Lee, V.S. Devahdhanush, S.J. Darges, I. Mudawar, Effects of flow loop compressible volume position on system instabilities during flow boiling in microchannel heat sinks, Int. J. Heat Mass Transfer 198 (2022) 123394, doi:10.1016/j.ijheatmasstransfer.2022.123394.
[45] J. Lee, I. Mudawar, M.M. Hasan, H.K. Nahra, J.R. Mackey, Experimental and computational investigation of flow boiling in microgravity, Int. J. Heat Mass Transfer 183 (2022) 122237, doi:10.1016/j.ijheatmasstransfer.2021.122237.
[46] E.W. Lemmon, I.H. Bell, M.L. Huber, M.O. McLinden, NIST standard reference database 23: reference fluid thermodynamic and transport properties-REFPROP, Version 10, NIST, Gaithersburg, MD, USA, 2018.
[47] V.S. Devahdhanush, I. Mudawar, H.K. Nahra, R. Balasubramaniam, M.M. Hasan, J.R. Mackey, Experimental heat transfer results and flow visualization of vertical upflow boiling in Earth gravity with subcooled inlet conditions – In preparation for experiments onboard the International Space Station, Int. J. Heat Mass Transfer 188 (2022) 122603, doi:10.1016/j.ijheatmasstransfer.2022.122603.
[48] C. Konishi, I. Mudawar, M.M. Hasan, Investigation of localized dryout versus CHF in saturated flow boiling, Int. J. Heat Mass Transfer 67 (2013) 131–146, doi:10.1016/j.ijheatmasstransfer.2013.07.082.
[49] S.J. Darges, V.S. Devahdhanush, I. Mudawar, H.K. Nahra, R. Balasubramaniam, M.M. Hasan, J.R. Mackey, Experimental results and interfacial lift-off model predictions of critical heat flux for flow boiling with subcooled inlet conditions – In preparation for experiments onboard the International Space Station, Int. J. Heat Mass Transfer 183 (2022) 122241, doi:10.1016/j.ijheatmasstransfer.2021.122241.
[50] S.J. Darges, V.S. Devahdhanush, I. Mudawar, Assessment and development of flow boiling critical heat flux correlations for partially heated rectangular channels in different gravitational environments, Int. J. Heat Mass Transfer 196 (2022) 123291, doi:10.1016/j.ijheatmasstransfer.2022.123291.
[51] C.P. Tso, K.W. Tou, G.P. Xu, Flow boiling critical heat flux of FC-72 from flush-mounted and protruded simulated chips in a vertical rectangular channel, Int. J. Multiphase Flow 26 (3) (2000) 351–365, doi:10.1016/S0301-9322(99)00023-3.
[52] G.P. Celata, M. Cumo, A. Mariani, Assessment of correlations and models for the prediction of CHF in water subcooled flow boiling, Int. J. Heat Mass Transfer 37 (2) (1994) 237–255, doi:10.1016/0017-9310(94)90096-5.
[53] P.K. Sarma, V. Srinivas, K.V. Sharma, V.D. Rao, G.P. Celata, A correlation to evaluate critical heat flux in small diameter tubes under subcooled conditions of the coolant, Int. J. Heat Mass Transfer 49 (1–2) (2006) 42–51, doi:10.1016/j.ijheatmasstransfer.2004.07.052.
[54] C.B. Tibiriçá, G. Ribatski, J.R. Thome, Saturated flow boiling heat transfer and critical heat flux in small horizontal flattened tubes, Int. J. Heat Mass Transfer 55 (25–26) (2012) 7873–7883, doi:10.1016/j.ijheatmasstransfer.2012.08.017.
[55] W. Zhang, T. Hibiki, K. Mishima, Y. Mi, Correlation of critical heat flux for flow boiling of water in mini-channels, Int. J. Heat Mass Transfer 49 (5–6) (2006) 1058–1072, doi:10.1016/j.ijheatmasstransfer.2005.09.004.
[56] J.E. Galloway, I. Mudawar, CHF mechanism in flow boiling from a short heated wall—II. Theoretical CHF model, Int. J. Heat Mass Transfer 36 (10) (1993) 2527–2540, doi:10.1016/S0017-9310(05)80191-7.
[57] H. Zhang, I. Mudawar, M.M. Hasan, CHF model for subcooled flow boiling in Earth gravity and microgravity, Int. J. Heat Mass Transfer 50 (19–20) (2007) 4039–4051, doi:10.1016/j.ijheatmasstransfer.2007.01.029.
[58] J.C. Sturgis, I. Mudawar, Critical heat flux in a long, rectangular channel subjected to one-sided heating—II. Analysis of critical heat flux data, Int. J. Heat Mass Transfer 42 (10) (1999) 1849–1862, doi:10.1016/S0017-9310(98)00275-0.
[59] H. Lamb, Hydrodynamics, 6th ed., Dover Publications, New York, NY, USA, 1945.
[60] L.M. Milne-Thompson, Theoretical Hydrodynamics, 4th ed., Collier-Macmillan, New York, NY, USA, 1960.
[61] H. Zhang, I. Mudawar, M.M. Hasan, Experimental and theoretical study of orientation effects on flow boiling CHF, Int. J. Heat Mass Transfer 45 (22) (2002) 4463–4477, doi:10.1016/S0017-9310(02)00152-7.
[62] M.S. Bhatti, R.K. Shah, Turbulent and transition flow convective heat transfer in ducts, Handbook of Single-Phase Convective Heat Transfer, Wiley, New York, NY, USA, 1987.